

Mathematical and computational modeling of metallic biomaterials biodegradation

Mojtaba Barzegari

June 2023

Contents

1 General introduction	3
1.1 Biodegradable metals	3
1.2 Magnesium as a biodegradable material	5
1.3 Chemistry of biodegradation of magnesium	7
1.4 Computational modeling of biodegradation	11
2 Aims and objectives	14
2.1 General aim	14
2.2 Specific objectives	15
2.3 Thesis outline	17
3 Developing the core computational model	19
3.1 Introduction	19
3.1.1 Magnesium biodegradation	19
3.1.2 Computational modeling of Mg degradation	20
3.2 Background theory	22
3.2.1 Biodegradation as a reaction-diffusion system	22
3.2.2 Moving boundary - Stefan problems	23
3.2.3 Level-set method	23
3.3 Materials and methods	24
3.3.1 Underlying chemistry	24
3.3.2 Mathematical modeling	25
3.3.3 Interface movement formulation	27
3.3.4 Boundary conditions	27
3.3.5 Implementation	28
3.3.6 Experimental setup	30
3.3.7 Parameter estimation	30
3.3.8 Simulation setup	32
3.3.9 Case study	34
3.4 Results	34
3.4.1 Optimization results	34

3.4.2	Degradation prediction	35
3.4.3	Example application	36
3.5	Discussion	37
3.6	Conclusions	42
4	Extending the model: adding fluid flow and convection	43
4.1	Introduction	43
4.2	Methods	45
4.2.1	Navier-Stokes equations	45
4.2.2	Weak formulation of the Navier-Stokes equations	46
4.2.3	Stokes equations	47
4.2.4	Implementation	48
4.2.5	Preconditioning and parallelizing the computation	50
4.2.6	Considering the degrading object	51
4.2.7	Simulation setup	52
4.3	Results	54
4.4	Discussion	56
4.5	Conclusion	59
5	Extending the model: simulating local pH evolution	63
5.1	Introduction	63
5.2	Methods	66
5.2.1	Experimental setup	66
5.2.2	Computational model construction	67
5.2.3	Simulation setup	72
5.3	Results	73
5.3.1	Thermodynamics-based simulation	73
5.3.2	Biodegradation simulations	73
5.4	Discussion	74
5.5	Conclusion	77

Chapter 1

General introduction

Biodegradable (bioabsorbable) implants provide temporary support for tissues, where the implants completely dissolve and are absorbed by the body during or after tissue healing, avoiding several drawbacks of permanent implants [1]. The application of biodegradable metallic biomaterials [2–4], including magnesium [5–7], zinc [8, 9], and iron [10], has become more prominent for over a decade in various biomedical engineering and tissue engineering disciplines. Among the mentioned materials, magnesium (Mg) is the most studied metal [11], the reason for which is its suitable mechanical and chemical properties for biomedical applications. Although poor corrosion resistance of Mg is a limiting factor for its application as light structural material, like in the transportation industry, it becomes an interesting characteristic when it comes to the biodegradable materials field for cardiovascular and orthopedic applications [12–14]. The first clinical usage of Mg was reported in 1878, but a renewed interest in it has grown significantly in the last 15–20 years [11]. From the clinical and biomedical perspective, two major concerns about using Mg in clinics are the release of hydrogen gas and surface alkalization due to Mg dissolution [15]. These issues are commonly addressed by alloying, biocompatible coating and surface modification [11]. This chapter includes an overview of biodegradable materials with a focus on Mg, the history of their usage in medical applications, a description of the chemistry of Mg biodegradation, and various computational models aiming to capture this chemistry.

1.1 Biodegradable metals

It has been a very long time since metals have started being employed as implant materials to support, reinforce, repair, or replace damaged tissues

and organs. Historically speaking, iron dental implants were discovered in the remains of a European who perished at the end of the first century AD or the start of the second century [16]. Moreover, gold has been used for the same application in China since ancient times. With more development in materials science and engineering, inert materials such as titanium alloys, cobalt alloys, and stainless steel are widely used nowadays in biomedical implants and devices. However, there are certain drawbacks to these materials in medical applications:

- The release of metallic ions from implants fabricated with these materials can lead to various side effects in the surrounding tissues such as inflammation.
- In some cases, such as for temporary fixation in cardiovascular and orthopedics applications, implant presence is unnecessary after the healing process. Moreover, removing the implant via a secondary surgery may not be a practical solution, causing suffering and pain to the patient again.
- The difference between the elastic modulus of these materials and the surrounding tissues can lead to various mechanical integrity issues. For instance, in the case of bone, this difference causes stress shielding effect, where the implant acts as a shield preventing the bone from receiving enough mechanical load needed for bone remodeling and growth. Additionally, this may cause further mechanical loosening of the implant and secondary bone fracture.

Biodegradable implants would be a great solution to the issues mentioned above. Implants fabricated from biodegradable materials gradually disappear and get absorbed by the body. With more attention to employing these materials in clinical applications, more research studies were conducted to investigate their various aspects. Initially, degradable polymers (such as polylactic acid) were used for this purpose, but later studies showed that they might stimulate the aseptic inflammation of surrounding tissues [1]. Besides, the mechanical properties of polymer materials are not acceptable in load-bearing applications. As a result, biodegradable metals gained more attention in orthopedics where Mg is the most suitable candidate due to its elastic modulus (41-45 GPa) being closest to that of natural bone (2-30 GPa) [17]. In addition to this, especially for bone healing applications, the released metallic ions during the degradation process contribute to the metabolism of the underlying biological process. For example, Mg is one of the most abundant ions found in the bone, and Mg cations have a beneficial impact on

the metabolism of enzymes in the bone regeneration process. Similarly, iron (Fe) plays a key role in oxygen transport in the body, and zinc (Zn) positively influences the physiological functions of bone healing and the formation of different transcriptional factors [18–22].

1.2 Magnesium as a biodegradable material

From the corrosion science perspective, Mg is an active material with a relatively low standard electrode potential of -2.37V , meaning that Mg and its alloys have high corrosion/degradation rate [1]. This property makes Mg and Mg-based alloys a biodegradable metal in biomedical applications, where the materials undergo corrosion in biological and physiological conditions and disappear during or after the damaged tissue is repaired.

From the biological perspective, Mg can contribute positively to the human body's metabolism to improve health. A normal adult body contains 20 – 28g of Mg, from which 27% is distributed in muscles, 65% in bone, and the rest in blood and other tissues [23]. Additionally, Mg contributes to more than 300 enzyme reactions in the body [24]. Extra Mg not needed by the body metabolism is transported via the circulatory system and excreted through the bladder, without causing any major side effect [17].

The first application of Mg for biomedical purposes was recorded in 1878 by Hues, who made artificial radial arteries from Mg and suggested that Mg can be beneficial for the treatment of ovariectomy and hemorrhoids [1]. Payr performed successful animal experiments using Mg tubular vascular connectors in 1900, after which the vessels were reformed, and vascular thickness returned to its normal range after 16 days of implantation [25]. This started a wide range of usage of Mg for cardiovascular applications, a recent example of which is the work by Ikeo et al. for designing V-shaped vascular clips made of Mg-Zn-Ca alloy [26]. In this work, the ductility of Mg was reported to be an added advantage for bearing large plastic deformations that these clips experience. In a relevant study, Erbel et al. implanted 71 stents made of Mg alloys in the coronary arteries of 63 patients. The results showed a similar efficiency and safety for Mg stents to that of other metallic stents [27]. Moreover, Mg stents degraded without any problem after four months. This type of study resulted in acquiring the CE mark for the next generation of Mg stents in Europe [28, 29].

The history of usage of Mg in orthopedics applications started very similarly to its vascular applications. In the study by Payr mentioned above, he also stated that Mg can improve the bone healing rate [25]. Six years later, in 1906, the first Mg-based implant was used by Lambotte for fixation

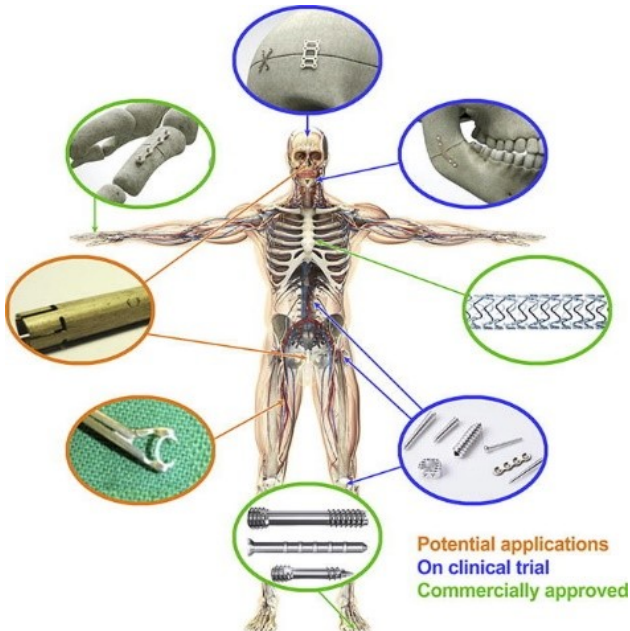


Figure 1.1: Various potential applications of Mg as a biodegradable metallic biomaterial for cardiovascular and orthopedic implants and devices [4].

of a fracture case [30, 31]. This study was followed by many other studies in the last century, the results of which confirmed that Mg could facilitate the bone healing process. However, these studies also demonstrated that the hydrogen gas released during the biodegradation of Mg could lead to inflammation. Furthermore, since Mg's rate of degradation is high, the tissues may not receive enough support before the implants vanish [25]. These issues made the Mg-based implants less common compared to inert metals for orthopedics applications. But, in recent decades, these implants gained more attention thanks to enormous research studies on the biodegradation of Mg to control its side effects and degradation behavior. In 2005, the possibility of using Mg for orthopedics implants was proposed by Witte et al. [32], a suggestion supported by the results of animal studies on femoral implants manufactured from Mg alloys (AZ31, AZ91, WE43, and LAE442). After this study, a wide variety of research works were conducted to investigate the efficiency of Mg-based implants for orthopedics applications [5, 33, 34]. Fig. 1.1 shows the current usage of Mg-based implants and medical devices divided into three categories: commercially approved, on clinical trials, and potential applications [4].

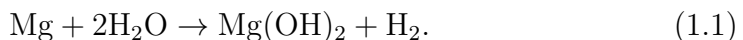
1.3 Chemistry of biodegradation of magnesium

The biodegradation behavior of Mg is investigated in corrosion tests, in which the selection of the corrosive media plays an important role since it affects the underlying chemical reactions [35]. By considering the main application of the biomaterial, which can be tissue engineering scaffolds, vascular stents, or orthopedic fixation devices, the corrosive media can be selected to be a representative of the service environment. The most basic form of the medium is a saline (NaCl) solution, in which the degradation rate is the highest possible [35]. More complex solutions can be used to mimic the behavior of the body environment by taking into account more body fluid components, the most popular of which are Ringer's solution, PBS (phosphate buffered saline), SBFs (simulated body fluids), HBSS (Hank's balanced salt solution), and Earle's balanced salt solution (EBSS) [35]. Adding more organic components to the solution will prepare it to simulate cell culture conditions. The common media for this purpose are MEM (Minimum Essential medium) and DMEM (Dulbecco's modified Eagle's medium) [35]. Fig. 1.2 summarizes various commonly used corrosive media for testing biodegradable metals along with their main components [35].

Various studies have already investigated the effect of different components in the aforementioned corrosive media on the degradation behavior of Mg materials [36–40]. In addition to the presented chemical components, it has been shown that synthetic pH buffers (such as Tris and HEPES) contribute to the biodegradation rate of Mg [36]. The investigations on the effect of different inorganic components, including carbonate, phosphate, sulfate and calcium, show these components' effective contribution to the degradation rate. However, the corrosion protection resulting from the mutual effect of carbonate, phosphate and calcium has been emphasized more [36, 39].

The most common solution for performing corrosion tests on Mg is saline (NaCl) solution, in which the material undergoes aggressive corrosion due to higher electrochemical activities [41, 42]. In a typical aqueous solution, the major corrosion reactions occurring can be written as detailed below [43, 44].

Main, hydrogen evolution reaction (HER):



Secondary, oxygen reduction reaction (ORR):



In this situation, the corrosion products forming on the corroded surface of Mg consist mainly of Mg(OH)_2 and MgO , and the pH in regions close to

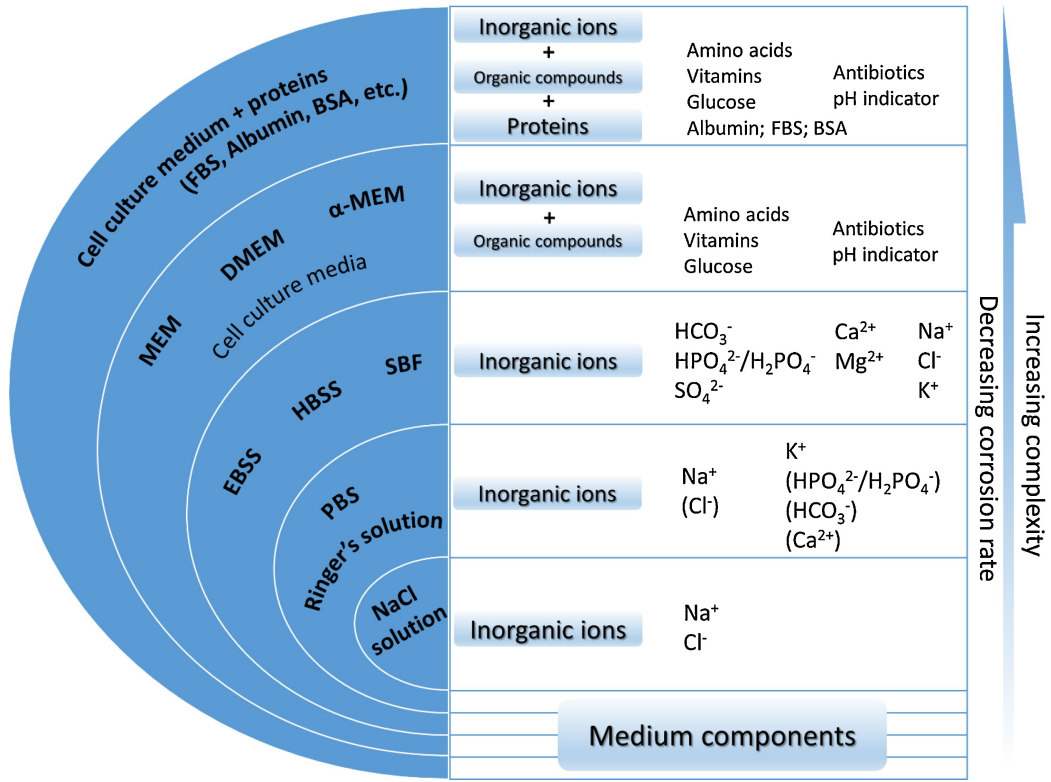
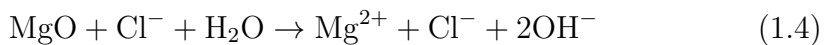
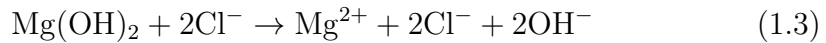


Figure 1.2: A schematic representation of commonly used corrosive media for testing biodegradable metals, sorted by their complexity from the chemical perspective from bottom to top [35].

this surface remains alkaline. In the presence of chloride ions in the saline medium, the formed corrosion product may be broken or bypassed, leading to an increased degradation rate.



The main advantage of using a saline solution for corrosion tests compared to more complex media is that the absence of inorganic ions like carbonate, phosphate, sulfate and calcium allows for investigating the corrosion behavior without concerning possible effect caused by the interaction of these chemical components. On the other hand, the main weakness of saline solution is that it cannot represent the complexity of real body fluid, and as a result, a more complex medium is required to investigate such conditions. To address this issue, more complex saline solutions, such as PBS, are widely used

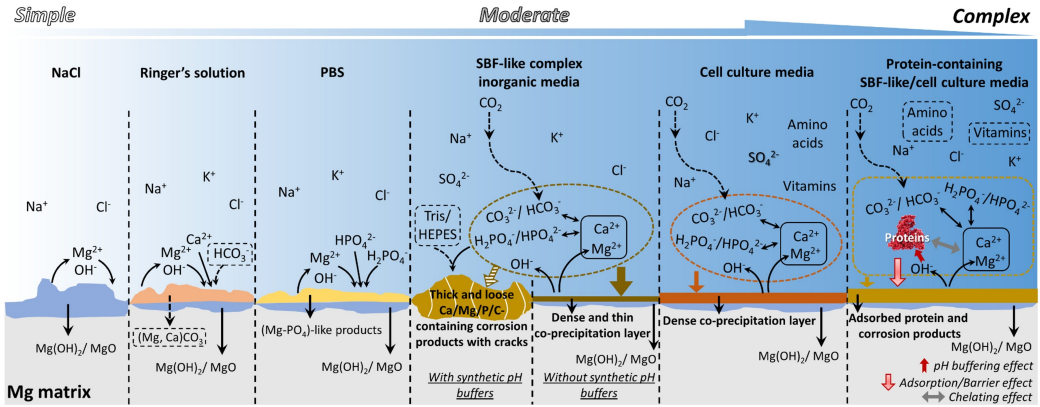


Figure 1.3: A schematic representation of Mg biodegradation behavior in commonly used solutions for corrosion tests of biodegradable metals [35].

for assessing the applicability of Mg alloys in more complex conditions from the chemical perspective [45, 46]. Despite the mentioned limitations, corrosion tests in saline solution are still contributing to understanding intrinsic degradation properties of Mg.

The term "simulated body fluid" is generally used to refer to solutions containing inorganic ions of human serum and interstitial fluid [35]. The commonly used corrosive media in this regard are SBF, HBSS, and EBSS, which all include the same inorganic components yet with a slight difference in their concentrations. A typical composition of these media is chloride, carbonate, phosphates, sulfate and calcium. The individual effect of these components on the rate of degradation of Mg has been extensively studied, where it has been observed that carbonate and phosphate slow down the rate whereas the effect of sulfate is negligible [38, 40]. The concentration of HCO_3^- affects the pH buffering capacity and the degradation rate of Mg simultaneously [47]. The effect of calcium ions is more complex because it does not contribute to Mg corrosion directly. Fig. 1.3 briefly summarizes the various reactions and formed precipitation compositions of the mentioned media for testing the degradation behavior of Mg [35].

There are various evaluation techniques for measuring the degradation rate of Mg, among which the weight loss, hydrogen evolution, potentiodynamic polarization, and electrochemical impedance spectroscopy are the commonly used ones. Generally speaking, the method used for evaluating the degradation rate can affect the reported behavior. For example, it has been shown that in HBSS, the measured corrosion rate of Mg is lower (slower) when evaluated using hydrogen evolution in comparison to the rate found by

direct weight loss measurements [48, 49], which can be due to the secondary dissolution of evolved hydrogen. Moreover, oxygen consumption due to secondary ORR can affect the volume of evolved gas, which is more significant for media with slower degradation rates such as HBSS and MEM [33]. Table 1.1 summarizes the advantages and shortcomings of widely used techniques for measuring degradation rate [35].

Discussing the degradation rate of Mg-based materials can be tricky because as mentioned before, the measurement method and the employed solution can influence the measured degradation rate [50]. However, certain studies have performed this quantitative measurement using different representative media for *in vivo* conditions, resulting in different reported values. The corrosion rate for pure Mg in EBSS was reported to be $0.39 \text{ mm.year}^{-1}$ [51], but in SBF and HBSS, the reported values are 1.39 [52] and $2.05 \text{ mm.year}^{-1}$ [53], respectively. Alloying Mg and adding Ca-P coating seems to decrease the degradation rate to $0.25 \text{ mm.year}^{-1}$ in HBSS [54] and $1.88 \text{ mm.year}^{-1}$ in SBF [55], although no direct correlation between alloying compounds and the degradation rate has been found yet [56].

Table 1.1: Summary of various common methods to assess the degradation rate of Mg [35]

Test method	Advantages	Shortcomings
Weight loss	High reliability Direct measurement Easily controlled test environment	Non-continuous. Does not reveal varying corrosion rate throughout the immersion Low sensitivity at the initial stages
Hydrogen evolution	Continuous Can be automated Can be performed in closed eu-dimeters	Performed in open environment in most cases Might show underestimated values of corrosion rate due to secondary ORR and solubility of H_2 in aqueous media
Potentiodynamic polarization	Fast measurement	Non-continuous Open environment measurement in most cases Very often low correlation with long-term weight loss measurements
Electrochemical impedance spectroscopy	Continuous In situ investigation of protective properties of forming corrosion products	Performed in open environments in most cases

1.4 Computational modeling of biodegradation¹

Besides experimental approaches to investigate the properties of biodegradable metallic implants and scaffolds, computational modeling of the biodegradation process and behavior can be used as an efficient tool to design the next generation of medical devices and implants [57]. In addition to traditional modeling approaches for mechanics of materials, it is possible to take advantage of well-developed principles of modeling transport phenomena and numerical simulations to investigate the biodegradation process computationally [58].

Computational models of the biodegradation process vary from a basic implementation of the process to comprehensive mathematical models that capture multiple aspects of the degradation phenomenon. In the category of simplified corrosion models, Gao et al. performed a quantitative study on the change of mechanics during the biodegradation of Mg alloys for cardiovascular applications [59]. Liu et al. developed a fluid dynamics model to characterize the effect of the induced wall shear stress (WSS) on the biodegradation mechanism of Mg stents [60]. They investigated the effect of blood flow velocity and dynamic environment on the degradation of cardiovascular stents. Boland et al. studied the mechanical performance of Mg stents for the treatment of coronary artery diseases using a computational model [61]. Gartzke et al. proposed a degradation model for the corrosion of Mg alloys coupled with mechanical analysis, allowing them to study the change of mechanical properties during the biodegradation process [62]. Another common category of studies in this regard is continuous damage (CD) simulations, in which geometrical discontinuities get translated into the reduction of materials. Despite the limitation of this technique for modeling biodegradation, such as more focus on the mechanical integrity rather than on the fundamental phenomena, it has been used for various relevant studies, such as Gastaldi et al. [63] and Shi et al. [64].

Among the relevant studies, mass transfer-related models were more successful in representing the biodegradation process mathematically. Indeed, the approach of constructing models based on the well-formulated transport phenomena equations and then solving the derived equations using appropri-

¹This section is partially based on a manuscript prepared to be submitted:
S. Mukherjee, S. Mandal, M. Barzegari, F. Perez-Boerema, B. Liang, E. Sadeghian Dekhord, L. Groeneveldt, L. Geris, “In silico design and optimization of mesoscopic and macroscopic properties of additively manufactured scaffolds: applications in skeletal tissue engineering.”

ate numerical schemes has been followed in recent years to study biodegradation. Ahmed et al. derived a set of mathematical equations to capture the chemical reactions occurring in Mg degradation [65], in which the detailed mathematical equations provided a proper insight into the effect of different chemical components on the biodegradation of Mg *in vitro*. Grogan et al. developed a model to correlate the mass flux of the metallic ions in the biodegradation interface to the velocity of the interface, used to simulate the degradation of complex geometries of Mg-based stents [66]. Similarly, Shen et al. developed a theoretical model to predict the degradation behavior of Mg alloys in orthopedic implants [67]. Their 3D model had a high agreement with *in vitro* corrosion test results.

One of the important applications of biodegradation models is to investigate the change of shape and morphology of the implants and medical devices over time. To this end, appropriate interface capturing methods should be used to track the corrosion interface during the biodegradation process. Bajger et al. developed a mathematical model to study the degradation of Mg implants by reaction-diffusion equations and level-set method (LSM), which enabled them to track the geometrical changes of the implant during degradation [68]. Similarly, Sanz-Herrera et al. developed a comprehensive computational model as a tool for Mg implant design [69]. They combined multiple diffusion-reaction equations to study the change of concentration of the chemical components that play an essential role in *in vitro* biodegradation of Mg implants. A summary of the studies mentioned above is represented in Table 1.2. The reader is encouraged to refer to [70] for a more complete list of recent published mechanistic and phenomenological models of the biodegradation process of Mg-based implants.

The approach taken by Bajger et al. was followed in the current thesis, in which an improved model was developed by considering more chemical components and phenomena, allowing us to perform a more accurate validation using *in vitro* data. Although the biodegradation models are getting more mature and more promising for simulating experimental situations, their integration into other models, such as mechanical stability analysis or neotissue growth, to construct fully-coupled models has remained a challenge. Solving this challenge will enable future models to replicate complex *in vivo* conditions more accurately *in silico*.

Table 1.2: Summary of the recently-developed computational models of the degradation process of Mg-based biomaterials and some of their key characteristics. FEM: Finite Element Method; CFD: Computational Fluid Dynamics; FVM: Finite Volume Method; MOL: Method of Lines; FSI: Fluid-Structure Interaction; ALE: Arbitrary Lagrangian-Eulerian.

Biological system	Modeled device	Material	Basis of degradation	Software used	Modeling method	Ref
Artery	Vascular stent	Mg Alloy AZ31B	Surface corrosion	ABAQUS	FEM, UMAT	[59]
Artery	Vascular stent	Mg Alloy WE43	Surface corrosion	ANSYS Fluent	CFD, FSI, FVM	[60]
Remodeling artery	Vascular stent	Mg Alloy AZ31	Uniform and pitting corrosion	ABAQUS	FEM, USDFLD	[61]
Artery	Coronary stents	Mg alloys AZ31, AZ61, AZ80, ZK60 and ZM21	Surface and stress corrosion	ABAQUS	CD, FEM	[63]
Bone	Orthopedic implants	Pure Mg	Surface corrosion by considering biphasic layers	MATLAB	Mass transfer, MOL	[65]
Artery	Vascular stent	Mg Alloy AZ31	Surface corrosion	ABAQUS	Diffusion model, ALE, FEM	[66]
Bone	Orthopedic pins	Mg alloys Mg-1Ca and Mg-3Ge	Surface corrosion	ABAQUS	Diffusion model, FEM	[67]
Hip bone	Orthopedic implant	Pure Mg	Surface corrosion	In-house, FreeFEM	Reaction-diffusion model, LSM, FEM	[68]
Bone	Orthopedic screws	Mg alloy	Surface corrosion	In-house	Reaction-diffusion model, FEM	[69]
Bone	Porous scaffolds	Mg Alloy LAE442	Surface corrosion	ABAQUS	FEM, UMAT	[62]
Artery	Vascular stent	Mg Alloy AZ31	Surface corrosion	ABAQUS	CD, FEM, UMAT	[64]

Chapter 2

Aims and objectives

This chapter is dedicated to the elaboration of the objectives of the current thesis. It starts with the general definition of the doctoral project aims. Hereafter, the specific objectives of the doctoral project are demonstrated. Then, the chapter illustrates the thesis's outline and structure.

2.1 General aim

The use of biodegradable metals has been gaining attention for various kinds of biomedical applications in recent decades, however, controlling their functionality and behavior inside the body has remained a challenge. Computational modeling of the materials' interaction with the body can help avoid part of the expensive experimental works required to characterize the degradation properties and can provide an integrated spatiotemporal view of the whole process.

One of the most challenging parts of performing such a modeling study is to capture the chemical interactions and the dynamics and kinetics of the reactions occurring on the material-environment interface. Taking advantage of mechanistic modeling principles of mass transfer coupled with free boundary and moving interface formulations seems to be a promising solution to this complex problem. By doing so, one can model the degradation process by a set of equations capturing the interaction of various chemical components while tracking the moving corrosion front, which changes the location where the dynamic is taking place.

In this study, we have developed a mathematical and computational model to predict the biodegradation behavior of biodegradable metallic biomaterials, focusing on Mg. This model enables us to investigate the chemical and, later on, biological phenomena occurring on the corrosion interface of

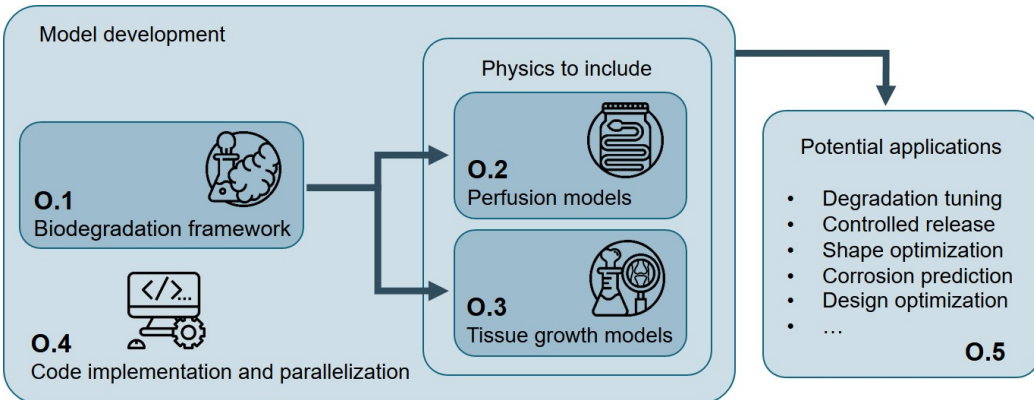


Figure 2.1: Schematic representation of the structure and outline of the current project, divided into five objectives.

these biomaterials. Additionally, coupling the model with other existing cell and tissue growth models leads to a multiphysics model combining the chemistry of biodegradation, the physics of the electrolytes and body fluids flow, and the biology of tissue growth/regeneration. Building such a model requires dealing with several challenges, one of which is to couple various functions used to track the moving boundary of different sub-problems. Moreover, adding the effect of convection imposed by the fluid flow increases the system's complexity. Elaborating these challenges from a mathematical point of view will facilitate future contributions to constructing such models.

2.2 Specific objectives

Despite the advantages of using biodegradable metals in implant design, their fast degradation and uncontrolled release remain a challenge in practical applications. A validated computational model of the degradation process can facilitate the tuning of biodegradation properties. In this doctoral project, a physicochemical model was developed by deriving a mathematical model of the chemistry of biodegradation of Mg and implementing its 3D computational model using the finite element method. To accomplish this, the project was divided into five main objectives, illustrated schematically in Fig. 2.1.

Objective 1 was with the development of the core biodegradation model. For this purpose, a physicochemical model of the biodegradation process of commercially-pure Mg was developed by constructing a mathematical model formulating the mass transfer phenomena and tracking the location of the implant's surface during degradation. For the mass transfer model, a set

of time-dependent reaction-diffusion-convection partial differential equations were derived from the chemistry of biodegradation of the Mg in saline (NaCl) and buffered (SBF) solutions, which usually includes the oxidation of the metallic part, reduction of water and oxygen, changes in local and global pH, and formation of a protective film on the surface of the scaffold which contributes to a slower rate of degradation. Besides these aspects, it was also crucial to consider the effect of different ions in the medium on the degradation rate. Additionally, investigating the structural changes of the scaffolds and implants in practical applications like the resorption of temporary fixation devices, requires tracking the movement of the corrosion surface. This was done by constructing an equation based on the level-set principle, which captured the movement of the medium-metal interface by defining an implicit surface. The derived equations were coupled and solved using the finite element method. The degradation data to validate the models were collected from immersion tests. The model parameters were calibrated using a Bayesian optimization algorithm, and the obtained parameters were used to simulate the pH changes in NaCl and SBF solutions.

Objective 2 was the coupling of corresponding equations of fluid flow (Navier-Stokes and Stokes equations) in the solution domain with the biodegradation model to capture the effect of convection on the degradation process. This was crucial in order to consider the conditions in perfusion bioreactors and hydrodynamics experiments. The main challenge for this step was the complexity of dealing with the finite element formulation of fluid flow equations and the difficulty of defining proper fluid boundary conditions on an implicit interface (the corrosion front).

The **third objective** was to couple the degradation model with the tissue growth models to simulate the response of the surrounding tissue during the biodegradation process. For doing this, a detailed tissue growth model was developed using two different interface tracking techniques, the phase-field and level-set methods, and the results and efficiency of both methods were compared. The mathematical coupling of the degradation and tissue growth models and validating their predictions remained a challenge in this objective.

The **fourth objective** was related to the optimization of the computational aspects of the thesis with all the codes developed in-house using open-source tools and libraries. Detailed work on the parallelization of the computational models of the three previous objectives was carried out to make the developed models run faster. As the required high accuracy on the moving interface increases computation time, parallelization was crucial for the computational models to decrease the execution time of the simulations. The parallel algorithm was implemented using a domain decomposition method. Besides this, the formed linear system of equations in each parti-

tion of the mesh was solved using Krylov methods by taking advantage of available highly efficient preconditioners and iterative solvers, and the scaling behavior with respect to the available computational resources was measured for different components of the models.

The **fifth objective** was the demonstration of the versatility of the developed model by using it as the biodegradation compartment in several multiphysics use-cases to demonstrate the ability of the model to be integrated into other modeling workflows for biomedical applications. In the performed studies, the biodegradation model was combined with structural mechanics and topology optimization codes to deliver a more comprehensive model of the underlying phenomena. The case studies presented in this thesis include mechanical loosening of mandibular bone plates, degradation of an optimized acetabular cup implant, and mechanical integrity of infilled structures.

2.3 Thesis outline

The objectives mentioned in Section 2.2 are tackled in the chapters ahead in the following order and structure:

Chapters 3 and 5 describe the development of the core biodegradation model of **Objective 1**. In **Chapter 3**, a basic biodegradation model is described, which is the base for combining the model with more physics in different applications. **Chapter 5** further develops the base model to include more advanced chemistry from the biodegradation of Mg in more complex electrolytes and conditions.

Chapter 4 describes the development of the fluid flow model used for the simulation of hydrodynamics conditions, which is related to **Objective 2** for coupling the biodegradation model with flow problems. The output coupled model is later used in **Chapter 5** for validating the biodegradation model in hydrodynamics conditions.

The work presented in **Chapter ??** is related to **Objective 3**, in which a tissue growth model is developed to be coupled with the biodegradation model. A simplified tissue growth model is also developed and used in **Chapter ??**, where the rate of bone healing is modeled during the degradation of a mandibular plate, leading to loss of mechanical strength.

Works related to **Objective 4** are presented in **Chapters ??, ??, and ??**, in which the details of software development and model parallelization are elaborated. **Chapter ??** discusses the steps and details of parallelization of the implemented biodegradation model, which can be generalized as a free boundary problem coupled with reaction-diffusion systems. As part of this objective, the developed biodegradation model was transformed into a

multifunctional 3D code called BioDeg, the details of which are described in **Chapter ??**. Additionally, the workflow and routines used to calibrate the models and estimate the unknown parameters are presented in **Chapter ??**, which were also published as educational materials. Furthermore, some parallel scaling behavior results and discussion of the biodegradation model are presented in **Chapter ??**.

In the end, **Chapters ??, ??, and ??** are related to **Objective 5**, dedicated to demonstrating some of the applications of the developed biodegradation model. **Chapter ??** presents the work done to combine the degradation model with the output of a surrogate model, in which the degradation behavior of a patient-specific porous acetabular implant was investigated. **Chapter ??** describes the coupling of the degradation model with a topology optimization code, in which the change of stiffness of some infilled structures was modeled during the degradation process. Lastly, in **Chapter ??**, the biodegradation model was used to predict the rate of mass loss for a mandibular plate, which was subsequently converted to a mechanical strength analysis model to examine how the plate characteristics react to degradation.

To facilitate the structure of the thesis, the chapters related to **Objectives one to three** are grouped in **Part 2** “Model Development”, the chapters related to **Objective 4** are presented in **Part 3** “Code Implementation and Software Development”, and the chapters related to **Objective 5** are presented in **Part 4** “Model Applications”.

Chapter 3

Developing the core computational model

This chapter is based on previously published content in *Corrosion Science*:

M. Barzegari, D. Mei, S. V. Lamaka, and L. Geris, “Computational modeling of degradation process of biodegradable magnesium biomaterials,” *Corrosion Science*, vol. 190, p. 109674, 2021.

Despite the advantages of using biodegradable metals in implant design, their uncontrolled degradation and release remain a challenge in practical applications. A validated computational model of the degradation process can facilitate tuning implant biodegradation properties. In this study, a mathematical model of the chemistry of magnesium biodegradation was developed and implemented in a 3D computational model. The parameters were calibrated by Bayesian optimization using dedicated experimental data. The model was validated by comparing the predicted and experimentally obtained pH change in saline and buffered solutions, showing maximum 5% of difference, demonstrating the model’s validity to be used for practical cases.

3.1 Introduction

3.1.1 Magnesium biodegradation

Due to their bio-friendly properties, biodegradable metallic biomaterials, including magnesium (Mg), iron (Fe), and zinc (Zn), are regaining attention in recent years [2]. These biomaterials find important applications in the design and manufacturing of supportive implants such as temporary devices in or-

thopedics and the cardiovascular field [5, 71]. In orthopedics, the biodegradable metallic biomaterials are used as fixation devices, providing adequate support in the early stages while being absorbed gradually during the bone healing process [72]. Implants fabricated using Mg and its alloys are being used for such a purpose [73] due to the similarity of the stiffness between natural bone and Mg, which helps to reduce the stress shielding induced by the implanted device. Additionally, Mg is reported to have a non-toxic contribution to the human body's metabolism and the bone healing process, which makes the release and absorption of metallic ions safe and biocompatible [74].

Accumulation of mechanistic understanding of Mg degradation achieved by experimental approaches over the years gradually provided a mechanistic understanding of the biodegradation process. Combining these insights with *in silico* modeling approaches enables researchers to study the biodegradation properties and behavior of the implant in a virtual environment prior to conducting any *in vitro* or *in vivo* tests. When fully validated, computational modeling can (in part) replace certain stages of costly and time-consuming experiments verifying the expected degradation behavior of the designed implants. Additionally, the developed models can be efficiently combined with existing computational models to examine other related phenomena such as tissue growth or mechanical integrity.

3.1.2 Computational modeling of Mg degradation

Previous contributions to the computational modeling of the degradation process include a wide range of different approaches, from the basic phenomenological implementations to comprehensive mechanistic models that take into account various aspects of the degradation and resorption process.

Continuous damage (CD) modeling has always been a common approach for corrosion simulation, but from a physicochemical point of view, it focuses on the mechanical integrity of the degradation and neglects the diffusion process. As a result, its application in the degradation modeling of biomaterials, which includes various fundamental phenomena such as mass transfer through diffusion and reaction, is relatively limited. Despite this issue, a CD model proposed by Gastaldi et al. showed a good performance for simulation of bioresorbable Mg-based medical devices [63], in which geometrical discontinuities were interpreted as the reduction of material.

Alternatively, mathematical modeling using transport phenomena equations has shown great flexibility in capturing different mechanisms involved in the biodegradation process. As an example, in Ahmed et al., a set of mathematical equations in cylindrical and spherical coordinates was derived to model the chemical reactions of Mg degradation [65]. Despite the simplic-

ity of their approach from the computational perspective, their model was able to demonstrate the contribution of various chemical components to the *in vitro* degradation of Mg. Similarly, Grogan et al. developed a mathematical model based on the Stefan problem formulation in 1D space to correlate the mass flux of metallic ions into the solution to the velocity of shrinkage of the material during degradation [66]. This was done by considering the mass diffusion and change of the concentration of Mg²⁺ ions, and then, employing an arbitrary Eulerian-Lagrangian (ALE) approach to extend the model to 3D on an adaptive mesh. A similar approach was taken by Shen et al. to develop a theoretical model of the degradation behavior of Mg-based orthopedic implants showing great consistency with *in vitro* test results [67].

An ultimate application of the computational modeling of the biodegradation process of biomaterials can be the prediction of how biodegradation affects the shape of the bulk material, medical device, or implant over time. One of the ways to achieve such a prediction is to capture the movement of the corrosion front mathematically using an appropriate method. The level set method (LSM) is a widely used example in this regard, which is an implicit mathematical way of representing the moving interfaces. This approach was used in Wilder et al. to study galvanic corrosion of metals [75]. They employed LSM on an adaptive mesh to track the moving corrosion interface, but their model lacked a thorough validation using experimental data. Gartzke et al. also worked on a simplified representation of the interface movement by developing a mechanochemical model of the biodegradation process, which helped them to study the effect of degradation on the mechanical properties [62]. They performed a basic qualitative validation on the predictions made by the model. Another similar study in this regard is the Sun et al. work [76], in which a detailed mathematical model was derived and validated to study the deposition of corrosion products on the surface of materials. This mathematical approach was also employed in the biomedical field by Bajger et al. to study the mass loss of Mg biomaterials during biodegradation [68]. They used LSM as well as a set of reaction-diffusion equations to track the change of geometry, which can be directly correlated to the loss of material. The derived equations were also able to capture the formation of the corrosion film that decreases the rate of degradation. Another comprehensive mathematical model was developed by Sanz-Herreraa et al. to investigate the role of multiple chemical components involved in the *in vitro* degradation of Mg implants [69]. One important drawback of this study was its 2D nature. Although the computational model was capable of studying the effect of multiple components, due to the high number of derived equations, it would be difficult to extend and use the same model for real 3D implants. Additionally, a 2D model cannot capture the full phe-

nomenon of corrosion, and as a result, the validation of the model will be more qualitative. It was shown in the study conducted by Gao et al. [59], where they compared the results of a multi-dimension model of the degradation of cardiovascular stents with those of a single-dimension model, that the number of considered dimensions had an important effect on the model predictions. In the end, it is worth mentioning that no dedicated experiments were performed in the aforementioned studies to validate the constructed mathematical and computational models.

The current study focuses on developing a physicochemical model of the biodegradation process of commercially-pure (CP) Mg biomaterials by continuing the work of Bajger et al. [68]. In this model, a set of partial differential equations (PDE) was derived according to the underlying chemistry of biodegradation, described as reaction-diffusion processes taking place at the interface of the biomaterial and its surrounding environment. The formation of a protective layer, effects of the ions in the solution, and the change in the pH due to the corrosion phenomenon were taken into account in the mathematical model. The corresponding computational model was implemented in a fully parallelized manner. Model calibration and validation were executed using data obtained from the immersion tests performed in saline (NaCl) and simulated body fluid (SBF) solutions.

3.2 Background theory

3.2.1 Biodegradation as a reaction-diffusion system

The biodegradation process can be considered as a reaction-diffusion system [77], in which the ions are released due to the chemical reactions on the surface, and the released ions diffuse through the surrounding solution and materials. These ions can interact with other ions and form new compounds [35]. As the reaction-diffusion systems have been studied in science and engineering for a couple of decades, the analogy with a reaction-diffusion system makes it convenient to construct a mathematical model of the biodegradation process based on the well-established transport phenomena equations [78]. From the mathematical perspective, a reaction-diffusion system is expressed by a set of parabolic PDEs that describe the conservation of contributing chemical species in the studied system.

3.2.2 Moving boundary - Stefan problems

Moving boundary problems, also called Stefan problems, are the general class of mathematical problems in which the boundary of the domain should also be calculated in addition to the solution of the other equations [79]. Coupling the reaction-diffusion system of biodegradation with a moving boundary problem constructs a mathematical model in which the change of the domain geometry due to the material loss can be correlated to the underlying reaction and diffusion processes of corrosion. As the geometry can be determined accurately, this approach provides a way to measure the mass loss directly by computing the change in the volume of the material. In such a system, the moving boundary is the material-solution interface (corrosion front).

For a 1D corrosion diffusion system, the position of the diffusion interface can be determined by [79]:

$$s(t) = s_0 + 2\alpha\sqrt{t}, \quad (3.1)$$

in which the $s(t)$ represents the position at any given time, and s_0 is the initial interface position. α coefficient can be calculated using:

$$\alpha = \frac{[Mg]_0 - [Mg]_{sat}}{[Mg]_{sol} - [Mg]_{sat}} \sqrt{\frac{D}{\pi}} \frac{\exp\left(\frac{-\alpha^2}{D}\right)}{\operatorname{erfc}\left(\frac{-\alpha}{\sqrt{D}}\right)} \quad (3.2)$$

where $[Mg]_{sol}$ is the concentration in the solid bulk (i.e. materials density) and $[Mg]_{sat}$ is the concentration at which the material is released to the medium. $[Mg]_0$ represents the initial concentration of the metallic ions in the medium, which is usually zero for most corrosion cases.

Eqs. 3.1 and 3.2 can be used to simply track the movement of the corrosion front, which is the employed method in studies like the Gorgan et al. work [66], but apparently, the real-world corrosion problems are 3D and much more complex than the described system.

As will be described later, Eq. 3.1 is used strictly for the first time step of the simulations in low diffusion regimes for calculating the initial velocity of the interface. Generally speaking, a more sophisticated approach, such as the level set method, is required for tracking the interface of complex 3D geometries.

3.2.3 Level-set method

In the current study, the corrosion front is tracked using an implicit function such that the zero iso-contour of the function represents the metal-solution

interface. As a common practice, this implicit function is expressed as a signed distance function that defines the distance of each point of space (the domain of interest) to the interface. Such a definition implies that the zero iso-contour of the function belongs to the interface. The level set method provides an equation to declare such an implicit function, $\phi = \phi(\mathbf{x}, t)$, $\mathbf{x} \in \Omega \subset \mathbb{R}^3$, which can be obtained by solving [80]:

$$\frac{\partial \phi}{\partial t} + \vec{V^E} \cdot \nabla \phi + V^N |\nabla \phi| = b\kappa |\nabla \phi| \quad (3.3)$$

in which $\vec{V^E}$ is the external velocity field, and V^N is the value of the normal interface velocity. The last term is related to the curvature-dependent interface movement and is omitted. As the effect of perfusion is neglected in the current study, the term containing the external velocity is also eliminated, resulting in the following simplified form of the level set equation:

$$\frac{\partial \phi}{\partial t} + V^N |\nabla \phi| = 0. \quad (3.4)$$

By having the normal velocity of the interface (V^N) at each point and solving Eq. 3.4, the interface can be captured at the zero iso-contour of the ϕ function.

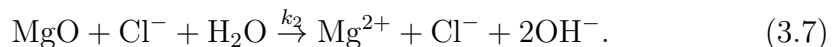
3.3 Materials and methods

3.3.1 Underlying chemistry

The chemistry of biodegradation of Mg depends considerably on the surrounding solution and the presence of certain ions [35]. In NaCl solutions, the anodic and cathodic reactions as well as the formation and elimination of side corrosion products can be considered as follows [2]:



Reaction 3.6 is not fully correct from the chemical point of view. In fact, Mg surface is always covered by MgO layer, and Mg(OH)₂ forms on top of that either at atmospheric conditions or during the immersion. The integrity of this MgO layer is undermined by Cl⁻ ions, leading to an increase in degradation rate:



Although Cl^- formally does not participate in reaction 3.7, it reflects the dependence of Mg corrosion rate on Cl^- concentration. This effect on the rate of degradation has been widely expressed as the effect of Cl^- on the Mg(OH)_2 in the literature [2, 5]. In the developed model, this effect is used interchangeably by omitting the MgO component, so the protective film formed on the corrosion interface is assumed to contain Mg(OH)_2 only. Moreover, it has been shown recently that oxygen reduction reaction also takes place during corrosion of Mg [33, 81, 82]. However, this is a secondary reaction (complementing water reduction) contributing to 1-20% of the total cathodic current depending on the conditions. Hence, it is not taken into consideration in this model. Additionally, the involved chemical reactions are more complicated in SBF solutions due to the presence of further inorganic ions and the formation of a layered precipitate structure [35], but the effect of these ions is currently encapsulated in the reaction rates and the diffusion coefficients of the developed mathematical model. The summary of the considered chemistry to develop the mathematical model is depicted in Fig. 3.1.

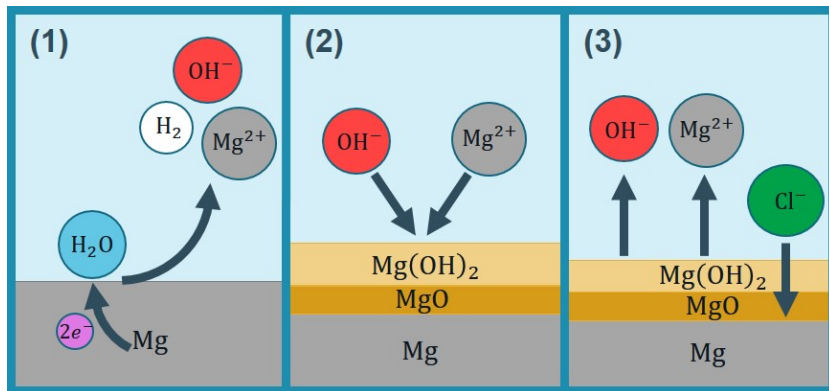


Figure 3.1: The chemistry of biodegradation of Mg considered in the current study: 1) Mg oxidation and water reduction processes accompanied by releasing Mg^{2+} and OH^- ions as well as H_2 gas, 2) formation of a partially protective precipitation layer, 3) dynamic solubility equilibrium and contribution of Cl^- .

3.3.2 Mathematical modeling

To keep track of the concentration changes of various contributing chemical components, we define four state variables for the concentration of Mg^{2+} ions, protective film (Mg(OH)_2), chloride (Cl^-) ions, and the hydroxide (OH^-)

ions:

$$\begin{aligned} C_{\text{Mg}} &= C_{\text{Mg}}(\mathbf{x}, t), & C_{\text{Film}} &= C_{\text{Film}}(\mathbf{x}, t) \\ C_{\text{Cl}} &= C_{\text{Cl}}(\mathbf{x}, t), & C_{\text{OH}} &= C_{\text{OH}}(\mathbf{x}, t) \quad \mathbf{x} \in \Omega \subset \mathbb{R}^3, \end{aligned} \quad (3.8)$$

which are indeed 4 scalar functions of space and time. Ω denotes the whole region of interest, including both the Mg bulk and its surrounding medium. By doing this, the value of pH at each point of Ω can be calculated as:

$$\text{pH} = 14 + \log_{10} C_{\text{OH}}, \quad (3.9)$$

where C_{OH} implies the activity of OH^- . By having the definition of the state variables in Eq. 3.8, the biodegradation of Mg described by Eqs. 3.5 and 3.6 can be represented as a set of reaction-diffusion PDEs:

$$\frac{\partial C_{\text{Mg}}}{\partial t} = \nabla \cdot (D_{\text{Mg}}^e \nabla C_{\text{Mg}}) - k_1 C_{\text{Mg}} \left(1 - \beta \frac{C_{\text{Film}}}{[\text{Film}]_{\max}} \right) + k_2 C_{\text{Film}} C_{\text{Cl}}^2 \quad (3.10)$$

$$\frac{\partial C_{\text{Film}}}{\partial t} = k_1 C_{\text{Mg}} \left(1 - \beta \frac{C_{\text{Film}}}{[\text{Film}]_{\max}} \right) - k_2 C_{\text{Film}} C_{\text{Cl}}^2 \quad (3.11)$$

$$\frac{\partial C_{\text{Cl}}}{\partial t} = \nabla \cdot (D_{\text{Cl}}^e \nabla C_{\text{Cl}}) \quad (3.12)$$

$$\frac{\partial C_{\text{OH}}}{\partial t} = \nabla \cdot (D_{\text{OH}}^e \nabla C_{\text{OH}}) + k_2 C_{\text{Film}} C_{\text{Cl}}^2 \quad (3.13)$$

in which the maximum concentration of the protective film can be calculated according to its porosity (ϵ) [68]:

$$[\text{Film}]_{\max} = \rho_{\text{Mg(OH)}_2} \times (1 - \epsilon). \quad (3.14)$$

D^e is the effective diffusion coefficient for each component. Due to the formation of the protective film, the diffusion coefficient is not constant and varies from the actual diffusion coefficient of the ions to a certain fraction of it. This fraction can be defined as ϵ/τ [83,84], in which ϵ and τ are the porosity and tortuosity of the protective film, respectively. The effective diffusion coefficient can be then calculated by interpolating the two aforementioned values:

$$D_i^e = D_i \left(\left(1 - \beta \frac{C_{\text{Film}}}{[\text{Film}]_{\max}} \right) + \beta \frac{C_{\text{Film}}}{[\text{Film}]_{\max}} \frac{\epsilon}{\tau} \right). \quad (3.15)$$

The β coefficient is called momentum here and controls the effect of the saturation term $(1 - \frac{C_{\text{Film}}}{[\text{Film}]_{\max}})$.

3.3.3 Interface movement formulation

In order to take advantage of the level set method for tracking the corrosion front, the velocity of the interface at each point should be determined. Then, by solving Eq. 3.4, the interface is obtained at the points with a zero value of the ϕ function. The interface velocity in mass transfer problems can be calculated using the Rankine–Hugoniot equation [85], and by considering the transportation of Mg²⁺ ions, it can be written as:

$$\{\mathbf{J}(x, t) - ([\text{Mg}]_{\text{sol}} - [\text{Mg}]_{\text{sat}}) \mathbf{V}(x, t)\} \cdot n = 0 \quad (3.16)$$

where \mathbf{J} is the mass flux at the interface. Rearranging Eq. 3.16 and inserting the value of the normal interface velocity into Eq. 3.4 yields:

$$\frac{\partial \phi}{\partial t} - \frac{D_{\text{Mg}}^e \nabla_n C_{\text{Mg}}}{[\text{Mg}]_{\text{sol}} - [\text{Mg}]_{\text{sat}}} |\nabla \phi| = 0, \quad (3.17)$$

which is the final form of the level set equation to be solved. In the case of simulations with a low diffusion rate, the interface moves slowly in the beginning, which results in a linear degradation, whereas based on the experimental results, the degradation rate is fast at the beginning and slows down eventually [36]. So, to mimic the same behavior in the low diffusion regimes, we took advantage of the theoretical Stefan formulation (Eqs. 3.1 and 3.2) to push the interface in the first time step. According to Eq. 3.1, the velocity of the interface can be calculated as $(2\alpha/\sqrt{t})$, but as we are dealing with a 3D model and not a 1D one, we pick a fraction (denoted by γ) of this ideal value to be used as the driving force of the interface at the beginning of the simulation. So, the normal velocity of the interface can be written in the general form as:

$$V^N(x, t) = \begin{cases} \gamma \frac{2\alpha}{\sqrt{t}} & t = 0 \\ \frac{D_{\text{Mg}}^e \nabla_n C_{\text{Mg}}}{[\text{Mg}]_{\text{sol}} - [\text{Mg}]_{\text{sat}}} & t > 0 \end{cases} \quad (3.18)$$

in which the α value should be calculated from Eq. 3.2. By selecting γ equal to zero, the Stefan formulation can be eliminated, and a value of 1 for γ restores the ideal 1D velocity definition.

3.3.4 Boundary conditions

The implementation of boundary conditions is relatively challenging and complex for the developed model as they should be imposed inside the domain of interest on virtual interfaces defined by mathematical expressions

(i.e. on the moving interface defined by the zero iso-contour of the level set equation). The penalty method was used to overcome this issue and define the desired boundary conditions on the moving corrosion front.

Fig. 3.2 demonstrates a schematic presentation of the boundary conditions and general considerations of each PDE of the biodegradation mathematical model. This figure is divided into 5 different parts, presenting the 5 PDEs of the model. The Mg block is depicted in the center, and the interface separates it from the surrounding medium. There is no specific boundary condition for the level set and film formation equations, but in comparison to the other 3 transport equations, it should be noted that diffusivity is not considered for Mg(OH)_2 , which is also reflected in Eq. 3.11. The level set function ϕ is defined in a way that is positive inside and negative outside the solid region. For the Mg^{2+} ions transport equation, a Dirichlet boundary condition is applied on the mathematical interface to make the concentration equal to the saturation concentration of Mg^{2+} ions, a value that was already used in Eq. 3.17. For the Cl^- and OH^- ions transport equations, a no-flux boundary condition is applied to the interface by making the diffusion coefficient equal to zero inside the Mg block, preventing ions to diffuse inside the solid material.

3.3.5 Implementation

To simulate the developed mathematical model, which is comprised of Eqs. 3.10, 3.11, 3.12, 3.13, and 3.17, a combination of finite difference and finite element methods was used, leading to discrete forms of these equations, which were subsequently solved using appropriate linear solvers.

To discretize the temporal terms of the aforementioned parabolic PDEs, a first-order backward Euler finite difference scheme was used, whereas the spatial terms were converted to a weak form using a standard first-order finite element scheme. Then, the open-source PDE solver FreeFEM [86] was used to implement the weak form and obtain a linear system of equations for each PDE. The obtained linear systems were solved in parallel using the HYPRE preconditioner [87] and the GMRES solver [88] via the open-source high-performance computing (HPC) toolkit PETSc [89]. Additionally, to increase the efficiency of the computation and decrease the simulation execution time, the computational mesh was decomposed and distributed among available computing resources using the interface of HPDDM package in FreeFEM [90]. The details of this implementation are presented in Chapter ???. A simple iterative solver based on the Newton method was also developed to solve Eq. 3.2 to obtain the value of α parameter if it was required in the simulations.

The computational mesh was generated using a set of first-order tetrahe-

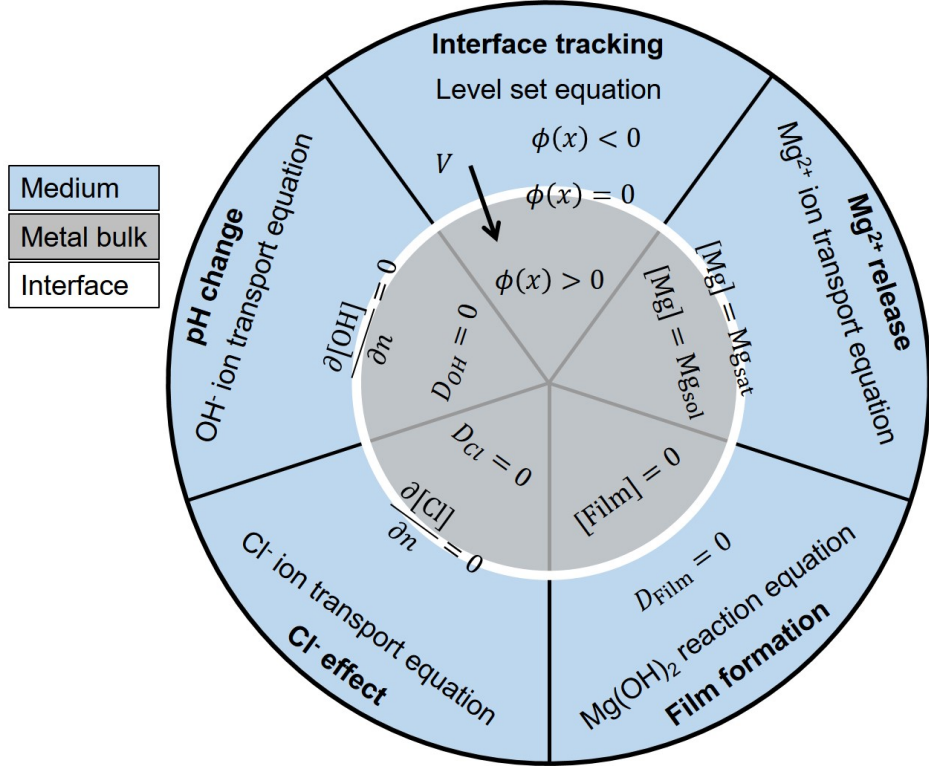


Figure 3.2: A schematic overview of the exposed boundary conditions and constraints required for the simulation of each equation of the developed mathematical model for Mg biodegradation.

dral elements and was adaptively refined on the metal-solution interface to increase the numerical accuracy of the simulation of the level set equation (Eq. 3.17). The Netgen mesh engine [91] in the SALOME platform [92] was used to generate the mesh.

Similar to the technique employed by Bajger et al. [68], the gradient of concentration of Mg²⁺ in Eq. 3.17 was calculated at a distance h in the normal direction from the interface, with h being the smallest element size of the mesh:

$$\nabla_n C = \frac{C(\mathbf{x} + h.n) - C(\mathbf{x} + 2h.n)}{h} \quad \mathbf{x} \in \Omega \subset \mathbb{R}^3. \quad (3.19)$$

Considering the adaptively refined mesh, the h value is very small, so the gradient is computed at the regions close enough to the interface. In addition to this technique, the mass lumping feature of FreeFEM was used to prevent the oscillation of concentration values on the diffusive metal-medium interface.

3.3.6 Experimental setup

The degradation rate of CP Mg was evaluated based on the hydrogen evolution tests performed either in NaCl or SBF solutions with eudiometers. The composition of the electrolytes is shown in the following table (Table 3.1). 0.5 g metallic chips (with a surface area of $47.7 \pm 5.0 \text{ cm}^2/\text{g}$ and chip thickness ca. 200 microns) of CP Mg were put in 500 ml electrolyte for 22-24 hours for monitoring the amount of evolved hydrogen. The method of measuring evolved hydrogen was chosen for monitoring the degradation rate because although such a measurement is prone to experimental errors such as relatively high solubility of hydrogen in water and volume change due to temperature and pressure variations, it provides a continuous assessment of the process, resulting in a continuous and smooth curve. Additionally, as small metallic chips were used for the tests, it was not possible to clean these pieces in chromic acid without losing them to measure the mass loss directly. The drawback of choosing the evolved hydrogen as the monitoring method is that it is not the only occurring reaction since oxygen reduction also takes place during the process [33, 81, 82]. As a result, measuring only hydrogen does not capture the totality of the degradation reactions. However, for CP Mg, the contribution of oxygen reduction is low (in contrast to high-purity Mg [33]) and can simply be ignored, meaning that the evolved hydrogen is an accurate equivalent for the mass loss. The bulk pH of electrolytes before and after corrosion was measured by a pH meter (Metrohm-691, Switzerland). Local pH was measured by positioning pH microprobes (Unisense, Denmark, pH-sensitive tip size 10x50 micron) 50 micron above the surface of Mg and monitoring the pH values either in one spot or by horizontal or vertical line-scans or mapping by following a horizontal grid. The electrolytes were not pH buffered additionally since SBF contains carbonates and phosphates that stabilize the pH at the approximate value of 8.5 instead of the 10.5 characteristic for pure NaCl solutions where pH is stabilized by precipitation of Mg(OH)_2 . Meanwhile, synthetic pH buffers, such as TRIS and HEPES were proven to affect the degradation mechanism rather significantly and should not be used for this purpose [35]. The measurements were performed at room temperature of $22 \pm 2^\circ\text{C}$ maintained by the laboratory climate control system. More detailed information about experimental set up and procedures can be found elsewhere [36, 40].

3.3.7 Parameter estimation

The constructed mathematical model contains some parameters that need to be calibrated prior to final validation of the model: diffusion coefficient of

Table 3.1: Chemical composition of NaCl and SBF electrolytes used to perform hydrogen evolution tests, weight loss, local and bulk pH measurements.

	Concentration / mM	
	0.85 wt. % NaCl	SBF
Na ⁺	145.4	142.0
K ⁺	-	5.0
Mg ²⁺	-	1.5
Ca ²⁺	-	2.5
Cl ⁻	145.4	147.8
HCO ₃ ⁻	-	4.2
HPO ₄ ²⁻ /H ₂ PO ₄ ⁻	-	1.0
SO ₄ ²⁻	-	4.2
Synthetic pH buffer (i.e. Tris/HCl, HEPES)	No	No
Initial pH value	5.6-5.9	7.35-7.45

Mg²⁺ and Cl⁻ ions (D_{Mg} and D_{Cl} to be inserted into Eq. 3.15 to get effective diffusion coefficients), the reaction rates of Eqs. 3.5 and 3.6 (k_1 and k_2), the momentum parameter, β , for controlling the saturation term behavior (in Eqs. 3.10, 3.11, and 3.15), and the γ parameter for the initial interface velocity (Eq. 3.18). An inverse problem setup was required to estimate the proper value of these parameters.

Performing a parameter estimation requires running the computational models several times. Considering the computationally-intensive model of the current study, a sensitivity analysis was performed prior to the parameter estimation to exclude non-essential parameters and reduce the time required to complete the inverse problem run. This sensitivity analysis was accomplished separately in the low diffusion (similar to the SBF solution) and high diffusion (similar to NaCl solution) regimes.

After determining the essential parameters to include, a Bayesian optimization approach [93] was used to construct the inverse problem and calibrate the parameters. The reason for choosing a Bayesian approach was to minimize the number of optimization iterations, in each of which the simulation should run once. The Bayesian optimization is a more efficient option for such computational intensive cases in comparison to gradient-based or fully-stochastic methods as it takes into account all the preceding iterations in a probability tree [94].

The objective function of the optimization problem was the difference between the predicted and experimentally obtained values of evolved hydrogen.

In the computational model, the evolved hydrogen can be computed directly at any time through the mass loss as each mole of corroded Mg is correlated to one mole of released hydrogen (Eq. 3.5). The mass loss can be obtained using the following volume integral:

$$Mg_{\text{lost}} = \int_{\Omega_+(t)} [Mg]_{\text{sol}} dV - \int_{\Omega_+(0)} [Mg]_{\text{sol}} dV, \quad (3.20)$$

where $\Omega_+(t) = \{\mathbf{x} : \phi(\mathbf{x}, t) \geq 0\}$, and then, the amount of produced hydrogen is calculated using the ideal gas law:

$$H_f = \frac{Mg_{\text{lost}}}{Mg_{\text{mol}}} \frac{RT}{P} \quad (3.21)$$

in which R , P , T , Mg_{mol} are the universal gas constant, the pressure, the medium temperature, and the molar mass of Mg, respectively.

3.3.8 Simulation setup

In order to simulate the developed mathematical model, the experimental setup was reconstructed *in silico* with some minor differences. As there is no perfusion in the solution chamber, the mixing effect was neglected, so, as can also be seen in the mathematical model, the advection terms were not considered. Furthermore, the experiments were conducted using small metallic chips, yet, as the biodegradation behavior heavily depends on the exposed surfaces, we represented these chips by a cuboid with the same surface-to-mass ratio. By considering the approximate surface-to-mass of $50\text{cm}^2/\text{g}$ and the total mass of 0.5g , the chips were replaced by a cuboid with the size of $60\text{mm} \times 21\text{mm} \times 0.2\text{mm}$, which approximately has the same ratio, surface area, volume, and mass. Also, the solution chamber with a capacity of 500ml was represented by a cubic container with an edge size of 80mm . Fig. 3.3 depicts the constructed geometry as well as the computational mesh generated to represent it. The mesh is refined on the interface and contains 18,049,471 elements, resulting in 3,077,227 degrees of freedom (DOF) for each PDE.

Simulations were carried out on the VSC (Flemish Supercomputer Center) supercomputer. Taking advantage of HPC techniques to parallelize the simulation is an inevitable aspect of such a computational-intensive model, so based on what described in the implementation section, the mesh was decomposed among 170 computing cores, i.e. 24,137 DOF per core (which includes the ghost nodes to satisfy the boundary condition in each sub-mesh). On the VSC supercomputer, we made use of 5 nodes, 36 cores each, each

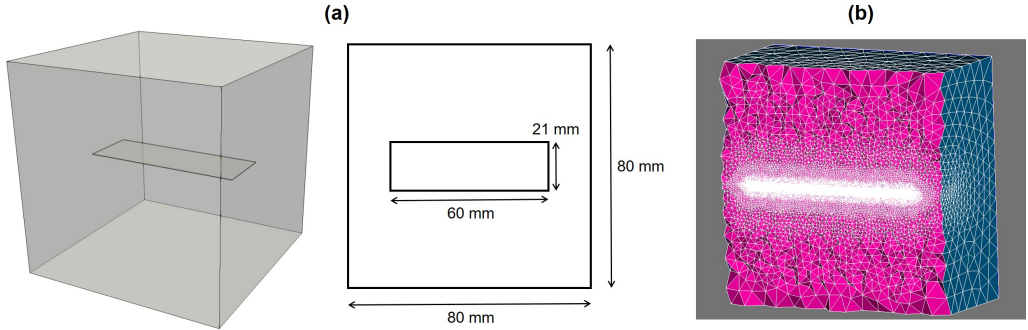


Figure 3.3: Computational representation of the experimental set-up, used to perform parameter estimation and numerical validation of the developed model. a) A cuboid of Mg ($60\text{mm} \times 21\text{mm} \times 0.2\text{mm}$) inside a solution, b) a cross-section of the computational mesh, refined on the corrosion front to increase the required level set accuracy.

node holding CPUs with a clock speed of 2.6 GHz, with 960 GB of the total available memory.

The OH^- transport equation (Eq. 3.13) was not solved during the parameter calibration process. Afterwards, two full simulations (for the NaCl and SBF solutions) were conducted to calculate the pH changes based on the change of the concentration of OH^- ions in the medium. This acted as the validation of the numerical model because no calibration was performed on the output of this equation. The pH was calculated using Eq. 3.9, based on the solution of Eq. 3.13 and a reported value of $7.00e \times 10^{-5}\text{cm}^2/\text{s}$ ($25.2\text{mm}^2/\text{hour}$) for the diffusion coefficient of OH^- ions (D_{OH} to be used in Eq. 3.15) in aqueous solutions [95].

According to the experimental setup, the initial concentration of the Mg^{2+} , Cl^- , and OH^- ions were set to 0 (no Mg^{2+} ions at the beginning), 146mM ($5.175 \times 10^{-6}\text{g/mm}^3$), and $1 \times 10^{-7}\text{g/mm}^3$, respectively. The porosity (ϵ) and tortuosity (τ) of the protective film were considered to be 0.55 and 1, respectively [76]. The saturation concentration $[\text{Mg}]_{\text{sat}}$ was set to the solubility of magnesium chloride in water, which is $134 \times 10^{-6}\text{g/mm}^3$ at 25°C [96]. The density of Mg ($[\text{Mg}]_{\text{sol}}$) and $\text{Mg}(\text{OH})_2$ were set to $1735 \times 10^{-6}\text{g/mm}^3$ and $2344 \times 10^{-6}\text{g/mm}^3$, respectively [68]. A time step convergence study was performed to determine the implicit time step size. Based on the results, a time step with a size of 0.025 hours was chosen. The overall simulated time is 22 hours in accordance with the experimental design of performed immersion tests.

3.3.9 Case study

To further investigate the predictions of the current model on more complex shapes, the biodegradation of a simple screw was studied in the SBF solution using the parameters obtained for the low diffusion regimes. Similar to the simulation of Mg cuboid, the mesh was refined on the metal-medium interface, and it consisted of 1,440,439 elements with 246,580 DOFs for each PDE. All the simulation parameters and materials properties were identical to the simulation of biodegradation in the SBF solution, and the target was to simulate 42 days (1008 hours) of the process. This was selected as a sufficiently long simulated time to observe the effects of biodegradation on larger time scales. The goal of this case study is to demonstrate the applicability of the developed model for any desired 3D shape with no geometrical limitations. As a result, although it was possible to consider a more complicated geometry for the screw (for example by considering threads around the cylindrical part of the screw or having a realistic geometry for the head), the screw geometry consists of basic 3D primitives, which are adequate for the mentioned purpose.

3.4 Results

3.4.1 Optimization results

Based on the performed sensitivity analysis, two parameter sets were obtained for the high diffusion (in NaCl solution) and low diffusion (in SBF solution) simulations, respectively. These parameters are listed in Table 3.2. According to the results, the reaction rate of Eq. 3.5 (k_1), which demonstrates the rate of oxidation-reduction, has less contribution to the process in comparison to the rate of the weakening of the protective film (k_2). Because of this, the parameter k_1 was not selected for the parameter estimation. Also, the model was sensitive to the effect of parameter k_2 in different ranges of values and not on a specific point, and as a result, three constant values were chosen as the delegates of these ranges in the optimization process. The model was not sensitive to the diffusion rate of Cl^- ions, which was also expected because although Cl^- has an important role in the weakening of the partially protective MgO film, its transport equation (Eq. 3.12) is purely diffusive and does not include any reaction term.

The parameter optimization process was performed on the specified range of selected parameters, while the rest of the parameter values were obtained from the literature [68,95]. Table 3.3 shows the output of this process, which was used to simulate the full model. For two estimation processes, 120 opti-

Table 3.2: The effective parameters as the result of the sensitivity analysis and their corresponding range to be considered in the Bayesian optimization for parameter calibration

	Parameter	Optimization range
Low diffusion (SBF solution)	D_{Mg}	[0.0001, 0.01]
	k_2	$10^{10}, 10^{15}, 10^{20}$
	β	[0.1, 10]
	γ	[0, 1]
High diffusion (NaCl solution)	D_{Mg}	[0.003, 0.1]
	k_2	$10^{10}, 10^{15}, 10^{20}$
	β	[0.1, 10]

Table 3.3: Values used to evaluate the model performance, obtained from the output of the optimization process and the literature.

Parameter	D_{Mg}	D_{Cl}	D_{OH}	k_1	k_2	β	γ
Unit	$\frac{\text{mm}^2}{\text{hour}}$	$\frac{\text{mm}^2}{\text{hour}}$	$\frac{\text{mm}^2}{\text{hour}}$	$\frac{1}{\text{hour}}$	$\frac{\text{mm}^6}{\text{g}^2 \text{hour}}$	-	-
SBF solution	0.000338	0.05	25.2	7	10^{15}	0.125	0.65
NaCl solution	0.06273	0.05	25.2	7	10^{20}	0.2	0

mization iterations were taken cumulatively, which took 276 hours of simulation execution time using 170 computing nodes for each simulation.

3.4.2 Degradation prediction

Fig. 3.4 shows the model output for the predicted produced hydrogen, protective film formation, and the pH changes. The graph of the evolved hydrogen is used as input during the parameter optimization process, but the pH results are produced by the simulations using the optimized parameters to demonstrate the validation of the developed mathematical and computational models. The predicted pH result (Fig. 3.4-d) shows a difference of 5.35% for the simulation in NaCl and 1.03% for SBF simulation. Each simulation took about 3 hours to complete.

In Fig. 3.4, a post-processed view of the final shape of the Mg cuboid in the NaCl solution is presented, in which the degraded geometry is plotted on the Mg^{2+} ions (Fig. 3.4-b) and protective film concentration (Fig. 3.4-c) contours. A transparent contour of the pH values in the solution is depicted for both the NaCl (Fig. 3.4-e) and SBF (Fig. 3.4-f) solutions. The range of colors is kept equal for both contours to make it easy to compare the change

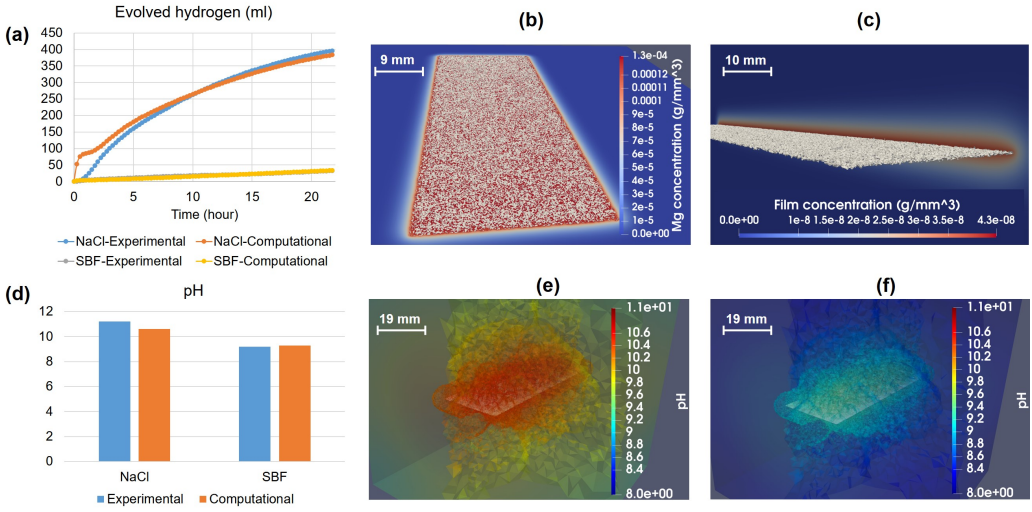


Figure 3.4: Comparing the quantitative output of the model for the rate of degradation and the pH changes in NaCl and SBF solutions with experimentally measured values as well as the simulation results for ion release, mass loss, protective film formation, and pH changes after 22 hours of simulated time: a) calibrated output of the formed hydrogen gas during the degradation (the SBF curves are overlapped), b) the simulation results of Mg^{2+} ions release, c) the simulation results of protective film concentration at the end of the simulation (the color contour shows the concentration of species, and the gray surface is the zero iso-contour of the level set function, which indicates the surface of the Mg block), d) de novo prediction of the global pH changes in the medium, showing a good agreement between the model output and the experimental results, e) pH changes in different regions of the medium in NaCl solution, f) pH changes in SBF solution.

of pH in both solutions.

The concentration values of the state variables of the derived transport PDEs (Mg^{2+} , Cl^- , OH^- , and $Mg(OH)_2$) are plotted along a diagonal line in the solution container in Fig. 3.5, showing how they change in the zones close to the corrosion surface and far from it.

3.4.3 Example application

The simulation of 42 days (19,200 time steps) of the degradation of the simple screw took 9 hours to run using 170 computing cores. Fig. 3.6 depicts the post-processed interface and Mg^{2+} ions release (similar to Fig. 3.4-b) as well as the mass loss during the degradation of the screw in the SBF solution. It

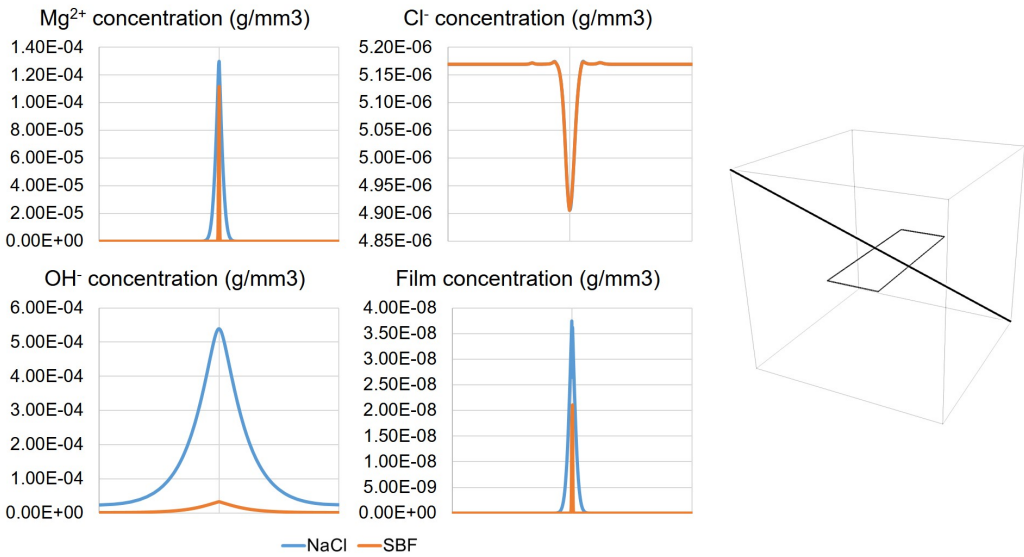


Figure 3.5: The change of concentration for the involved chemical components, Mg^{2+} , Cl^- , OH^- ions, and the protective precipitation structure (which can be correlated to the thickness of the layer) plotted over a diagonal line as shown in the right.

is worth mentioning that the roughness observed on the surface of the screw geometry is related to the node-based visualization of the level-set function evolution and is not caused by either non-uniform corrosion or numerical error in the simulations.

3.5 Discussion

In this study, a physicochemical model of the biodegradation process of commercially-pure Mg was developed by constructing a mathematical model formulating the mass transfer phenomena as well as tracking the location of the surface of the implant during degradation. For the mass transfer model, the equations were derived from the chemistry of biodegradation of the Mg in saline (NaCl) and buffered (SBF) solutions, which includes the oxidation of the metallic part, reduction of water, changes in pH, and formation of a protective film on the surface of the scaffold which contributes to a slower rate of degradation. Beside these aspects, it was also crucial to consider the effect of different ions in the medium on the rate of degradation. Additionally, investigating the structural changes of the scaffolds and implants in practical applications, like resorption of temporary fixation devices, re-

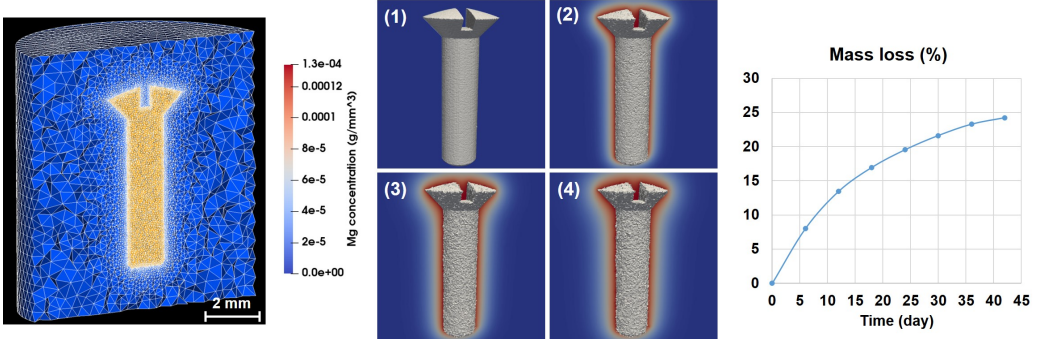


Figure 3.6: A cross-section of the computational mesh and simulation results of the degradation process of the use-case screw in SBF solution as well as the mass loss graph over time. The contours display the concentration of Mg^{2+} ions on a cross-section view of the medium beside the moving surface of the screw at 1) 1st day (initial state), 2) 6th day, 3) 12th day, and 4) 18th day.

quires tracking the movement of the corrosion surface. This was done by constructing an equation based on the level set principle, which captured the movement of the medium-metal interface by defining an implicit surface. The derived equations were coupled and solved using a combination of finite difference and finite element methods. The degradation data to validate the models was collected from immersion tests of small Mg chips, reconstructed as a single cuboid in the computational study with a similar surface over volume properties. The model parameters were calibrated using a Bayesian optimization algorithm, and the obtained parameters were used to simulate the pH changes in NaCl and SBF solutions.

The developed model falls in the categories of physical models of the corrosion process, which provide more insights of the process in comparison to the phenomenological models. The reason is that the phenomenological models focus on the elimination of elements to capture the loss of materials, which makes it impossible to model the formation of new chemical compounds or interaction of species [97]. The physical models, like the one developed in this study, are capable of capturing the underlying chemical interactions. By doing this, processes like the effect of coating, the formation of a protective layer, and pH changes can be modeled. Adding an appropriate interface tracking method enables the physical models to act like the phenomenological models in capturing the corrosion interface movement. In the current study, this has been accomplished using a level set function. Technically speaking, this approach has certain benefits over the ALE method, which is

the method used by several similar studies, including Grogan et al. [66]. In comparison to the ALE method, the level set function tracks the interface instead of a Lagrangian mesh, and elements can freely be marked as solid or liquid. Additionally, employing the ALE method for degradation simulation requires remeshing the geometry as the interface moves, which is not efficient for 3D models and is limited to the available features of the employed numerical solver.

One of the challenging aspects of validating physical models is getting the correct value for the parameters of said models, requiring dedicated experimental input. To overcome this challenge, an efficient inverse problem was constructed based on the Bayesian optimization approach to estimate the unknown parameters. To save time and resources, the parameter estimation process was performed on the most effective parameters, which were selected based on a sensitivity analysis. This selection process implied the importance of parameters in high and low diffusion rates. This included the diffusion coefficients (except the diffusion rate of the hydroxide ion), which were subsequently used in Eq. 3.15 to get the effective coefficient employed in the derived PDEs. The objective function of the optimization process was the difference in the mass loss predicted by the computational model and the experiments, but instead of direct mass loss measurement, we measured the volume of formed hydrogen gas in Mg corrosion, which then was converted to mass loss by considering the stoichiometry of the reactions.

The degradation rate is fast at the beginning, but then it slows down due to the formation of a partially protective film and also because of the saturation concentration. This phenomenon is well captured by the model at high diffusion rates, but in low diffusion rates (in SBF solution), this effect can be reproduced by pushing the corrosion front according to the Stefan formulation of the moving interface problems. This was controlled by the parameter γ (Eq. 3.18). The sensitivity test demonstrated that this parameter doesn't have a significant effect in the high diffusion rates, but for the low diffusion regimes, it was considered in the parameter estimation process. It should be noted that the inclusion of the γ parameter is crucial for short-term simulations only, helping the model mimic the chemical behavior correctly. In other words, the long-term degradation behavior can be successfully simulated without considering the parameter γ . For example, the sensitivity test (Table 3.2) has marked γ as an effective parameter because it plays an important role in the first 22 hours of degradation model behavior. But, for the case study, the result (the graph in Fig. 3.6) would be almost the same with γ set to zero since 40,320 time steps (1008 hours) passed after applying the parameter in the first time step.

For the high diffusion regime simulation, the results show a difference

between the experimental and computational data in the early stages of the degradation process (Fig. 3.4-a). The reason for this behavior lies within Eqs. 3.17 and 3.19, in which the interface velocity was correlated to the gradient of released ions. In high diffusion rates, the material release occurs very fast, so the calculated gradient (Eq. 3.19) vanishes for a short period until the diffusion becomes more uniform. As a result, the interface does not move, and according to Eq. 3.20, no mass loss gets calculated. This effect was automatically ignored in the parameter estimation process since the objective function considers the overall degradation behavior.

The degradation of the CP Mg was assumed to be mostly diffusion-based. As a result, the value of D_{Mg} plays an important role in the behavior of the model. Although it was possible to get the diffusion coefficient of Mg^{2+} from the previously conducted experiments in the literature (similar to what was done for D_{OH}), we decided to not do so because of two reasons: 1) the values reported in the literature are mostly valid for saline solutions only, and 2) the reported values were not in a good agreement with one another [66, 76]. Thus, the diffusion coefficient was obtained using the parameter estimation process for both the NaCl and SBF solutions. The obtained value of D_{Mg} ($0.06273 \text{ mm}^2/\text{hour}$) was in line with the values that Grogan et al. have already suggested ($0.010575 - 0.50575 \text{ mm}^2/\text{hour}$) [66], showing that the constructed inverse problem was successful in reproducing previous results of similar studies. The obtained value of D_{Mg} in the Bajger et al. work [68] is $0.00066 \text{ mm}^2/\text{hour}$, which is mostly related to the simplicity of the employed parameter estimation method as well as having a 2D model instead of a 3D one.

In the *in vitro* biodegradation of Mg-based biomaterials, the local pH of the surrounding solution increases less than that in NaCl solution. This is because the $\text{Mg}(\text{OH})_2$ formed in NaCl stabilizes pH at 10.4 [98], while Mg-Ca-P-C containing products stabilize the pH at 7.8-8.5 since OH^- is consumed for the formation of this product [36, 39]. This phenomenon was captured in Eqs. 3.13 and 3.9 to calculate pH based on the concentration of OH^- ions, showing the local pH changes at any location (Fig. 3.4-e,f). In the current study, the global pH is considered as the validation criterion, which means that the average value of the solution pH is calculated using a volume integral and is compared with the ones obtained from the experiments. Fig. 3.4-d shows that such a prediction has a good agreement with the experimental data.

One of the biggest simplifications of the current study was made by ignoring the contribution of pH changes to the biodegradation mechanism of Mg. Although doing that is relatively simple and straightforward in the approach taken by this study, it results in non-linear terms in the derived PDEs. This

non-linearity inserts another level of complexity to the computational model as the order of the state variables are in the range of 10^{-6} to 10^{-10} , which makes it difficult to yield convergence in the iterative non-linear solvers. By developing a robust non-linear solver, this effect can be added simply by including more relevant terms as the effect of Eq. 3.13 into Eq. 3.10.

Additionally, buffered solutions and the physiological fluids inside the human and animal bodies contain more ions interacting with more complex chemistry [35]. In this study, this effect was encapsulated in a limited number of parameters (such as k_1 and k_2 in Eqs. 3.10, 3.11, and 3.13), but while the results show its success to reproduce experimental observations, it still needs additional elaboration to be able to capture more chemical interactions. For example, SBF solutions contain phosphates, carbonates, and calcium that form hydroxyapatite-like compounds on the surface of Mg, acting as rather strongly blocking corrosion products. In the current state of the developed model, such an effect on the corrosion rate was captured by a low effective diffusion coefficient (Eq. 3.15) for the Mg transport. In future model developments, the effect of presented inorganic ions such as HCO_3^- , $\text{HPO}_4^{2-}/\text{H}_2\text{PO}_4^-$, and Ca^{2+} can be added similar to the way the effect of Cl^- was considered. Additionally, formulating the effect of HPO_4^{2-} that exists in the physiological environments will make the model capable of making more accurate predictions for *in vivo* studies.

A common approach in mechanistic studies is to start with a pure material and gradually increasing complexity by adding impurities and alloying elements. This approach was followed in the current study by beginning with a model for pure Mg that captures the major reactions. The developed model can be further extended to Mg alloys by considering the effect of alloying elements on the reaction rates as well as adding more terms to the transport equations to capture the electrochemical potential changes, converting the PDEs into the Nernst–Planck equation [99]. By doing so, more complex forms of the corrosion process, such as galvanic corrosion, can be predicted by the model. This will increase the applicability of the model for biomedical cases since pure Mg is not commonly used for medical-graded applications. As an additional future development, the corrosion layer can be considered to be heterogeneous, making it possible to simulate the cathodic reactions by randomly distributing more active spots on the surface. Alternatively, a similar effect can be achieved by adapting the degradation rates using polarization curves and introducing an active spot for inhomogeneous anodic dissolution [100]. Applying this will enable the model to take into account additional corrosion products formed due to additional alloying elements such as Zn, Ca, Ag, rare-earth elements, and detrimental cathodic impurities such as Fe.

Although the pH simulations are not enough experimental input to call the model fully validated, the obtained validation results show that the derived mathematical model and the corresponding parallelized computational model give a correct *in silico* representation of the studied process. The performed predictive simulations, including the case study, demonstrate the potential of the developed computational model and software to study the biodegradation behavior of implants. This can be further combined with other computational models to provide a multidisciplinary environment to investigate the mechanical integrity of implants or induced neotissue growth for different applications in orthopedics and tissue engineering.

3.6 Conclusions

The use of biodegradable metals for designing medical devices and implants has the challenge of controlling the release and rate of degradation, which is usually investigated by conducting *in vitro* and *in vivo* tests requiring conducting multiple experiments for different scenarios and situations. In this study, we have developed a mathematical model to predict the biodegradation behavior of commercially pure Mg-based biomaterials, which makes it possible to study the corrosion of implants and scaffolds in a simulated environment. Despite the assumed simplifications, the model can serve as an important tool to find the biodegradable metals properties and predict the biodegradation behavior of Mg-based implants that improves current design workflows.

Chapter 4

Extending the model: adding fluid flow and convection

This chapter is partially based on a manuscript prepared to be submitted:

M. Barzegari, C. Wang, S.V. Lamaka, G. Zavodszky, and L. Geris, “Interface-coupled multiphysics computational modeling of local pH changes during the biodegradation of magnesium biomaterials.”

Similar to the importance of perfusion in tissue engineering bioreactors, fluid flow plays an important role in biodegradation tests in hydrodynamics conditions. In this chapter, the development of a parallel fluid flow model is detailed, which is further coupled with the biodegradation model for simulating immersion tests in hydrodynamics setup.

4.1 Introduction

Considering fluid flow in the developed biodegradation model is crucial in light of the final application of the model, which is to be coupled with cell differentiation and tissue growth models to predict the rate of neotissue formation on biodegradable implants and scaffolds. In tissue engineering, cell expansion and differentiation experiments usually take place inside perfusion bioreactors, meaning that the flow of a biological fluid provides sufficient nutrients needed for the growth process and removes unnecessary and undesirable waste [101–103]. Moreover, the induced shear stress resulting from this perfusion plays a prominent role in the cell differentiation process [104–107], making the fluid flow inside the bioreactor even more critical. Consequently, the effect of the fluid flow should be considered in the biodegradation model

to enable it to make predictions in a perfusion setup, which is interchangeably called hydrodynamics conditions in chemistry.

Fluid flow in the context of a hydrodynamic condition has a similar application in corrosion and biodegradation experiments [108]. In a typical setup, the electrolyte moves and is refreshed over time to remove the corrosion products and provide needed mechanical stimuli if applicable. In biodegradation experiments, the flow velocity and induced shear stress affect the corrosion behavior of degradable scaffolds and implants due to increased mechanical forces and mass transfer [108]. Studies show that hydrodynamics conditions play a significant role in Mg degradation [109] where the corrosion rate increases in comparison to static conditions in immersion tests, in the presence of flowing [110], rotating [111], circulating [112], and *in vivo* perfusion [113]. Additionally, the fluid flow helps remove the corrosion products and avoid their accumulation [114].

The effect of hydrodynamics condition on the rate and pattern of biodegradation is rooted in the distribution and diffusion of fluids [115], which can be related to increment of mechanical stimuli like wall shear stress or increment in ions transport. It is reported that the presence of fluid flow leading to accelerated movement of the corrosive medium increases the rate of uniform and localized corrosion of Mg alloys [108]. The increase in corrosion rate is due to the increase of mass transfer of ions [115], affecting the chemical reactions occurring in the interface of Mg and the electrolyte [114,116]. Moreover, the increment in mass transfer removes more corrosion products from the surface, which is another contribution of the fluid flow to increasing the biodegradation rate [115]. Wang et al. [108] reported that the degradation rate was 0.37 ± 0.007 and $1.21 \pm 0.27\text{mm.year}^{-1}$ for the corrosion of stents made of Mg AZ31 alloys in static and hydrodynamics conditions, respectively. After considering the volume loss with CT measurements, they have concluded that the corrosion rate of these alloys is three times more in the presence of fluid flow, increasing from $\sim 0.6\text{mm.year}^{-1}$ in static condition to $\sim 1.5\text{mm.year}^{-1}$ in a hydrodynamics setup [108]. This shows the significance of adding fluid flow to the developed biodegradation model.

Computational Fluid Dynamics (CFD) is the field of studying the dynamics of fluid flow using mathematical and computational methods [117, 118]. The fluid flow is usually expressed in the form of Navier-Stokes or Stokes equations, on which appropriate numerical schemes are applied and the derived system of equations is solved using computers, resulting in the prediction of flow patterns and secondary entities like the shear stress. CFD modeling has been used in tissue engineering to study fluid flow systems such as dynamic cell culture conditions in perfusion bioreactors [119–121].

In this chapter, a parallel computational model for fluid flow simulations

was developed and coupled with the biodegradation model. The model was developed by solving the derived equations, i.e., Navier-Stokes equations coupled with the Darcy effect for the degrading object, using the finite element method. To ensure proper verification of the simulation results, the model output was compared with an OpenFOAM simulation on the same geometry and setup.

4.2 Methods

4.2.1 Navier-Stokes equations

In its general form, the Navier-Stokes equations describing the flow of an incompressible fluid with constant density ρ in the domain $\Omega \subset \mathbb{R}^d$ (with d being the dimension, so 2 or 3) can be written as [122]:

$$\begin{cases} \frac{\partial \mathbf{u}}{\partial t} - \nabla \cdot [\nu(\nabla \mathbf{u} + \nabla \mathbf{u}^T)] + (\mathbf{u} \cdot \nabla) \mathbf{u} + \nabla p = \mathbf{f}, & x \in \Omega, t > 0, \\ \nabla \cdot \mathbf{u} = 0, & x \in \Omega, t > 0, \end{cases} \quad (4.1)$$

in which \mathbf{u} is the fluid velocity, p is the pressure (which is actually pressure divided by the density), $\nu = \frac{\mu}{\rho}$ is the kinematic viscosity (with μ being the dynamic viscosity), and \mathbf{f} is a force term. The equations are conservation of linear momentum and conservation of mass (also called continuity equation), respectively. When ν is constant, the diffusion term in Eq. 4.1 can be simplified as [123]:

$$\text{div}[\nu(\nabla \mathbf{u} + \nabla \mathbf{u}^T)] = \nu(\Delta \mathbf{u} + \nabla \text{div} \mathbf{u}) = \nu \Delta \mathbf{u}, \quad (4.2)$$

which turns Eq. 4.1 into the following form:

$$\begin{cases} \frac{\partial \mathbf{u}}{\partial t} - \nu \Delta \mathbf{u} + (\mathbf{u} \cdot \nabla) \mathbf{u} + \nabla p = \mathbf{f}, & x \in \Omega, t > 0, \\ \nabla \cdot \mathbf{u} = 0, & x \in \Omega, t > 0, \end{cases} \quad (4.3)$$

Eq. 4.3 satisfies the incompressibility condition $\nabla \cdot \mathbf{u} = 0$ and needs proper initial and boundary conditions to be well-posed. The initial condition can be defined as:

$$\mathbf{u}(\mathbf{x}, 0) = \mathbf{u}_0(\mathbf{x}) \quad \forall \mathbf{x} \in \Omega, \quad (4.4)$$

where \mathbf{u}_0 is a divergence-free velocity field. Various types of boundary conditions can be applied, but the ones we deal with in this chapter are described here. If $\partial\Omega$ is the boundary of Ω , it can be split into 3 distinct boundaries $\partial\Omega = \Gamma_1 \cup \Gamma_2 \cup \Gamma_3$ each of which with a different type. On Γ_1 , the inlet

can be defined as a Dirichlet boundary condition for the velocity for a given velocity profile \mathbf{g} :

$$\mathbf{u} = \mathbf{g} \quad \text{on } \Gamma_1 \quad (4.5)$$

On Γ_2 , a wall boundary no-slip condition can be considered:

$$\mathbf{u} = 0 \quad \text{on } \Gamma_2 \quad (4.6)$$

On Γ_3 , for the outlet condition, a homogeneous Neumann condition on velocity and a zero pressure condition can be defined like:

$$\frac{\partial \mathbf{u}}{\partial \mathbf{n}} = 0, \quad p = 0, \quad \text{on } \Gamma_3 \quad (4.7)$$

with \mathbf{n} being the normal direction on the boundary $\partial\Omega$. Broadly speaking, these boundaries can be grouped into 2 sets: $\Gamma_D = \Gamma_1 \cup \Gamma_2$ and $\Gamma_N = \Gamma_3$ for boundaries with Dirichlet and Neumann conditions, respectively.

The Navier-Stokes equations can be written componentwise for individual components of the flow vector field in the Cartesian coordinates. Denoting $u_i, i = 1, \dots, d$ (with $d = 2$ in 2D and $d = 3$ in 3D), Eq. 4.3 can be presented as:

$$\begin{cases} \frac{\partial u_i}{\partial t} - \nu \Delta u_i + \sum_{j=1}^d u_j \frac{\partial u_i}{\partial x_j} + \frac{\partial p}{\partial x_i} = f_i, & i = 1, \dots, d, \\ \sum_{j=1}^d \frac{\partial u_j}{\partial x_j} = 0. \end{cases} \quad (4.8)$$

4.2.2 Weak formulation of the Navier-Stokes equations

For deriving the weak formulation, the first equation of 4.3 is multiplied by a test function \mathbf{v} defined on a proper function space V (with \mathbf{H}^1 being the Sobolev space defined in domain Ω) in which the test functions vanish on the Dirichlet boundary:

$$V = [\mathbf{H}_{\Gamma_D}^1(\Omega)]^d = \{\mathbf{V} \in [\mathbf{H}^1(\Omega)]^d : \mathbf{v}|_{\Gamma_D} = \mathbf{0}\}. \quad (4.9)$$

yielding to:

$$\int_{\Omega} \frac{\partial \mathbf{u}}{\partial t} \cdot \mathbf{v} d\omega - \int_{\Omega} \nu \Delta \mathbf{u} \cdot \mathbf{v} d\omega + \int_{\Omega} [(\mathbf{u} \cdot \nabla) \mathbf{u}] \cdot \mathbf{v} d\omega + \int_{\Omega} \nabla p \cdot \mathbf{v} d\omega = \int_{\Omega} \mathbf{f} \cdot \mathbf{v} d\omega. \quad (4.10)$$

Applying Green's divergence theory results in:

$$-\int_{\Omega} \nu \Delta \mathbf{u} \cdot \mathbf{v} d\omega = \int_{\Omega} \nu \nabla \mathbf{u} \cdot \nabla \mathbf{v} d\omega - \int_{\partial\Omega} \nu \frac{\partial \mathbf{u}}{\partial \mathbf{n}} \cdot \mathbf{v} d\gamma \quad (4.11)$$

and

$$\int_{\Omega} \nabla p \cdot \mathbf{v} d\omega = - \int_{\Omega} p \nabla \cdot \mathbf{v} d\omega + \int_{\partial\Omega} p \mathbf{v} \cdot \mathbf{n} d\gamma \quad (4.12)$$

Substituting Eqs. 4.11 and 4.12 into Eq. 4.10 yields to:

$$\begin{aligned} & \int_{\Omega} \frac{\partial \mathbf{u}}{\partial t} \cdot \mathbf{v} d\omega + \int_{\Omega} \nu \nabla \mathbf{u} \cdot \nabla \mathbf{v} d\omega + \int_{\Omega} [(\mathbf{u} \cdot \nabla) \mathbf{u}] \cdot \mathbf{v} d\omega - \int_{\Omega} p \nabla \cdot \mathbf{v} d\omega \\ &= \int_{\Omega} \mathbf{f} \cdot \mathbf{v} d\omega + \int_{\partial\Omega} \left(\nu \frac{\partial \mathbf{u}}{\partial \mathbf{n}} - p \mathbf{n} \right) \cdot \mathbf{v} d\gamma \quad \forall \mathbf{v} \in V. \end{aligned} \quad (4.13)$$

The last term of Eq. 4.13 is expressed in accordance to the defined Neumann boundary condition, which vanishes on Γ_3 due to the defined condition in the current study (Eq. 4.7). Moreover, this term vanishes on the Dirichlet boundaries due to the properties of the function space V (Eq. 4.9).

Similarly, the second equation of 4.3 is multiplied by a test function q belonging to the function space Q (with \mathbf{L}^2 being a Hilbert space defined in domain Ω), called the pressure space:

$$Q = \mathbf{L}_0^2(\Omega) = \{p \in \mathbf{L}^2(\Omega) : \int_{\Omega} p d\omega = 0\}, \quad (4.14)$$

resulting in:

$$\int_{\Omega} q \nabla \cdot \mathbf{u} d\omega = 0 \quad \forall q \in Q. \quad (4.15)$$

Eqs. 4.13 and 4.15 are so called weak forms of the Navier-Stokes equations.

4.2.3 Stokes equations

For viscous flow, where the Reynolds number is less than 1 ($Re = \frac{|\mathbf{U}|L}{\nu}$, with L and \mathbf{U} being the representative length and velocity of the domain), the convection term of the Navier-Stokes equations can be neglected, simplifying Eq. 4.3 to [123]:

$$\begin{cases} \alpha \mathbf{u} - \nu \Delta \mathbf{u} + \nabla p = \mathbf{f} & \text{in } \Omega, \\ \nabla \cdot \mathbf{u} = 0 & \text{in } \Omega, \end{cases} \quad (4.16)$$

with α being a positive coefficient. Eq. 4.16 can be used to model laminar flow in low Reynolds regimes and is simpler to handle than Eq. 4.3 from

the numerical computing perspective. The weak formulation of the Stokes equation can be derived by following the approach taken for the Navier-Stokes equations in Section 4.2.2. The final form of the weak formulation is:

$$\begin{cases} \int_{\Omega} (\alpha \mathbf{u} \cdot \mathbf{v} + \nu \nabla \mathbf{u} \cdot \nabla \mathbf{v}) d\omega - \int_{\Omega} p \nabla \cdot \mathbf{v} d\omega = \int_{\Omega} \mathbf{f} \cdot \mathbf{v} d\omega & \forall \mathbf{v} \in V, \\ \int_{\Omega} q \nabla \cdot \mathbf{u} d\omega = 0 & \forall q \in Q, \end{cases} \quad (4.17)$$

Eq. 4.17 can be written in the standard finite element variational form by defining 2 bilinear terms $a : V \times V \mapsto \mathbb{R}$ and $b : V \times Q \mapsto \mathbb{R}$:

$$\begin{aligned} a(\mathbf{u}, \mathbf{v}) &= \int_{\Omega} (\alpha \mathbf{u} \cdot \mathbf{v} + \nu \nabla \mathbf{u} \cdot \nabla \mathbf{v}) d\omega, \\ b(\mathbf{u}, q) &= - \int_{\Omega} q \nabla \cdot \mathbf{u} d\omega, \end{aligned} \quad (4.18)$$

which simplifies the notation of the variational problem of the Stokes equation to:

$$\begin{cases} a(\mathbf{u}, \mathbf{v}) + b(\mathbf{v}, p) = (\mathbf{f}, \mathbf{v}) & \forall \mathbf{v} \in V, \\ b(\mathbf{u}, q) = 0 & \forall q \in Q, \end{cases} \quad (4.19)$$

in which

$$(\mathbf{f}, \mathbf{v}) = \sum_{i=1}^d \int_{\Omega} f_i v_i d\omega. \quad (4.20)$$

4.2.4 Implementation

Numerical implementation of the Stokes (Eq. 4.16) and Navier-Stokes (Eq. 4.16) equations can be tricky due to the presence of specific sources of instability, which highly depends on the type of studied fluid regime [124, 125]. Various numerical models have been presented for dealing with these equations, some of which are commonly used in CFD applications, such as the Newton-Raphson approximation of Navier-Stokes equations and the Chorin's projection method.

In order to increase the stability and avoid problems in the mathematical analysis of the numerical models (e.g., V-ellipticity property), a pseudo-compressibility assumption can be added to the continuity equation. The pseudo-compressible approximation appears as a pressure term εp with ε being a very small coefficient, resulting in the following equation as the final

form of the Navier-Stokes equations that we consider in this study [126]:

$$\begin{cases} \frac{\partial \mathbf{u}}{\partial t} - \nu \Delta \mathbf{u} + (\mathbf{u} \cdot \nabla) \mathbf{u} + \nabla p = \mathbf{f}, \\ \nabla \cdot \mathbf{u} + \varepsilon p = 0. \end{cases} \quad (4.21)$$

Similarly, the Stokes equation can be written as:

$$\begin{cases} \alpha \mathbf{u} - \nu \Delta \mathbf{u} + \nabla p = \mathbf{f}, \\ \nabla \cdot \mathbf{u} + \varepsilon p = 0. \end{cases} \quad (4.22)$$

Another challenging part is to approximate the convection terms in the equations. One of the best approaches to do so is to take advantage of the method of characteristics, in which the characteristics curves of a PDE are used to convert it to an ODE, resulting in a simpler solution. By using the method of characteristics for the convection term and a backward Euler discretization for the temporal term, the weak form of the Navier-Stokes and continuity equations (Eq. 4.21) can be rewritten as:

$$\begin{aligned} & \int_{\Omega} \frac{\mathbf{u}^{n+1} - \mathbf{u}^n \circ X^n}{\Delta t} \cdot \mathbf{v} d\omega + \nu \int_{\Omega} \nabla \mathbf{u}^{n+1} \cdot \nabla \mathbf{v} d\omega - \int_{\Omega} p^{n+1} \nabla \cdot \mathbf{v} d\omega = \int_{\Omega} \mathbf{f} \cdot \mathbf{v} d\omega \\ & \int_{\Omega} \nabla \cdot \mathbf{u}^{n+1} q d\omega + \varepsilon \int_{\Omega} p^{n+1} q d\omega = 0 \end{aligned} \quad (4.23)$$

in which $(\mathbf{u}^{n+1}, p^{n+1})$ are the unknowns to be computed from the known state \mathbf{u}^n coming from the previous time step or the initial condition. In Eq. 4.23, the term $\mathbf{u}^{n+1} - \mathbf{u}^n \circ X^n$ is corresponding to the convection term being approximated using the method of characteristics.

The weak form of the Stokes equations stays almost the same as Eq. 4.17 (because it does not contain transient and convection terms) but needs a slight modification to add the pseudo-compressible terms from Eq. 4.22:

$$\begin{aligned} & \int_{\Omega} (\alpha \mathbf{u} \cdot \mathbf{v} + \nu \nabla \mathbf{u} \cdot \nabla \mathbf{v}) d\omega - \int_{\Omega} p \nabla \cdot \mathbf{v} d\omega = \int_{\Omega} \mathbf{f} \cdot \mathbf{v} d\omega, \\ & \int_{\Omega} q \nabla \cdot \mathbf{u} d\omega + \varepsilon \int_{\Omega} p q d\omega = 0. \end{aligned} \quad (4.24)$$

The model was implemented in the open-source PDE solver FreeFEM [86] using P1 elements for the pressure and P2 elements for the velocity state variables. Eqs. 4.23 and 4.24 can be easily implemented in FreeFEM thanks to the built-in support of the method of characteristics via the `convect` function.

4.2.5 Preconditioning and parallelizing the computation

The solution of the Stokes and Navier-Stokes equations using the finite element method in 3D is a computationally intensive process, and as a result, taking advantage of high-performance techniques to reduce the simulation time becomes crucial in real-world applications. Preconditioning the system and parallelizing the simulation by partitioning the mesh and distributing the partitions among available computing nodes in a parallel computing setup are great solutions to this challenge.

In the current implementation, the METIS graph partitioner [127] and HPDDM package [90] were used to partition the computational mesh and distribute the load over the available resources. For preconditioning and improving the solution time of the derived equations, various (combinations of) preconditioners and iterative or direct solvers available in the PETSc toolkit [89] were tested to find the most suitable combination.

While exact factorization preconditioners (such as LU) are easy to implement and use for fluid flow applications, they show bad memory scaling profiles in large-scale problems, meaning that memory usage increases exponentially with the problem size, making it almost impossible to use them for 3D cases. A better solution for this class of problems is to take advantage of the FieldSplit preconditioner in the PETSc toolkit, which allows solving the derived linear system of equations using the block matrices technique. In this technique, the matrices are divided into smaller blocks, and separate preconditioners or solvers can be assigned to each block (each field). These blocks arise naturally from the underlying physics or numerical discretization of the problem, such as velocity and pressure in fluid flow applications. For matrices with an arbitrary number of blocks, three different “block” algorithms are available in the PETSc toolkit: block Jacobi (**additive**), block Gauss-Seidel (**multiplicative**), and symmetric block Gauss-Seidel (**symmetric_multiplicative**), which can be selected by passing the desired one to the `pc_fieldsplit_type` flag. For two blocks, like the one in fluid flow problems with velocity and pressure as the blocks, another family of solvers based on Schur complements can be used.

In the current study, the FieldSplit preconditioner with Schur complement approximation was used on two blocks for velocity and pressure. A GMRES KSP type [88] was employed to solve the preconditioned system with an iterative solver. An Algebraic Multigrid (AMG) preconditioner [128] was used for the velocity block, and a Jacobi preconditioner was assigned to the pressure block. The result of this configuration, as well as the request for appropriate monitoring tools, can be written as follows:

```

-ksp_monitor -ksp_converged_reason -ksp_type fgmres
-pc_type fieldsplit -pc_fieldsplit_type schur
-pc_fieldsplit_schur_fact_type full
-fieldsplit_velocity_pc_type gamg
-fieldsplit_velocity_ksp_type preonly
-fieldsplit_pressure_pc_type jacobi
-fieldsplit_pressure_ksp_max_it 5

```

to pass to PETSc while solving the equations.

4.2.6 Considering the degrading object

In biodegradation simulations, a degrading object exists in the fluid domain, through which the flow should not pass because it is a solid part. One common approach to handle this situation is to remove the solid part from the fluid flow mesh, but since the part shrinks over time, this is not a feasible and efficient approach, needing tremendous mesh recreation and removal during simulation. As a result, in the current study, the presence of the solid body as a barrier is taken into account by adding a Darcy term for the permeability to the Navier-Stokes and Stokes equations. A penalization technique is then employed to implement it in the weak formulation. To couple the fluid flow model with the biodegradation model, a convection term is added to the ions transport equations, causing the fluid velocity field advect the ions.

Adding the Darcy term to Eq. 4.16 and considering no other acting force yields to:

$$-\nu\Delta\mathbf{u} + \nabla p + \frac{\nu}{K}\mathbf{u} = 0, \quad (4.25)$$

where K is the permeability function. Similar to Eq. 4.25 the effect of the solid part can be added to the Navier-Stokes equation (Eq. 4.3) by the Darcy term, leading to the following equation:

$$\frac{\partial\mathbf{u}}{\partial t} - \nu\Delta\mathbf{u} + (\mathbf{u} \cdot \nabla)\mathbf{u} + \nabla p + \frac{\nu}{K}\mathbf{u} = 0. \quad (4.26)$$

The Darcy term vanishes in regions with high permeability, i.e., inside the fluid domain, resembling the Stokes equation. Still, when K is very small, i.e., inside the solid part, it dominates the flow and acts like a barrier. To avoid numerical perturbation for switching between these 2 regions, a Heaviside function is defined to update K [129]:

$$H(\phi) = \begin{cases} 0, & \phi < -\varepsilon \\ \frac{1}{2} + \frac{\phi}{2\varepsilon} + \frac{1}{2\pi} \sin\left(\frac{\pi\phi}{\varepsilon}\right), & -\varepsilon < \phi < \varepsilon \\ 1, & \phi > \varepsilon \end{cases} \quad (4.27)$$

in which ϕ is the level-set signed distance function used to separate the solid and solution parts (Eqs. 3.3 and 3.4), and ε is set to $1.5h$, with h being the minimum mesh element size. Then, K can be accordingly updated to have a smooth transition between regions with a big difference in permeability:

$$K(\mathbf{x}) = 10^{30}(1 - H) + K_0H \quad (4.28)$$

where K_0 is the permeability of metals in fluid regions ($\sim 10^{-6}$ H/m).

4.2.7 Simulation setup

Test case to compare with OpenFOAM

In order to perform a verification analysis on the developed CFD model, a case of 3D flow inside a chamber was implemented to compare the simulation results with those of a well-established and known CFD solver. For this reason, the OpenFOAM open-source solver was used, which has been extensively used for fluid dynamics simulations over the last decades [130]. The simulation was carried out using the simpleFOAM solver, which uses the SIMPLE (Semi-Implicit Method for Pressure Linked Equations) algorithm for coupling and solving the Navier-Stokes equations.

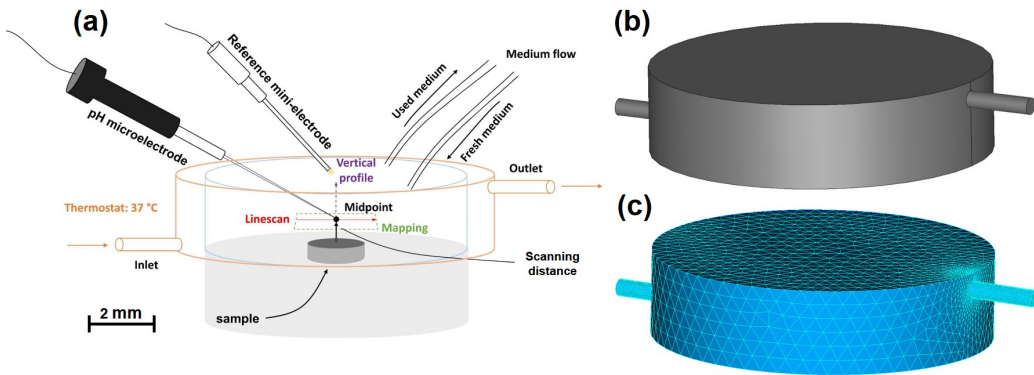


Figure 4.1: Fluid flow model construction for comparing the CFD results with the experimental setup: a) a schematic of the experimental setup, b) the CAD geometry, c) the generated mesh containing tetrahedral elements.

The geometry was chosen based on the experiments performed for biodegradation in hydrodynamics conditions. The experimental setup is depicted in Fig. 4.1-A, where the constructed CAD geometry is shown in Fig. 4.1-B. The computational mesh, comprising linear tetrahedral elements, was generated

using Netgen [91] in the SALOME platform [92]. The final mesh used in both FreeFEM and OpenFOAM models is shown in Fig. 4.1-C, containing 100,888 elements.

The fluid flow direction is from left to right, meaning that the inlet was set on the vertical face of the small pipe on the bottom left side of the chamber, and the outlet was set similarly on the upper right pipe. The rest of the boundaries were set to no-slip boundary conditions. A zero pressure boundary condition was set on the outlet. The inlet velocity was set to 1.0mm/s, and the parameter ν was set to 0.85mm²/s.

Test case to check coupling with degradation model

In addition to the test case for verification of the developed CFD code, two more cases were constructed to evaluate the model's performance in the presence of a barrier, i.e., the degrading object in the coupled biodegradation model. To this end, after coupling the models, a simple 3D geometry of a cylinder with an embedded sphere as the degrading object inside was simulated. The simulation parameters were set similarly to the verification case. The inlet and outlet were assigned to the bases of the cylinder, and the altitude was assigned as the wall boundary condition. Fig. 4.2 shows a schematic of the computational setup for this test case as well as a vertical cut of the generated computational mesh containing 640,249 elements. The mesh was refined on the interface of the degrading object to increase the numerical accuracy of the biodegradation model.

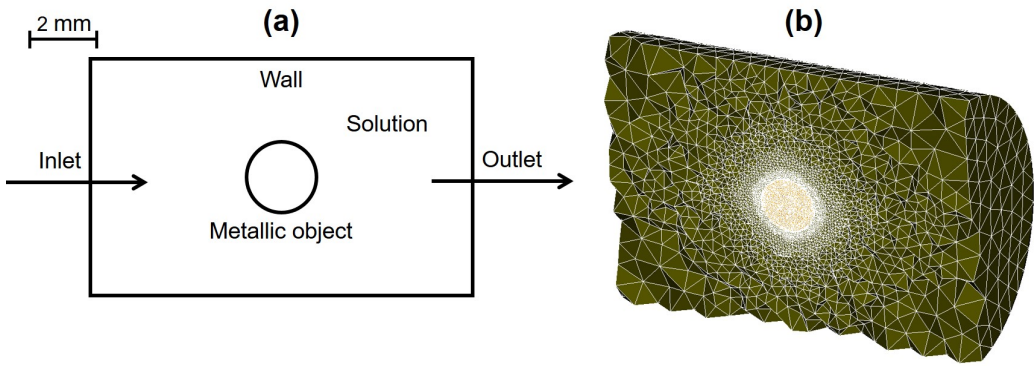


Figure 4.2: Model construction for checking the coupling of the fluid flow and biodegradation models: a) schematic representation of the domain b) the generated computational mesh.

Additionally, a simple 2D representation of the full chamber model (Fig.

4.1) was constructed to test the effect of the fluid flow on the degradation behavior of the metallic parts. In this model, a high inlet velocity and a high diffusion coefficient were used to have an exaggerated degradation, showing how the fluid flow would affect the change of morphology of the object. The degrading metallic part was selected to be a small rectangle on the bottom of the chamber. The domain setup is depicted schematically in Fig. 4.3. The computational mesh was generated using the SALOME platform and contained 24,946 elements.

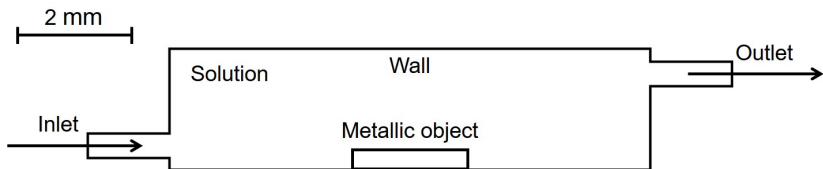


Figure 4.3: Schematic view of the model used for checking the effect of the fluid flow on biodegradation behavior.

4.3 Results

To verify the robustness of the model predictions, the results of the CFD code developed in FreeFEM were compared both quantitatively and qualitatively with an OpenFOAM model of an identical set-up. The qualitative comparison was made via the streamlines, showing how the flow develops by plotting the trajectory lines of the fluid velocity field inside the desired domain, which is the chamber in this case. Figs. 4.4 and 4.5 show such comparison between the developed model and OpenFOAM. Fig. 4.4 shows the streamlines for both models from a side view, in which the flow enters the chamber from the left inlet pipe and leaves it from the top right outlet. The qualitative comparison shows a good agreement between the predictions of the models.

Similarly, Fig. 4.5 depicts a comparison but from the top view, showing good agreement between the predictions, although the OpenFOAM model (bottom) shows slightly better performance on the boundaries as can be appreciated from the existence of extra streamlines close to the cylinder boundary in the FreeFEM code results.

Moreover, a quantitative comparison is possible by comparing the numerical values predicted by the models in various regions of the desired domain, including the regions close to the boundaries. Fig. 4.6 shows the comparison

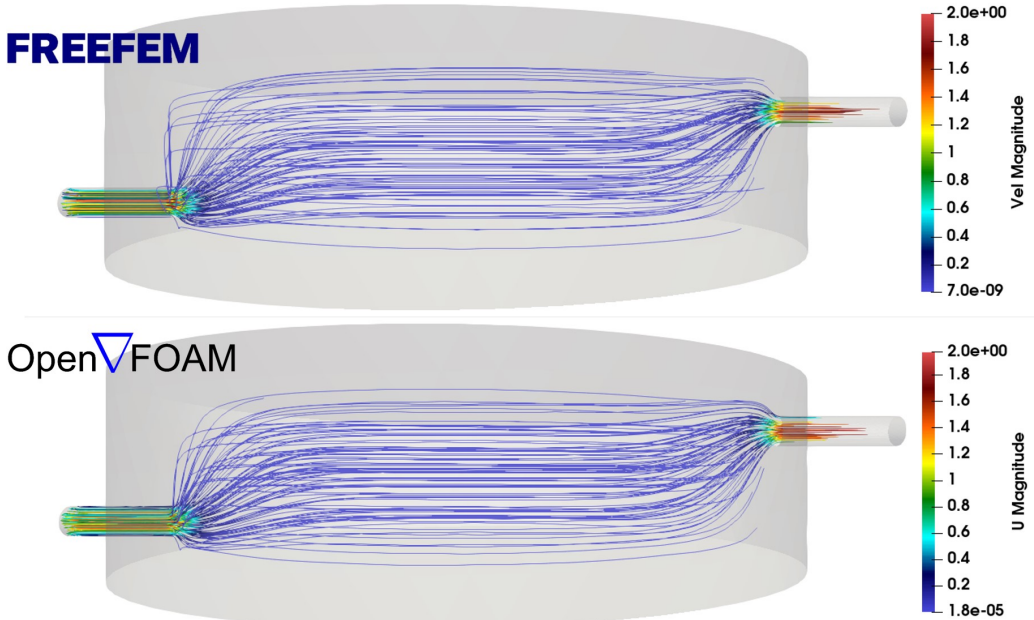


Figure 4.4: Comparing the results of the developed CFD model (top) with OpenFOAM (bottom) via plotting the streamlines of the fluid velocity field, depicted from the side view. The colors on the trajectory lines show the magnitude of the velocity vector (in mm/s).

of the fluid velocity field visualization between the developed CFD code and OpenFOAM on a cross-section in the center of the chamber, showing that both models produce the same results quantitatively.

A closer look at the center of Fig. 4.6 is depicted in Fig. 4.7, where the color bar range is adapted to contain only the visible values. This zoomed-in comparison confirms the good agreement between the CFD model and OpenFOAM results. The employed mesh is relatively coarse in the center (regions far from the inlet and outlet), the effect of which can be seen as non-smooth velocity profiles in Fig. 4.7. Still, both models handle this coarse mesh effect similarly.

Fig. 4.8 shows the result of a proof-of-concept simulation in which the biodegradation model [131] (presented in Chapter 3) is coupled with the fluid flow model. This was done by solving Eq. 4.26 (or Eq. 4.25 for simpler cases) and adding a convection term to the equations of the biodegradation model to include the directional effect of fluid flow on the degrading object. The interplay between the fluid flow and the degradation can be seen in Fig. 4.8 with the released ions being advected to the right (the direction of the fluid

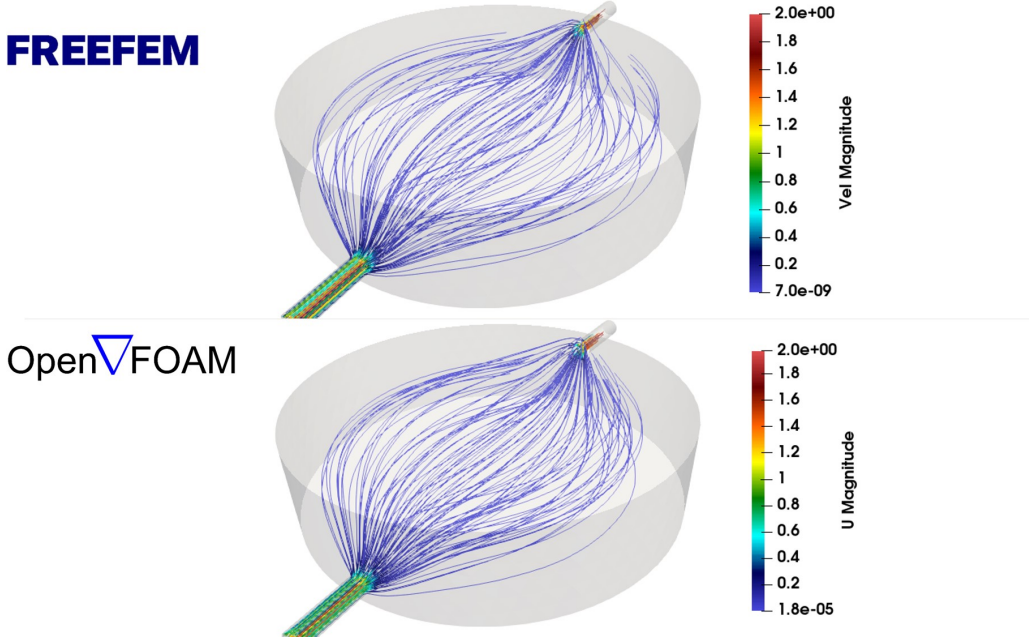


Figure 4.5: Streamlines of the fluid velocity field plotted from a top view to compare the output of the developed CFD model (top) and OpenFOAM (bottom) with colors showing the magnitude of the velocity vector at each point (in mm/s).

flow) and the degrading object being slightly more degraded on the left.

Fig. 4.9 shows the effect of the degrading object on the fluid velocity field, depicted as streamlines passing over the solid part at the end of the performed simulation. The figure demonstrates the fluid flow response to the presence of the changing morphology of the obstacle, obtained from solving the Navier-Stokes equations containing the Darcy term (Eq. 4.26).

Fig. 4.10 shows the results of the second test case for the coupled biodegradation model, in which the release of metallic ions is depicted over time along with the change of the morphology of the degrading object. The released metallic ions get convected in the direction of the flow field inside the chamber, which was obtained by solving the Navier-Stokes equations.

4.4 Discussion

In this study, a parallel fluid flow model was developed to be coupled with the computational biodegradation model enabling the consideration of the effect of the hydrodynamics conditions in corrosion tests. The most important

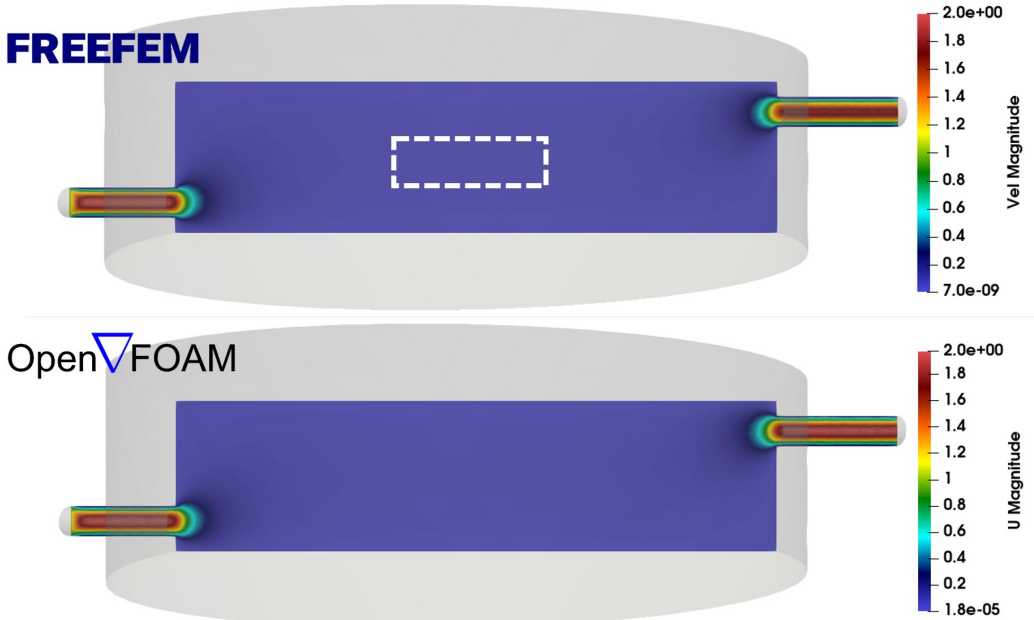


Figure 4.6: comparison between the fluid velocity field predicted by the developed CFD code (top) and OpenFOAM (bottom), depicted on a vertical cross-section in the center of the chamber. Fluid enters the chamber from the left and leaves it from the right. The colors show the magnitude of the velocity vector at each point (in mm/s). The white dashed-line box shows the zoomed-in area of Fig. 4.7.

form of hydrodynamics in tissue engineering is the perfusion phenomenon in bioreactors, which makes the development of such coupled degradation-CFD model even more crucial considering the final application of the biodegradation model. Similar to perfusion bioreactors, the hydrodynamics set-up in biodegradation tests helps removing corrosion products and providing mechanical forces if applicable.

In order to verify the developed CFD model, a test case was prepared to simulate a similar chamber flow model in both the in-house FreeFEM code and the OpenFOAM code, a well-established open-source CFD solver. Qualitative (Figs. 4.4 and 4.5) and quantitative (Figs. 4.6 and 4.7) comparison of results show identical predictions for the flow field in both models, demonstrating that the derivation of the weak forms of Navier-Stokes equations as well as their numerical implementation in FreeFEM were performed correctly. This comparison indicates that the developed code can be used instead of a well-known and sophisticated CFD solver for the desired flow

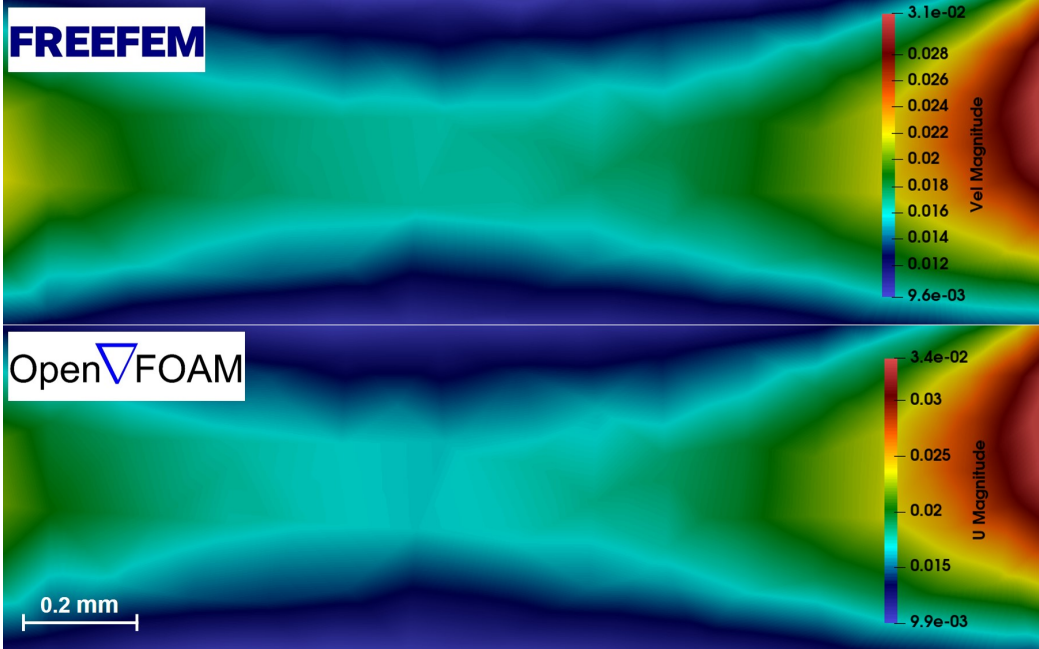


Figure 4.7: A zoomed-in view of the area depicted as white dashed-line in Fig. 4.6, indicating the fluid velocity field for results predicted by the developed CFD code (top) and OpenFOAM (bottom) with colors showing the magnitude of the velocity vector at each point (in mm/s).

regime, which is laminar flow with low Reynolds numbers.

The reason for developing an in-house CFD code instead of using a well-established CFD solver lies in the lack of availability of proper coupling software. Although various efficient solver coupling codes exist and are widely used in similar scenarios (such as the preCISE coupling library [132]), at the time of this writing and to the best of the authors' knowledge, there is no compatible coupling software for FreeFEM, the language in which the computational model of the biodegradation process was implemented. In case of existence, the computational biodegradation model could have been linked with OpenFOAM, SU2, or Code_Saturne in an efficient in-memory way. But, with such an approach not available, the only feasible approach would be coupling the models using disk IO (input-output), meaning that in each time step, the computational model should write the domain data on disk (we should notice that the domain evolves since it is a moving interface problem), and the CFD code reads the data, computes the flow field, and writes it back to the disk so that the biodegradation would read it back. Despite the possibility of employing this approach, the computationally in-

tensive aspects of the models, which is the result of a 3D mesh refined on the corrosion interface leading to normally 2M-4M elements, makes the workflow dramatically inefficient. Working in HPC environments and dealing with a partitioned mesh can make the situation even more complex. This reasoning made it inevitable to develop an in-house CFD code so that it can be seamlessly and efficiently coupled with other models.

In order to couple the flow model with the computational biodegradation model, both models should be modified to include the effect of the other one. For the biodegradation model, the effect of fluid flow was considered as an extra convection term in the set of derived reaction-diffusion equations, which can be implemented using the method of characteristics in FreeFEM. On the other side, the inclusion of the effect of a degrading object can be more tricky in the CFD model. This was done by adding a Darcy term to the Navier-Stokes and Stokes equation, which considers a high permeability for the regions inside the degrading object, preventing fluid from penetrating into those parts. After the degrading part interface shrinks, the Darcy term gets updated automatically since it is formulated based on the level-set function used in the biodegradation model to describe the moving corrosion interface. Figs. 4.8 and 4.9 demonstrate the effect of the presence of the degrading part on the pattern of flow, while Fig. 4.10 shows the effect of fluid flow on the biodegradation, which is the ions being convected in the direction of the fluid velocity field, leading to a minor directional degradation in which the side facing the flow direction degrades slightly faster.

The performed verification study on the developed CFD code is not enough to call it a fully validated fluid flow model. However, by considering the desired flow regime in biodegradation tests, the verification shows that the coupled model is capable of predicting acceptable and correct results. Nonetheless, dedicated validation tests can be further done to fully validate the developed model as a general CFD code which can be used standalone for simulating laminar flows with low Reynolds numbers.

4.5 Conclusion

In this chapter, a parallel fluid flow model was developed and linked with the biodegradation model, making it possible to simulate the degradation process in hydrodynamics conditions. Proper preconditioners and solvers were selected to improve the parallel efficiency of the developed model in HPC environments. The results obtained from the fluid flow model were compared with the output of a similar simulation performed using OpenFOAM, in which a good agreement was observed, verifying the performance

of the developed model for the desired flow regime needed to perform local pH simulations in Chapter 5.

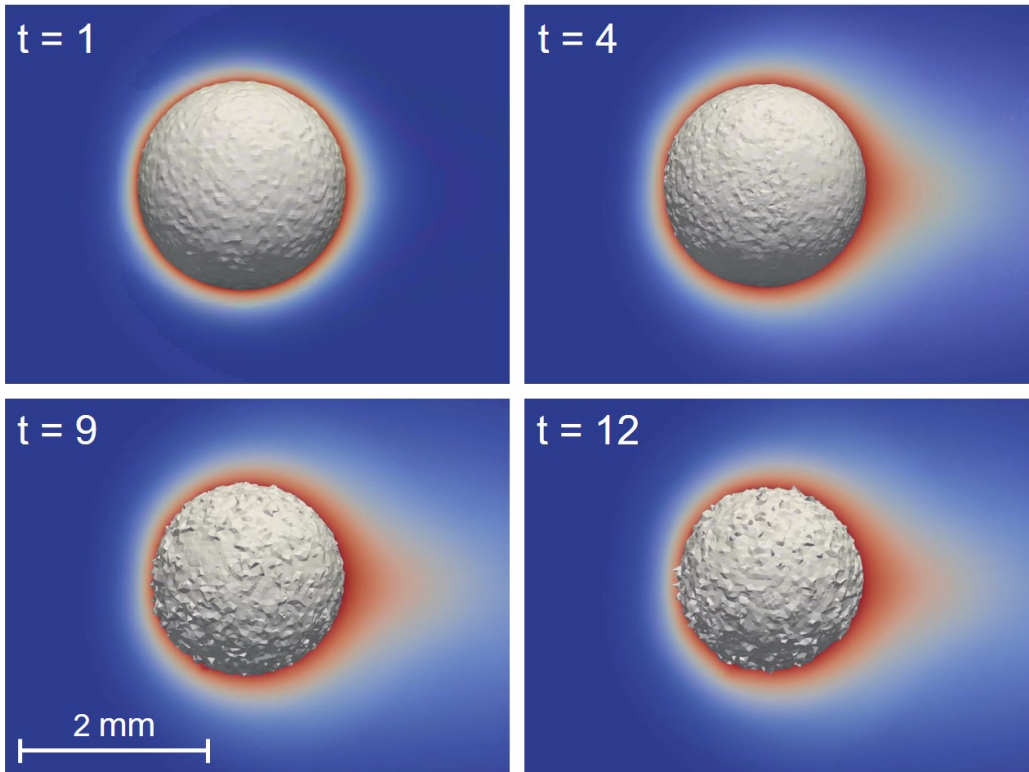


Figure 4.8: Biodegradation simulation results in the presence of fluid flow over time, showing the interplay between the fluid flow and biodegradation models. The displayed time is in an arbitrary unit for demonstrating the intervals only. The flow gets detoured due to the presence of an obstacle, and the released ions get advected to the direction of fluid flow (left to right). The colors represent the concentration of Mg ions as they get released to the surrounding environment and subsequently get diffused/advectioned. The gray surface shows the zero iso-contour of the used level-set function to track the degrading object's interface, demonstrating the solid part's change of morphology.

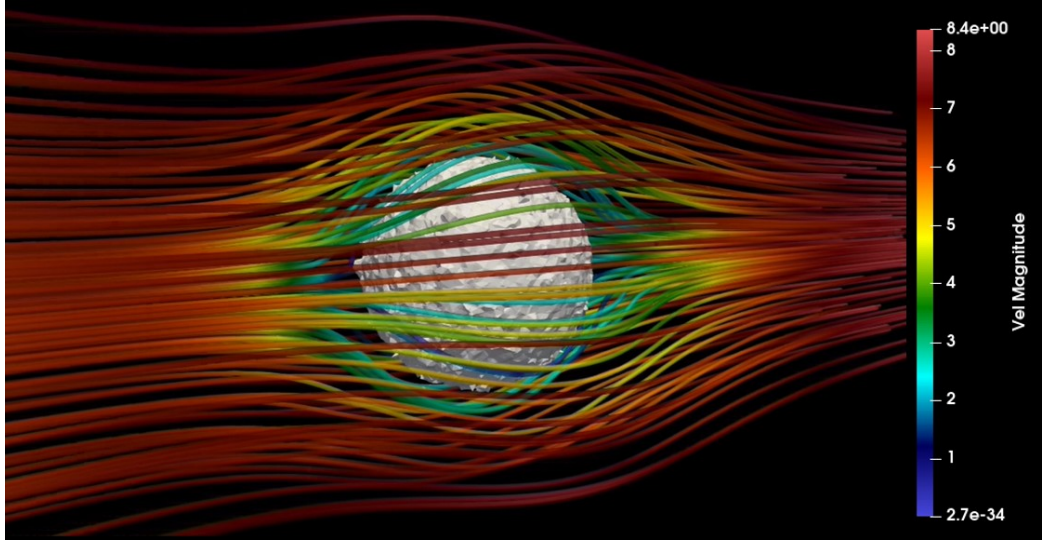


Figure 4.9: Visualization of the fluid velocity field depicted by streamlines passing over a degrading object. Colors show the magnitude of the velocity field (in mm/s) projected on the streamlines.

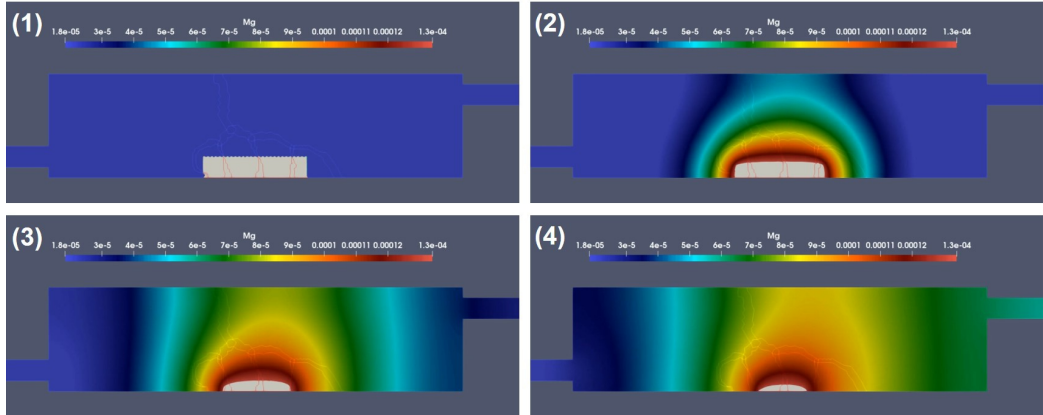


Figure 4.10: Visualization of the results of the biodegradation of an object inside the chamber in hydrodynamics conditions. Colors show the concentration of released metal ions getting convected in the direction of fluid flow. The light gray part shows the degrading object. The numbers (1) to (4) demonstrate the evolution of the simulation over time.

Chapter 5

Extending the model: simulating local pH evolution

This chapter is based on a manuscript prepared to be submitted:
M. Barzegari, C. Wang, S.V. Lamaka, G. Zavodszky, and L. Geris,
“Interface-coupled multiphysics computational modeling of local pH
changes during the biodegradation of magnesium biomaterials.”

In this chapter, the basic biodegradation model developed in Chapter 3 is further developed to capture more advanced chemistry occurring at the corrosion interface in HBSS solutions, making it possible to simulate more complex environments and local pH changes during the biodegradation process.

5.1 Introduction

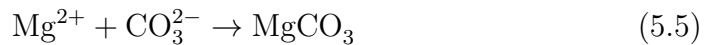
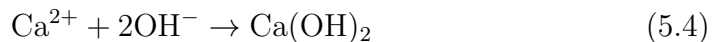
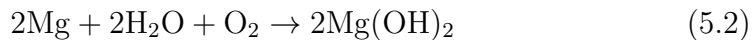
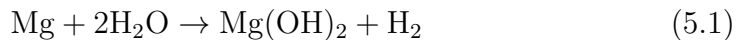
Mg is the most studied biodegradable metal [2,3,71,133], on which many research groups have performed valuable biodegradation studies [11,134–136]. The biodegradation behavior of Mg is investigated in *in vitro* corrosion tests, in which the selection of the corrosive media plays an important role since it affects the underlying chemical reactions [35]. By considering the main application of the biomaterial, which can be tissue engineering scaffolds, vascular stents, or orthopedic fixation implants, the corrosive media can be selected to be a representative of the service environment. The most basic form of the medium is a saline (NaCl) solution, in which the degradation rate is the highest possible [35]. More complex solutions can be used to mimic the behavior of the body environment by taking into account additional body fluid com-

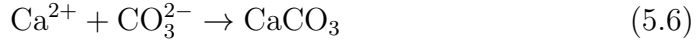
ponents, the most popular of which are Ringer's solution, PBS (phosphate buffered saline), SBFs (simulated body fluids), HBSS (Hank's balanced salt solution), and Earle's balanced salt solution (EBSS) [35]. Adding more organic components to the solution will make it ready to simulate cell culture conditions. The common media for this purpose are MEM (Minimum Essential medium) and DMEM (Dulbecco's modified Eagle's medium) [35].

Various studies have already investigated the effect of different components in the aforementioned corrosive media on the degradation behavior of Mg materials [36–40]. A typical composition of "simulated body fluid" solutions (such as SBF, HBSS, and EBSS) is chloride, carbonate, phosphates, sulfate, and calcium. The individual effect of these components on the rate of degradation of Mg has been extensively studied, in which it has been observed that carbonate and phosphate slow down the rate while the effect of sulfate is negligible [38, 40]. The concentration of HCO_3^- affects the pH buffering capacity and the degradation rate of Mg simultaneously [47].

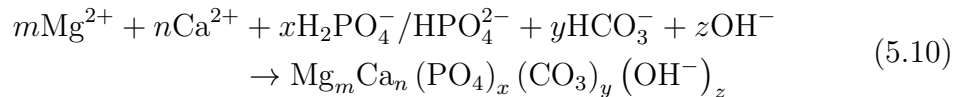
The effect of calcium ions is more complex because it has been found that Ca^{2+} doesn't contribute to the Mg corrosion directly [7], but a mixed effect of Ca^{2+} , Mg^{2+} , HCO_3^- , and $\text{H}_2\text{PO}_4^-/\text{HPO}_4^{2-}$ forms a co-precipitation layer on the corroded surface of Mg, slowing down the corrosion rate of commercially pure Mg as well as of some Mg alloys [36, 39]. It has also been reported that although various Mg alloys show different intrinsic degradation behavior in NaCl solution, they possibly behave similarly in simulated body fluids [40, 137]. Since the humoral regulations inside the human body control the changes in pH of body fluids, it is common to use pH buffers to mimic a similar condition, but it should be taken into account that buffering solutions may affect the degradation rate of Mg [138, 139] and may also delay the formation of the precipitate layer [39]. An alternative solution to address this issue is to use natural pH buffers such as $\text{HCO}_3^-/\text{CO}_2$, an option that is commonly used for immersion tests under cell culture conditions. In this situation, an equilibrium between H_2CO_3 (CO_2), HCO_3^- , and CO_3^{2-} keeps the pH constant. As a result, using simulated body fluids for corrosion tests without additional synthetic pH buffers is still acceptable [39, 40].

The major reactions occurring in simulated body fluids can be written as:





The protection layer is formed on the corroded surface as a hydroxyapatite-like precipitation according to the following reaction [44, 82, 140, 141]:



In fact, the similarity in corrosion behavior of various Mg alloys in SBF solutions is due to the similar composition of this quasi-protective layer, a mechanism that doesn't occur in NaCl solution, leading to a more apparent difference in degradation rate between Mg alloys. The composition of the formed hydroxyapatite-like precipitation layer is close to the ones found *in vivo* [35]. Additionally, local pH measurements in HBSS and SBF show that, in contrast to saline solutions, the local pH value is not alkaline [39, 142]. This has been reported for hydrodynamics situations, under which the medium composition is kept constant by replacing the consumed ions by means of fluid flow.

Building mathematical and computational models of the biodegradation process in complex buffered solutions can help save the resources required to perform *in vitro* tests, but the details of the aforementioned chemistry are challenging to capture in a mechanistic model. Few attempts have been made to model the underlying chemical reactions in SBF solutions [100, 143, 144], but due to the complexity of the resulting mathematical models, it is not feasible to extend them to 3D and real-world cases, like for simulation of the degradation of biomedical implants. In the case of data-driven approaches [145], the applicability is limited to the studied conditions, making it difficult for developed models to achieve high extensibility and generalizability.

In this chapter, a detailed mathematical model is presented to extend the work discussed in Chapter 3 and [131], in which a mechanistic model of the biodegradation process is coupled with a thermodynamics-based code to predict local interfacial biodegradation of Mg in HBSS solutions. The local pH changes are the validation criterion to compare the simulation results with experimental ones. Besides other parameters affecting the Mg biodegradation mechanism, monitoring the pH changes at the degradation interface has proved to be significant due to its direct effect on the formation and stability of the degradation products layer [146].

Table 5.1: The elemental composition of ultra-high pure and commercial pure Mg used for performing corrosion experiments (percentages)

	Fe	Si	Mn	Al	Cu	Ni
CP-Mg	0.03420	0.0001	0.00237	0.00402	0.00037	<0.0002
UHP-Mg	0.0012	<0.0001	0.00037	0.00291	<0.0001	<0.0002

5.2 Methods

5.2.1 Experimental setup

In this study, the corrosion tests were performed on ultra-high pure (UHP) and commercially pure (CP) Mg in hydrodynamics conditions. The elemental composition of the used materials is shown in Table 5.1, measured by Atomic Absorption Spectrometer (AAS). The samples were prepared as rod shapes with a diameter of 2mm mounted in epoxy resin with a disc shape. The electrolyte used for corrosion tests was commercial HBSS (ThermoFisher Scientific, no. 14025100), the composition of which is presented in Table 5.2.

Table 5.2: Chemical composition of the HBSS electrolytes used to perform corrosion tests for local pH measurements.

Components	mM
KCl	5.33
KH ₂ PO ₄	0.44
NaHCO ₃	4.17
NaCl	137.9
Na ₂ HPO ₄	0.34
CaCl ₂	1.26
MgCl ₂ · 6H ₂ O	0.49
MgSO ₄ · 7H ₂ O	0.41
D – Glucose	5.56

Local pH measurements were performed using a glass-type pH microelectrode with a tip diameter of 10 μm (Unisense, pH-10). The electrode was positioned above the sample at a distance of $50 \pm 3\mu\text{m}$. At this distance, a line scan mapping routine was performed to obtain the horizontal pH profiles, in which a specimen-centered area ($3000 \times 3000\mu\text{m}$, which was used as the simulation domain as well) was mapped with the step length of 100 μm . The sampling interval was 3 s, the result of which was a total duration of approximately 1 hour to scan the area. Similarly, the vertical pH profiles were

scanned starting at the height of $50\mu\text{m}$ above the midpoint of the specimen up to $500\mu\text{m}$ in the bulk medium. Fig. 5.1 demonstrates the setup of the experiment schematically, in which the flow enters the chamber from the left with a rate of $1.0\text{mL}\cdot\text{min}^{-1}$ (Medorex TL15E peristaltic pump) and leaves it to the right. The tests were performed independently at room temperature (RT, 22 ± 2 in an air-conditioned lab) and 37°C (Thermo Scientific SAHARA S13).

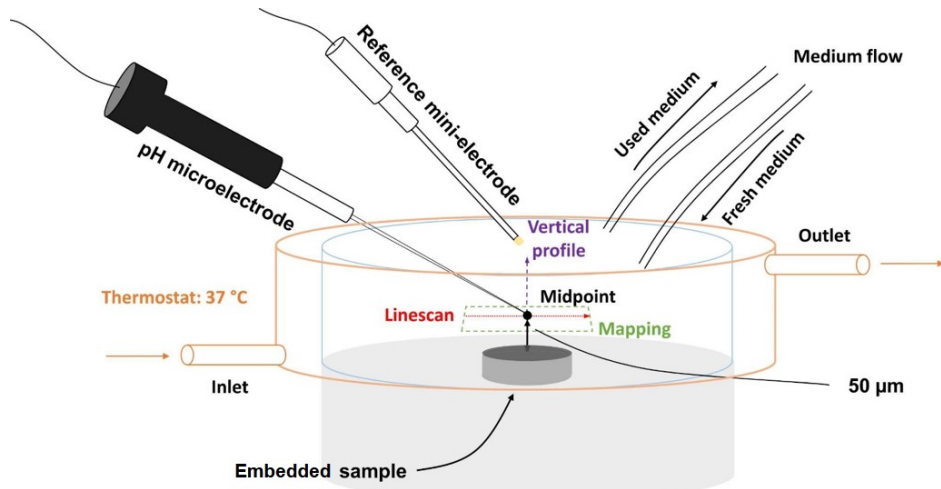


Figure 5.1: Experimental setup for validating the coupled biodegradation model

The *in vitro* cross-section morphology of the specimens was characterized using a dual beam FIB/SEM platform (LYRA3 TESCAN) equipped with an EDX system (Oxford Inca with a silicon drift detector), the result of which was used to compare qualitatively with the simulation predictions.

5.2.2 Computational model construction

The computational model in the current study comprises three coupled modules:

1. An extended version of the mechanistic biodegradation model based on our previous work [131] (Chapter 3) to obtain Mg and hydroxide ions distributions and the initial formation of the protective layer based on the modeling hypotheses.
2. A thermodynamics-based simulation to estimate the concentration of various components of the electrolyte in regions close to the surface of the sample based on the calculated pH of module 1.

3. A module to link the former two, calculating the hydroxyapatite-like precipitation concentration, in which calculated pH values were transferred from module 1 to module 2 for each node of the computational mesh to calculate the concentration of ions depending on the computed local pH and transfer back the calculated precipitation concentration to module 1.

Fig. 5.2 shows a schematic representation of the coupled modules and the way that simulation data are being transferred between them. It should be noted that the results obtained from module 2 are calculated in an equilibrium state as it is a thermodynamics-based code, but module 1 works based on kinetics equations and calculations. As a result, it is assumed that the kinetics of the reactions is affected by the equilibrium state of involved chemical components in each time step, which can be considered as a small time window in which the chemical species are in equilibrium. This fact should be seen as an assumption made for simplifying the calculation of the stoichiometry of the protective layer (Eq. 5.10), in which the effect of the underlying kinetics on the change of pH is neglected.

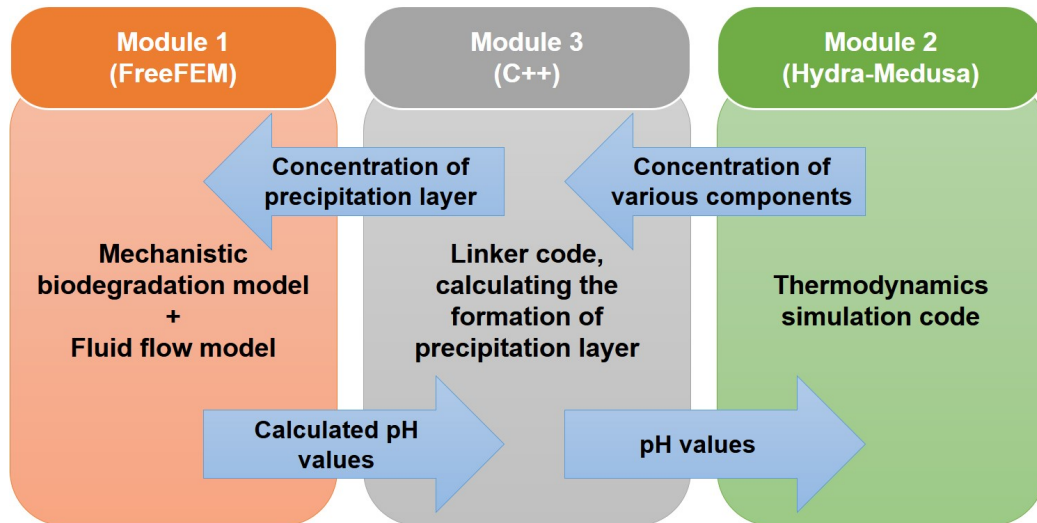
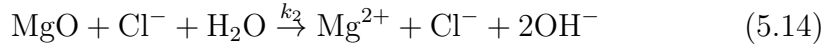
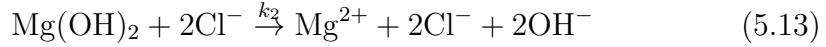
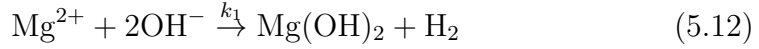
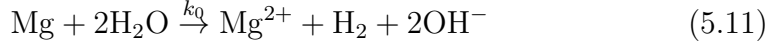


Figure 5.2: Schematic representation of the coupled modules for modeling of local pH changes, showing how they are connected as well as the programming languages and tools used for the implementation.

The computational biodegradation model (module 1) was developed by deriving a set of reaction-diffusion-advection equations from the chemistry of the corrosion of Mg in hydrodynamics conditions. The following basic reactions are captured by this model, which is an extension of our previous

contribution [131] (Chapter 3) as the overall process is described in more detailed equations:



The following state variables hold the concentration of various basic ions involved in reactions described by Eqs. 5.11, 5.12, 5.13, and 5.14:

$$\begin{aligned} C_{\text{Mg}} &= C_{\text{Mg}}(\mathbf{x}, t), & C_{\text{Mg}_{[\text{s}]}} &= C_{\text{Mg}_{[\text{s}]}}(\mathbf{x}, t), & C_{\text{Mg}(\text{OH})_2} &= C_{\text{Mg}(\text{OH})_2}(\mathbf{x}, t) \\ C_{\text{Cl}} &= C_{\text{Cl}}(\mathbf{x}, t), & C_{\text{OH}} &= C_{\text{OH}}(\mathbf{x}, t) & \mathbf{x} \in \Omega \subset \mathbb{R}^3 \end{aligned}, \quad (5.15)$$

Additionally, two more state variables are needed to couple the models, representing the calculated concentration of the hydroxyapatite-like precipitation as well as the cumulative layer concentration:

$$C_{\text{Hydrox}} = C_{\text{Hydrox}}(\mathbf{x}, t), \quad C_{\text{Film}} = C_{\text{Film}}(\mathbf{x}, t) \quad \mathbf{x} \in \Omega \subset \mathbb{R}^3, \quad (5.16)$$

where the total film concentration can be calculated as:

$$C_{\text{Film}} = C_{\text{Hydrox}} + C_{\text{Mg}(\text{OH})_2}. \quad (5.17)$$

With the above state variables defined, the biodegradation model can be constructed by implementing the following PDEs:

$$\frac{\partial C_{\text{Mg}_{[\text{s}]}}}{\partial t} = -k_0 C_{\text{Mg}_{[\text{s}]}} \quad (5.18)$$

$$\frac{\partial C_{\text{Mg}}}{\partial t} = \nabla \cdot (D_{\text{Mg}}^e \nabla C_{\text{Mg}}) - \nabla \cdot (\mathbf{u} C_{\text{Mg}}) + k_0 C_{\text{Mg}_{[\text{s}]}} - k_1 \alpha C_{\text{Mg}} C_{\text{OH}}^2 + k_2 C_{\text{Film}} C_{\text{Cl}}^2 \quad (5.19)$$

$$\frac{\partial C_{\text{Mg}(\text{OH})_2}}{\partial t} = k_1 \alpha C_{\text{Mg}} C_{\text{OH}}^2 - k_2 C_{\text{Film}} C_{\text{Cl}}^2 \quad (5.20)$$

$$\frac{\partial C_{\text{Cl}}}{\partial t} = \nabla \cdot (D_{\text{Cl}}^e \nabla C_{\text{Cl}}) - \nabla \cdot (\mathbf{u} C_{\text{Cl}}) \quad (5.21)$$

$$\frac{\partial C_{\text{OH}}}{\partial t} = \nabla \cdot (D_{\text{OH}}^e \nabla C_{\text{OH}}) - \nabla \cdot (\mathbf{u} C_{\text{OH}}) + k_0 C_{\text{Mg}_{[\text{s}]}} - k_1 \alpha C_{\text{Mg}} C_{\text{OH}}^2 + k_2 C_{\text{Film}} C_{\text{Cl}}^2 \quad (5.22)$$

showing the mathematical representation of reactions 5.11, 5.12, 5.13, and 5.14 in hydrodynamics condition in the form of a set of reaction-diffusion-advection equations. k_0 , k_1 , and k_2 are reaction rate constants corresponding to the Mg oxidation, film formation, and film elimination reactions, respectively. In Eqs. 5.19, 5.20, and 5.22, α is defined as:

$$\alpha = \left(1 - \beta \frac{C_{\text{Film}}}{[\text{Film}]_{\max}}\right), \quad (5.23)$$

in which the protective film maximum concentration is calculated using its porosity (ϵ) [68]:

$$[\text{Film}]_{\max} = \rho_{\text{Film}} \times (1 - \epsilon). \quad (5.24)$$

In Eqs. 5.19, 5.21, and 5.22, \mathbf{u} is the velocity field from the surrounding fluid flow governed by the Stokes equation:

$$\begin{cases} -\nu \Delta \mathbf{u} + \nabla p + \frac{\nu}{K} \mathbf{u} = 0 \\ \nabla \cdot \mathbf{u} + \varepsilon p = 0. \end{cases} \quad (5.25)$$

in which \mathbf{u} is the fluid velocity, p is the pressure (which is actually pressure divided by the density), $\nu = \frac{\mu}{\rho}$ is the kinematic viscosity (with μ being the dynamic viscosity), and K is the permeability function.

The local pH can be calculated using the simulated concentration of hydroxide (Eq. 5.22):

$$\text{pH} = 14 + \log_{10} (C_{\text{OH}}/\text{MW}_{\text{OH}} \times 10^6), \quad (5.26)$$

with $\text{MW}_{\text{OH}} = 17.01$ being the molecular weight (MW) of the hydroxide ions.

The concentration of the hydroxyapatite-like precipitation (C_{Hydrox} in Eqs. 5.15 and 5.17) is calculated using the thermodynamics-based simulations (module 2) based on calculated local pH (Eq. 5.26) for each node of the desired domain. After solving the derived equations in each time step, the linking module passes the obtained local pH to the thermodynamics module to calculate the individual concentration of involved chemical components. Then, the individual concentrations are converted to the concentration of the hydroxyapatite-like precipitation by taking into account the stoichiometry of the formation reaction (Eq. 5.10), leading to the calculation of C_{Hydrox} for each node. After this, the total concentration of the film can be calculated according to Eq. 5.17 by passing back the calculated value to module 1.

The thermodynamics-based simulations were conducted using the Hydra-Medusa code [147–149], in which the input data of chemical equilibrium constants, solubility products, temperature, and involved chemical components

are used to generate a set of equilibrium diagrams correlating pH to concentration or fraction of desired chemical components. The experimental conditions, including the initial composition of the electrolyte (Table 5.2) and evaluated temperatures (25°C and 37°C), were given as input, and contributing components and solubility products were selected as represented in Table 5.3.

Table 5.3: Solubility products of related chemical reactions at 25°C (RT) and 37°C [150]

Chemical reaction	$pK_{sp} 25^{\circ}\text{C}$	$pK_{sp} 37^{\circ}\text{C}$
$\text{Ca}_5(\text{PO}_4)_3\text{OH} \rightarrow 5\text{Ca}^{2+} + 3\text{PO}_4^{3-} + \text{OH}^-$	54.46	58.77
$\text{Mg}(\text{OH})_2 \rightarrow \text{Mg}^{2+} + 2\text{OH}^-$	11.25	11.25
$\text{Ca}(\text{OH})_2 \rightarrow \text{Ca}^{2+} + 2\text{OH}^-$	5.20	5.38
$\text{MgCO}_3 \rightarrow \text{Mg}^{2+} + \text{CO}_3^{2-}$	8.03	5.51
$\text{CaCO}_3 \rightarrow \text{Ca}^{2+} + \text{CO}_3^{2-}$	8.48	8.44
$\text{Mg}_3(\text{PO}_4)_2 \rightarrow 3\text{Mg}^{2+} + 2\text{PO}_4^{3-}$	23.28	27.62
$\text{H}_2\text{O(l)} \rightarrow \text{H}^+(aq) + \text{OH}^-(aq)$	14.00	13.61
$\text{HCO}_3^-(aq) \rightarrow \text{CO}_3^{2-}(aq) + \text{H}^+(aq)$	10.33	10.24
$\text{HPO}_4^{2-}(aq) \rightarrow \text{PO}_4^{3-}(aq) + \text{H}^+(aq)$	12.35	12.32

The derived PDEs for the mechanistic model (Eqs. 5.19, 5.20, 5.21, and 5.22) were solved using a standard first-order finite element scheme. The open-source PDE solver FreeFEM [86] was used to implement the finite element model, resulting in a linear system of equations. The obtained equations were solved in parallel using efficient preconditioners and iterative solvers available in the open-source high-performance computing (HPC) toolkit PETSc [89]. The HYPRE BoomerAMG [87] and FieldSplit preconditioners were applied to the reaction-diffusion PDEs and the Stokes equations, respectively, and the GMRES solver [88] was used to solve the linear systems. Moreover, the computational mesh was partitioned and distributed among available computing resources using the HPDDM preconditioner [90]. Additionally, a Level-Set-based approach was employed to track the change of morphology of the degrading part, on the solution of which appropriate boundary conditions for the PDEs were applied via the penalization method. The details of this implementation are presented in our published works [131, 151] and Chapters 3 and ???. Since Eq. 5.22 is a non-linear PDE, a Picard-relaxation approach was followed to linearize this equation. The linking module (module 3) was implemented as a FreeFEM plugin in C++.

5.2.3 Simulation setup

Since the objective of the current study is to investigate local pH changes in regions close to the degrading metal, the computational domain was selected to include only a small portion of the chamber used in the experimental setup (Fig. 5.1). The domain was a $3 \times 3 \times 3$ mm cube on top of the degrading object, and the degrading block, represented as a disc with a diameter of 2mm and height of 0.3mm, was attached to the outside of the cube. The cube size was selected such that it represents the sample-centered area used in the experimental setup for line scan mapping. This setup is depicted in Fig. 5.3. The computational mesh was generated using a set of first-order tetrahedral elements, which was adaptively refined on the interface of the degrading sample to increase the numerical accuracy of the employed interface capturing technique. The Netgen mesh engine [91] in the SALOME platform [92] was used to generate the mesh. The generated mesh contained 290,997 elements with 51,757 degrees of freedom (DOF) for each equation.

The boundary conditions include an inlet on the left of the box, an outlet on the right, a wall on the bottom except where the degrading part exists, and a free slip on top. The inlet velocity was selected to be a linear profile ranging from zero on the bottom to $0.01\text{mm}.\text{s}^{-1}$ on the top, a value coming from solving the Navier-Stokes equations in the full chamber model (described in Chapter 4).

The values of model parameters were set based on our previous work [131] (Chapter 3), but the following assumptions were also applied for selecting the proper parameters of the coupled computational model:

1. Diffusion rate of hydroxide ions is 5-10 times more than the rate of Mg ions, so D_{OH} was set as $D_{\text{OH}} = 7.5D_{\text{Mg}}$ [146].
2. The hydroxyapatite-like precipitation does not form immediately at the beginning and emerges later [146, 150]. In the current model, it is set to start forming after the first hour of simulation time.
3. The magnesium hydroxide layer is thicker at 37°C [150], so the film elimination parameter (k_2) was set to be 50 times lower in this temperature in comparison to the room temperature.

The density of the electrolyte was selected to be $1.085 \times 10^{-3}\text{g}.\text{mm}^{-3}$, and the dynamic viscosity was set to $1.28 \times 10^{-3}\text{g}.\text{mm}^{-1}\text{s}^{-1}$. The simulations were carried out on the Snellius supercomputer using 100 CPU cores on a thin node with 256 GB of total memory.

5.3 Results

5.3.1 Thermodynamics-based simulation

Inputting the experimental conditions in the Hydra-Medusa software, including the initial composition of the electrolyte, temperature and the contributing chemical components, results in a big and complex output containing all the possible occurring chemical reactions. From this output, relevant reactions for the current biodegradation systems were filtered out, and the filtered reactions were converted to desired concentration units. Fig. 5.4 depicts the output of this process separately for simulations performed at 25°C (RT) and 37°C , showing how the concentration of relevant components varies with changing the environment pH. The solubility products of these simulations were taken from Table 5.3, and equilibrium concentrations were set to be equal to the electrolyte composition, listed in Table 5.2. These results (module 2) were used by the linking module (module 3) to provide equilibrium information for the mechanistic model (module 1).

5.3.2 Biodegradation simulations

In the current study, the local pH profiles, i.e., the pattern of pH changes in the region close to the degradation surface, were used to validate the developed coupled computational model. The comparison between computational predictions and experimental results was made in 3 different ways: 1) qualitative comparison of pH distribution above the degradable metal in a sample-centered square with an edge size of 3mm, 2) comparing the horizontal pH profiles, where the pH was measured over a line parallel to the sample, and 3) comparing vertical pH profiles, in which the pH was measured over a distance from the surface of the sample to the bulk of the electrolyte.

Fig. 5.5 shows a visualization of the local pH profiles from the top and side views for simulations performed at 25°C (RT) and 37°C after 12 hours. These patterns are comparable with the local pH distribution measured in the experiments, as shown in Fig. 5.6. In these figures, the flow is from left to right, advecting the released ions in the flow direction.

Quantitative profiles provide a more accurate comparison between the computational predictions and experimentally-obtained values. The horizontal profiles, also called line scans, are depicted in Fig. 5.8, in which the local pH changes are plotted over a horizontal line located $50\mu\text{m}$ above the surface of the sample. The profiles are shown separately for the experiments performed with CP and UHP Mg and the computational model. The results were recorded after 3, 6, and 12 hours of immersion.

Similarly, Fig. 5.8 shows the vertical pH profile after 12 hours of degradation, which was the final time of the simulation. The local pH is measured over a distance of 0.5mm vertically, starting from 50 μ m above the sample.

5.4 Discussion

In this study, an interface-coupled multiphysics biodegradation model was developed in order to predict the corrosion behavior in simulated body fluids in the presence of various chemical components. The quantity to compare with the experimental results was the predicted local pH, which reflects the capabilities of the model to capture the complex chemistry occurring near the biodegradation interface. For this end, our previous biodegradation model [131] (Chapter 3) was extended and coupled with a fluid flow model capturing the hydrodynamics condition. Then, the coupled model was linked to a thermodynamics-based code for computing the concentration of involved chemical components, the results of which were provided back to the biodegradation model via a linking module to compute the concentration of the precipitation layer.

It has been shown that the local pH changes can be a reflective characteristic of the biodegradation process in SBF-like solutions [146, 150]. Consequently, the vertical and horizontal local pH profiles can be reasonably used for the validation of the computational models of the biodegradation process. Capturing the complex interaction of various chemical components on the biodegradation interface in a mechanistic model can be a big challenge, especially for 3D cases with any arbitrary shape. That's why several modules were coupled in the current study to deliver such a model.

In this work, while the experiments were performed using CP and UHP Mg, the computational model does not take into account the difference in the elemental composition of these materials. Instead, the biodegradation model was developed by ignoring the effect of alloying elements and impurities. There are noticeable quantitative and qualitative variations in the obtained experimental results, such as different behavior of CP and UHP for horizontal pH profiles in line scan mappings (Fig. 5.7) and distribution of local pH above the sample (Fig. 5.6). However, these differences are still roughly the same behavior and quantity, which support the performed assumption and simplification of ignoring the dissimilarity of elemental composition. As a consequence, the computational results, including the pH profiles (Fig. 5.8), line scans (Fig. 5.7), and local pH distributions (Fig. 5.5), lies between the values and profiles obtained for CP and UHP Mg.

Recent studies on measuring local pH changes on the biodegradation sur-

face of Mg alloys show that the local values are different from the pH within the bulk of the electrolyte [146]. For example, in the tests performed by Mareci et al. [152], such observation was made when the vertical pH profiles were compared to the global pH values. Similar behavior was observed in the Wang et al. work [150]. Reproducing this behavior is problematic in mechanistic computational models due to the uniformity of the diffusion of hydroxide ions that change the pH. In other words, a uniform diffusion with a relatively high diffusion coefficient leads to the same local and global pH values. In the model presented here however, spatially dependent behavior was successfully reproduced *in silico* by letting a narrow film form at the beginning of the mechanistic biodegradation simulation and then computing the interaction of various ions in this narrow region by using the coupled thermodynamics-based code. Comparing the results of the predicted vertical pH profiles with the experimentally obtained curves (Fig. 5.8) shows good agreement, implying that the employed approach was able to mimic the complex chemistry on the biodegradation surface from a quantitative point of view. Yet, a different behavior can be observed further away from the surface where the local pH approaches the global value. In experimental results, this happens at a shorter distance from the implant compared to the computational predictions (Fig. 5.8) where yielding to the global pH seems to occur at longer distances from the biodegradation surface. This behavior can be confirmed by the visualization of computed pH (Fig. 5.5) and is due to the uniform diffusion mechanism of ions in the computational model, causing a gradient in the bulk part outside of the narrow formed region.

The results of horizontal line scan mapping on the surface of the sample and local pH distribution (Figs. 5.7 and 5.6) show that the pH starts to change in regions above the sample. In the computational predictions depicted in Fig. 5.7, the change of pH starts sharply when the line scan reaches the sample, a behavior rooted in the presence of the fluid flow model, which prevents ions from being diffused to the left, as shown in Fig. 5.5. Similarly, the advected ions in the direction of fluid flow (to the right in Fig. 5.5) prevent the pH value from decreasing dramatically where the sample ends in the line scan mapping. Moreover, the line scans show different behavior for experiments performed at room temperature compared to 37°C, especially for CP Mg samples. At RT, the horizontal pH profile tends to descend slightly over time, meaning that the profile measured after 3 hours of degradation is placed above the one measured after 12 hours. This behavior occurs oppositely for the measurement done at 37°C. The computational predictions of line scan profiles follow the same pattern, which could be due to how the coupled model computed the change of concentration of various chemical components and their contribution to the change of local pH.

Regarding the horizontal line scan results, a slight increase in the local pH values can be observed in the computational results in the region where the sample ends (Fig. 5.7). Although a similar behavior can be seen in the experimentally-obtained line scans (Fig. 5.6), it should be further investigated from the numerical implementation perspective to make sure that numerical artifacts do not contribute to it. One possible approach that may help remove numerical artifacts in this regard is to make the type of employed boundary conditions consistent in the employed fluid flow model. In the current model, a velocity condition was used for the inlet while the outlet condition was fixed pressure. Using the same type of boundary conditions for both inlet and outlet, meaning either assigning pressure conditions to the inlet or velocity to the outlet, can be considered in further extensions of the model to check their effect on the obtained local pH results.

As mentioned before, various chemical components of the electrolyte contribute differently to the change of pH, among which Ca^{2+} seems to have the most intricate effect [7]. It has been reported that in the absence of Ca^{2+} ions, the surface pH tends to be between 10 and 11, the typical range for pH value in biodegradation tests performed in saline solution [146]. This value is in line with the computational predictions of our previous study [131] (Chapter 3). However, in presence of Ca^{2+} cations, local pH between 7.8 and 8.5 and significantly lower degradation rates are reported [36, 153–155]. These findings are in line with the predictions made by the model presented in this chapter, obtained by coupling a mechanistic modeling approach and chemical equilibrium modeling, the latter of which considers the presence of Ca^{2+} .

The simplification assumptions made for developing the computational model, including the correlation between the diffusion rates of hydroxide and Mg ions, higher film elimination rate at room temperature, and the time at which the precipitation layer starts to form, can be seen as the limitations of the developed model. Regarding the latter mentioned assumption, the time was hard-coded into the model due to limitations of implementing the actual mechanisms of inducing the precipitation in the model. This can be improved in further developments of the model by incorporating a kinetics-based description of the precipitation layer formation, similar to the formation of magnesium hydroxide layer defined using a PDE (Eq. 5.20). This improvement will remove the necessity of the assumption made for linking the results obtained in equilibrium using the thermodynamics-based code (module 2) with the kinetics-based model (module 1), which was elaborated in section 5.2.2.

Knowing the mechanism of ionic activities at regions close to the biodegradation interface is crucial for comprehending the chemical process of Mg in complex solutions such as simulated physiological conditions. The developed

computational model can be seen as an facilitating tool for moving towards understanding these mechanisms by making it possible to virtually investigate the effective parameters such as the flow rate and environment composition. This knowledge will be helpful for biomedical applications where new coating and stabilization systems can be developed for different implantation environments.

5.5 Conclusion

In this chapter, the model developed in Chapter 3 was extended and combined with the fluid flow model developed in Chapter 4 to deliver a computational model of the biodegradation process in hydrodynamics conditions capable of predicting local pH changes close to the corrosion surface. In order to simulate local pH evolution in simulated body fluids, the precipitation of the hydroxyapatite-like protective model should be modeled. This was done by coupling the mentioned model with a thermodynamics-based code to compute the concentration of active chemical components contributing to the formation of the protective layer on the degradation interface. Results obtained from the coupled model show a good agreement with experimentally-obtained local pH measurements, demonstrating the effectiveness of the developed simulation workflow.

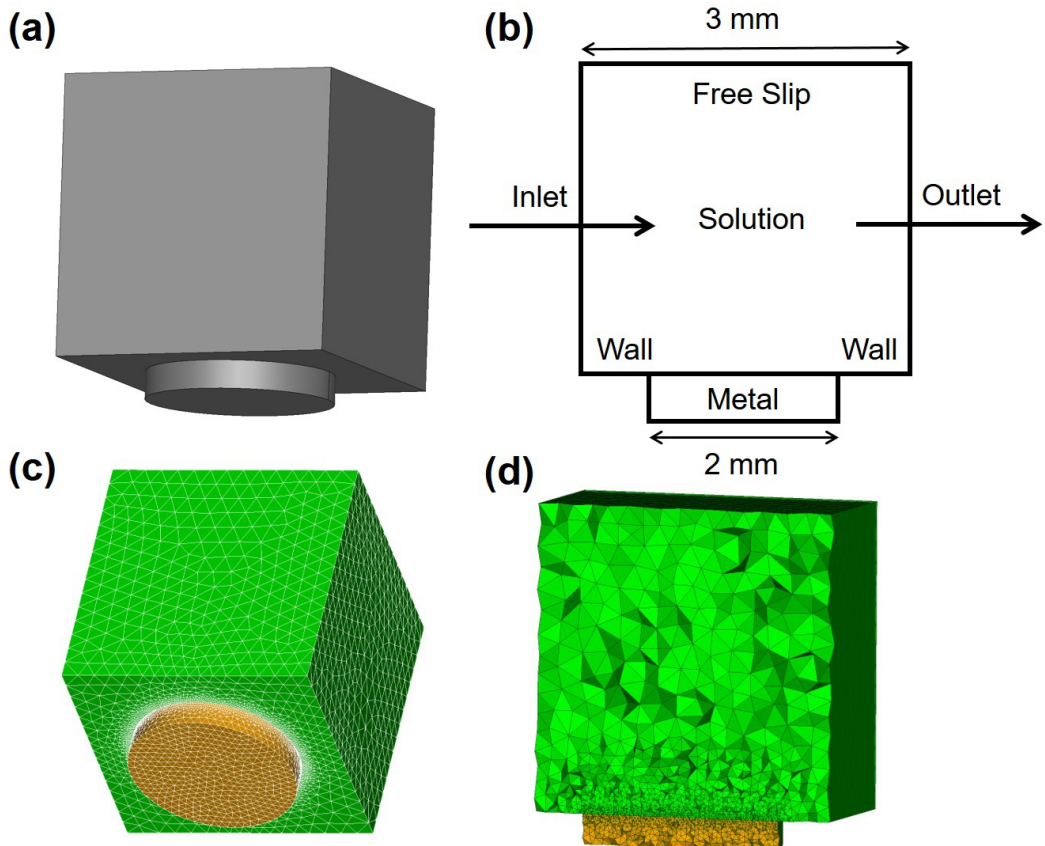


Figure 5.3: Computational model setup for local pH simulations: a) the geometry of the desired domain, being a small portion of the full chamber on top of the disc-like sample, b) the dimensions of the domain and applied boundary conditions for the fluid flow simulation, c) the generated computational mesh, depicting the flow region in green and the biodegradable sample in yellow, d) a cross-section of the mesh showing the refined meshing on the interface of the degradable metal.

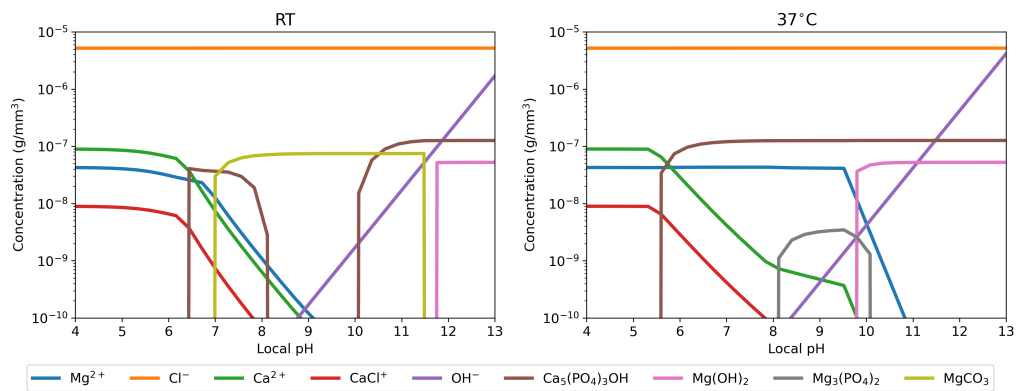


Figure 5.4: Selected relevant components from the Hydra-Medusa software output for given experimental conditions, showing how the concentration of various components vary with changing local pH

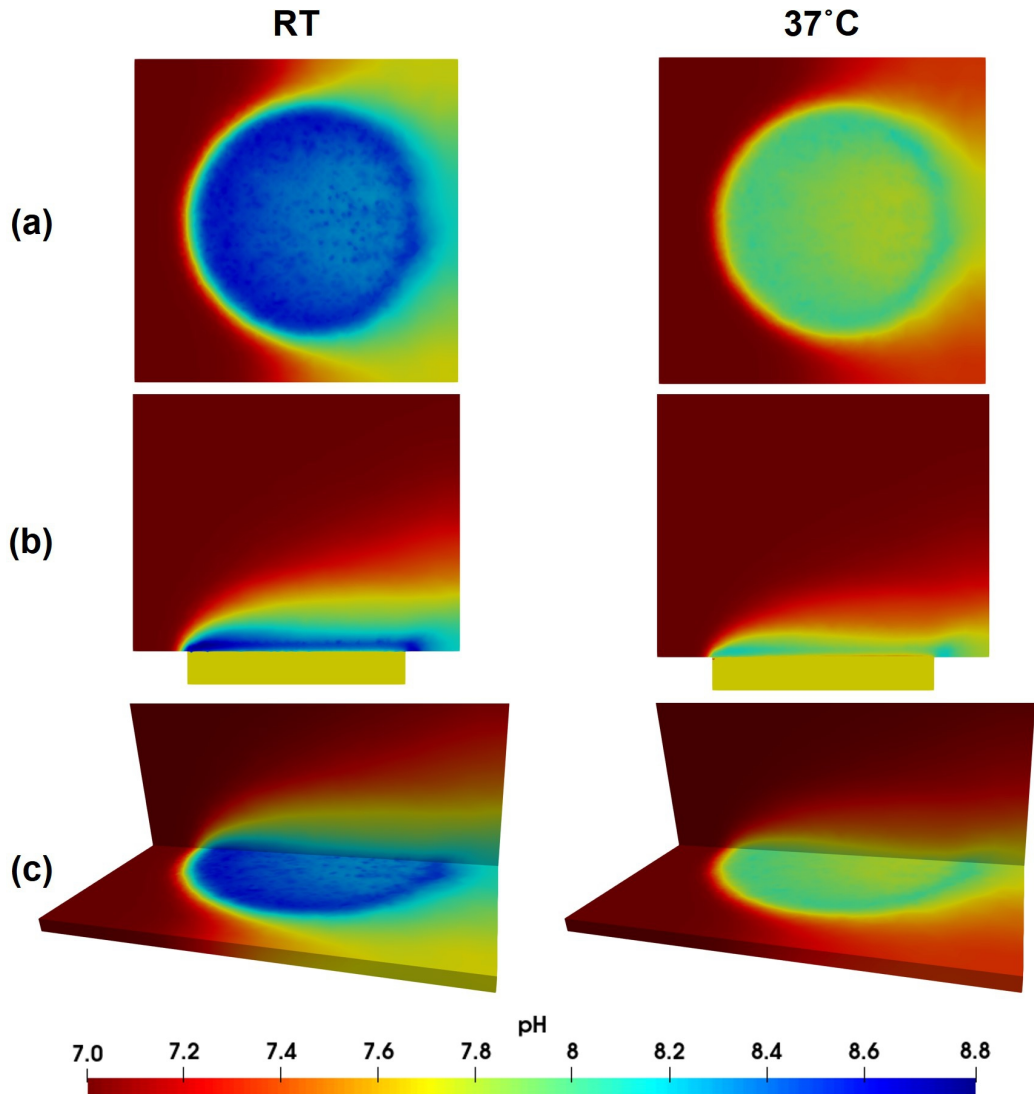


Figure 5.5: Simulation results for local pH predictions, depicting the local pH in a) top view from a horizontal cross-section, b) side view from a vertical cross-section, and c) perspective view with both the top and side cross sections, for simulations performed at 25°C (RT) and 37°C .

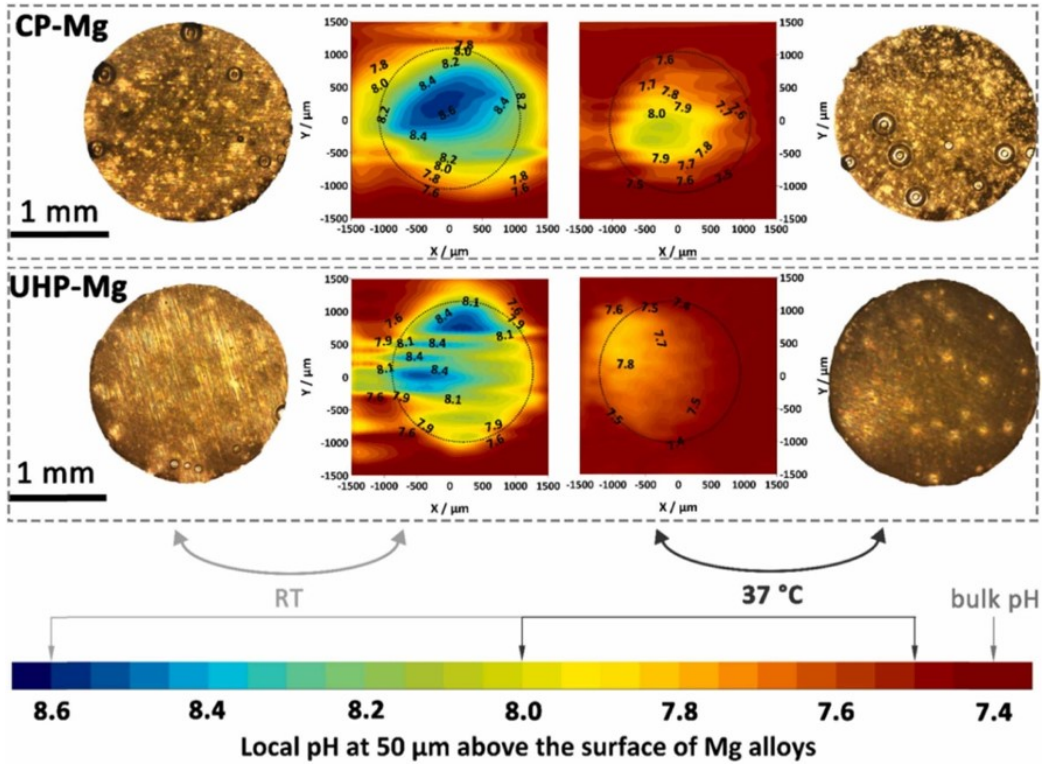


Figure 5.6: Experimental results for the distribution of local pH above the surface of the sample, measured after 12 hours of degradation.

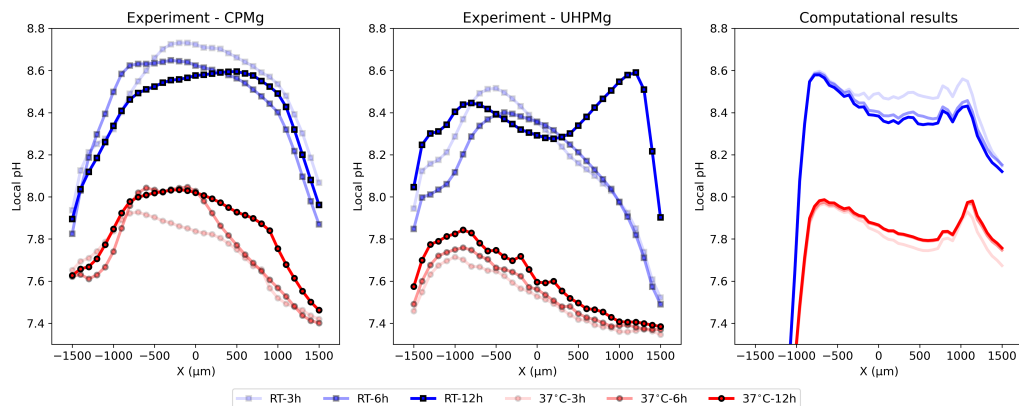


Figure 5.7: Comparing computational predictions and experimentally-obtained horizontal line scans of local pH changes, measured 50 μm above the surface of the sample after 3, 6, and 12 hours of degradation.

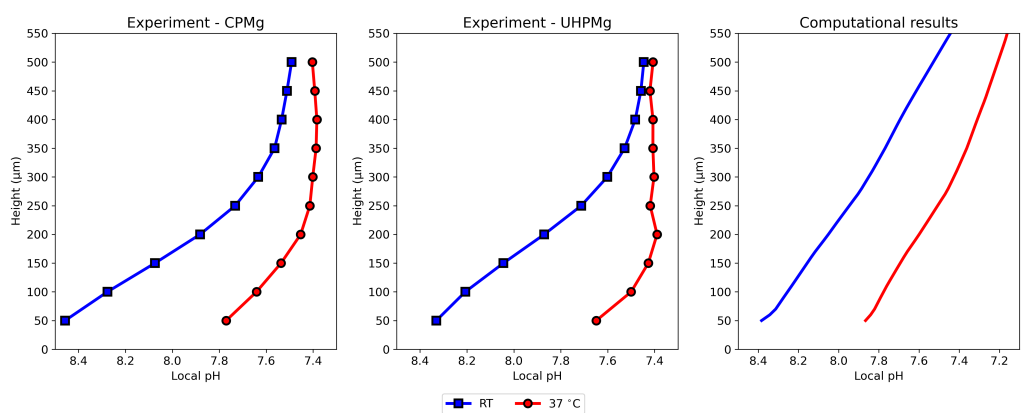


Figure 5.8: Comparing computational and experimental results for the local pH profiles, measured over a vertical line above the center of the sample after 12 hours of immersion.

Bibliography

- [1] Y. Gao, L. Wang, and Y. Fan, “Biomechanics of magnesium-based implant during tissue repair,” in *Biomechanics of Injury and Prevention*, pp. 335–361, Springer Nature Singapore, 2022.
- [2] Y. Zheng, X. Gu, and F. Witte, “Biodegradable metals,” *Materials Science and Engineering: R: Reports*, vol. 77, pp. 1–34, mar 2014.
- [3] Y. Liu, Y. Zheng, X.-H. Chen, J.-A. Yang, H. Pan, D. Chen, L. Wang, J. Zhang, D. Zhu, S. Wu, K. W. K. Yeung, R.-C. Zeng, Y. Han, and S. Guan, “Fundamental theory of biodegradable metals—definition, criteria, and design,” *Advanced Functional Materials*, vol. 29, p. 1805402, feb 2019.
- [4] H.-S. Han, S. Loffredo, I. Jun, J. Edwards, Y.-C. Kim, H.-K. Seok, F. Witte, D. Mantovani, and S. Glyn-Jones, “Current status and outlook on the clinical translation of biodegradable metals,” *Materials Today*, vol. 23, pp. 57–71, mar 2019.
- [5] D. Zhao, F. Witte, F. Lu, J. Wang, J. Li, and L. Qin, “Current status on clinical applications of magnesium-based orthopaedic implants: A review from clinical translational perspective,” *Biomaterials*, vol. 112, pp. 287–302, jan 2017.
- [6] Z. ZHEN, T. fei XI, and Y. feng ZHENG, “A review on in vitro corrosion performance test of biodegradable metallic materials,” *Transactions of Nonferrous Metals Society of China*, vol. 23, pp. 2283–2293, aug 2013.
- [7] R. Willumeit-Römer, “The interface between degradable mg and tissue,” *JOM*, vol. 71, pp. 1447–1455, feb 2019.
- [8] J. Venezuela and M. Dargusch, “The influence of alloying and fabrication techniques on the mechanical properties, biodegradability and

- biocompatibility of zinc: A comprehensive review,” *Acta Biomaterialia*, vol. 87, pp. 1–40, mar 2019.
- [9] E. Mostaed, M. Sikora-Jasinska, J. W. Drelich, and M. Vedani, “Zinc-based alloys for degradable vascular stent applications,” *Acta Biomaterialia*, vol. 71, pp. 1–23, apr 2018.
 - [10] M. Schinhammer, A. C. Hänzi, J. F. Löffler, and P. J. Uggowitzer, “Design strategy for biodegradable fe-based alloys for medical applications,” *Acta Biomaterialia*, vol. 6, pp. 1705–1713, may 2010.
 - [11] M. Esmaily, J. Svensson, S. Fajardo, N. Birbilis, G. Frankel, S. Virtanen, R. Arrabal, S. Thomas, and L. Johansson, “Fundamentals and advances in magnesium alloy corrosion,” *Progress in Materials Science*, vol. 89, pp. 92–193, aug 2017.
 - [12] B. Heublein, “Biocorrosion of magnesium alloys: a new principle in cardiovascular implant technology?,” *Heart*, vol. 89, pp. 651–656, jun 2003.
 - [13] M. P. Staiger, A. M. Pietak, J. Huadmai, and G. Dias, “Magnesium and its alloys as orthopedic biomaterials: A review,” *Biomaterials*, vol. 27, pp. 1728–1734, mar 2006.
 - [14] J. Walker, S. Shadanbaz, T. B. F. Woodfield, M. P. Staiger, and G. J. Dias, “Magnesium biomaterials for orthopedic application: A review from a biological perspective,” *Journal of Biomedical Materials Research Part B: Applied Biomaterials*, vol. 102, pp. 1316–1331, jan 2014.
 - [15] F. Cecchinato, N. A. Agha, A. H. Martinez-Sanchez, B. J. C. Luthringer, F. Feyerabend, R. Jimbo, R. Willumeit-Römer, and A. Wennerberg, “Influence of magnesium alloy degradation on undifferentiated human cells,” *PLOS ONE*, vol. 10, p. e0142117, nov 2015.
 - [16] E. Crubzy, P. Murail, L. Girard, and J.-P. Bernadou, “False teeth of the roman world,” *Nature*, vol. 391, pp. 29–29, jan 1998.
 - [17] J.-L. Wang, J.-K. Xu, C. Hopkins, D. H.-K. Chow, and L. Qin, “Biodegradable magnesium-based implants in orthopedics—a general review and perspectives,” *Advanced Science*, vol. 7, p. 1902443, feb 2020.
 - [18] B. Wegener, A. Sichler, S. Milz, C. Sprecher, K. Pieper, W. Hermanns, V. Jansson, B. Nies, B. Kieback, P. E. Müller, V. Wegener,

- and P. Quadbeck, “Development of a novel biodegradable porous iron-based implant for bone replacement,” *Scientific Reports*, vol. 10, jun 2020.
- [19] G. Gąsior, J. Szczepański, and A. Radtke, “Biodegradable iron-based materials—what was done and what more can be done?,” *Materials*, vol. 14, p. 3381, jun 2021.
 - [20] H.-S. Han, I. Jun, H.-K. Seok, K.-S. Lee, K. Lee, F. Witte, D. Mantovani, Y.-C. Kim, S. Glyn-Jones, and J. R. Edwards, “Biodegradable magnesium alloys promote angio-osteogenesis to enhance bone repair,” *Advanced Science*, vol. 7, p. 2000800, jun 2020.
 - [21] G. K. Levy, J. Goldman, and E. Aghion, “The prospects of zinc as a structural material for biodegradable implants—a review paper,” *Materials*, vol. 7, p. 402, oct 2017.
 - [22] X. Liu, J. Sun, Y. Yang, Z. Pu, and Y. Zheng, “In vitro investigation of ultra-pure zn and its mini-tube as potential bioabsorbable stent material,” *Materials Letters*, vol. 161, pp. 53–56, dec 2015.
 - [23] J. Vormann, “Magnesium: nutrition and metabolism,” *Molecular Aspects of Medicine*, vol. 24, pp. 27–37, feb 2003.
 - [24] R. J. Elin, “Magnesium metabolism in health and disease,” *Disease-a-Month*, vol. 34, pp. 166–218, apr 1988.
 - [25] F. Witte, “The history of biodegradable magnesium implants: A review,” *Acta Biomaterialia*, vol. 6, pp. 1680–1692, may 2010.
 - [26] N. Ikeo, R. Nakamura, K. Naka, T. Hashimoto, T. Yoshida, T. Urade, K. Fukushima, H. Yabuuchi, T. Fukumoto, Y. Ku, and T. Mukai, “Fabrication of a magnesium alloy with excellent ductility for biodegradable clips,” *Acta Biomaterialia*, vol. 29, pp. 468–476, jan 2016.
 - [27] R. Erbel, C. D. Mario, J. Bartunek, J. Bonnier, B. de Bruyne, F. R. Eberli, P. Erne, M. Haude, B. Heublein, M. Horrigan, C. Ilsley, D. Böse, J. Koolen, T. F. Lüscher, N. Weissman, and R. Waksman, “Temporary scaffolding of coronary arteries with bioabsorbable magnesium stents: a prospective, non-randomised multicentre trial,” *The Lancet*, vol. 369, pp. 1869–1875, jun 2007.
 - [28] Y. Sotomi, Y. Onuma, C. Collet, E. Tenekecioglu, R. Virmani, N. S. Kleiman, and P. W. Serruys, “Bioresorbable scaffold,” *Circulation Research*, vol. 120, pp. 1341–1352, apr 2017.

- [29] H. M. Garcia-Garcia, M. Haude, K. Kuku, A. Hideo-Kajita, H. Ince, A. Abizaid, R. Tölg, P. A. Lemos, C. von Birgelen, E. H. Christiansen, W. Wijns, J. Escaned, J. Dijkstra, and R. Waksman, “In vivo serial invasive imaging of the second-generation drug-eluting absorbable metal scaffold (magmaris — DREAMS 2g) in de novo coronary lesions: Insights from the BIOSOLVE-II first-in-man trial,” *International Journal of Cardiology*, vol. 255, pp. 22–28, mar 2018.
- [30] A. LAMBOTTE, “Technique et indication des prothèses dans le traitement des fractures,” *Presse med*, vol. 17, p. 321, 1909.
- [31] A. Lambotte, “L’utilisation du magnésium comme matériel perdu dans l’ostéosynthèse,” *Bull Mem Soc Nat Chir*, vol. 28, no. 3, pp. 1325–1334, 1932.
- [32] F. Witte, V. Kaese, H. Haferkamp, E. Switzer, A. Meyer-Lindenberg, C. Wirth, and H. Windhagen, “In vivo corrosion of four magnesium alloys and the associated bone response,” *Biomaterials*, vol. 26, pp. 3557–3563, jun 2005.
- [33] C. Wang, D. Mei, G. Wiese, L. Wang, M. Deng, S. V. Lamaka, and M. L. Zheludkevich, “High rate oxygen reduction reaction during corrosion of ultra-high-purity magnesium,” *npj Materials Degradation*, vol. 4, dec 2020.
- [34] S. Huang, B. Wang, X. Zhang, F. Lu, Z. Wang, S. Tian, D. Li, J. Yang, F. Cao, L. Cheng, Z. Gao, Y. Li, K. Qin, and D. Zhao, “High-purity weight-bearing magnesium screw: Translational application in the healing of femoral neck fracture,” *Biomaterials*, vol. 238, p. 119829, apr 2020.
- [35] D. Mei, S. V. Lamaka, X. Lu, and M. L. Zheludkevich, “Selecting medium for corrosion testing of bioabsorbable magnesium and other metals – a critical review,” *Corrosion Science*, vol. 171, p. 108722, jul 2020.
- [36] D. Mei, S. V. Lamaka, J. Gonzalez, F. Feyerabend, R. Willumeit-Römer, and M. L. Zheludkevich, “The role of individual components of simulated body fluid on the corrosion behavior of commercially pure mg,” *Corrosion Science*, vol. 147, pp. 81–93, feb 2019.
- [37] R.-C. Zeng, Y. Hu, S.-K. Guan, H.-Z. Cui, and E.-H. Han, “Corrosion of magnesium alloy AZ31: The influence of bicarbonate, sulphate, hy-

- drogen phosphate and dihydrogen phosphate ions in saline solution,” *Corrosion Science*, vol. 86, pp. 171–182, sep 2014.
- [38] S. Johnston, M. Dargusch, and A. Atrens, “Building towards a standardised approach to biocorrosion studies: a review of factors influencing mg corrosion in vitro pertinent to in vivo corrosion,” *Science China Materials*, vol. 61, pp. 475–500, dec 2017.
 - [39] S. V. Lamaka, J. Gonzalez, D. Mei, F. Feyerabend, R. Willumeit-Römer, and M. L. Zheludkevich, “Local pH and its evolution near mg alloy surfaces exposed to simulated body fluids,” *Advanced Materials Interfaces*, vol. 5, p. 1800169, jun 2018.
 - [40] D. Mei, S. V. Lamaka, C. Feiler, and M. L. Zheludkevich, “The effect of small-molecule bio-relevant organic components at low concentration on the corrosion of commercially pure mg and mg-0.8ca alloy: An overall perspective,” *Corrosion Science*, vol. 153, pp. 258–271, jun 2019.
 - [41] B. Hadzima, M. Mhaede, and F. Pastorek, “Electrochemical characteristics of calcium-phosphatized AZ31 magnesium alloy in 0.9 % NaCl solution,” *Journal of Materials Science: Materials in Medicine*, vol. 25, pp. 1227–1237, jan 2014.
 - [42] X. Lu, Y. Li, P. Ju, Y. Chen, J. Yang, K. Qian, T. Zhang, and F. Wang, “Unveiling the inhibition mechanism of an effective inhibitor for AZ91 mg alloy,” *Corrosion Science*, vol. 148, pp. 264–271, mar 2019.
 - [43] Y. Li, X. Lu, K. Wu, L. Yang, T. Zhang, and F. Wang, “Exploration the inhibition mechanism of sodium dodecyl sulfate on mg alloy,” *Corrosion Science*, vol. 168, p. 108559, may 2020.
 - [44] A. Atrens, G.-L. Song, M. Liu, Z. Shi, F. Cao, and M. S. Dargusch, “Review of recent developments in the field of magnesium corrosion,” *Advanced Engineering Materials*, vol. 17, pp. 400–453, jan 2015.
 - [45] C. Schille, M. Braun, H. Wendel, L. Scheideler, N. Hort, H.-P. Reichel, E. Schweizer, and J. Geis-Gerstorfer, “Corrosion of experimental magnesium alloys in blood and PBS: A gravimetric and microscopic evaluation,” *Materials Science and Engineering: B*, vol. 176, pp. 1797–1801, dec 2011.
 - [46] D. Xue, Y. Yun, Z. Tan, Z. Dong, and M. J. Schulz, “In vivo and in vitro degradation behavior of magnesium alloys as biomaterials,”

Journal of Materials Science & Technology, vol. 28, pp. 261–267, mar 2012.

- [47] Y. Xin, T. Hu, and P. K. Chu, “Degradation behaviour of pure magnesium in simulated body fluids with different concentrations of hco₃,” *Corrosion Science*, vol. 53, pp. 1522–1528, apr 2011.
- [48] S. Johnston, Z. Shi, and A. Atrens, “The influence of pH on the corrosion rate of high-purity mg, AZ91 and ZE41 in bicarbonate buffered hanks’ solution,” *Corrosion Science*, vol. 101, pp. 182–192, dec 2015.
- [49] S. Johnston, Z. Shi, J. Venezuela, C. Wen, M. S. Dargusch, and A. Atrens, “Investigating mg biocorrosion in vitro: Lessons learned and recommendations,” *JOM*, vol. 71, pp. 1406–1413, jan 2019.
- [50] M. Pogorielov, E. Husak, A. Solodivnik, and S. Zhdanov, “Magnesium-based biodegradable alloys: Degradation, application, and alloying elements,” *Interventional Medicine and Applied Science*, vol. 9, pp. 27–38, mar 2017.
- [51] J. Walker, S. Shadanbaz, N. T. Kirkland, E. Stace, T. Woodfield, M. P. Staiger, and G. J. Dias, “Magnesium alloys: Predicting in vivo corrosion with in vitro immersion testing,” *Journal of Biomedical Materials Research Part B: Applied Biomaterials*, vol. 100B, pp. 1134–1141, feb 2012.
- [52] X. Gu, Y. Zheng, Y. Cheng, S. Zhong, and T. Xi, “In vitro corrosion and biocompatibility of binary magnesium alloys,” *Biomaterials*, vol. 30, pp. 484–498, feb 2009.
- [53] N. I. Z. Abidin, B. Rolfe, H. Owen, J. Malisano, D. Martin, J. Hofstetter, P. J. Uggowitzer, and A. Atrens, “The in vivo and in vitro corrosion of high-purity magnesium and magnesium alloys WZ21 and AZ91,” *Corrosion Science*, vol. 75, pp. 354–366, oct 2013.
- [54] H. Wang and Z. Shi, “In vitro biodegradation behavior of magnesium and magnesium alloy,” *Journal of Biomedical Materials Research Part B: Applied Biomaterials*, vol. 98B, pp. 203–209, jul 2011.
- [55] W. R. Barfield, G. Colbath, J. D. DesJardins, Y. H. An, and L. A. Hartsock, “The potential of magnesium alloy use in orthopaedic surgery,” *Current Orthopaedic Practice*, vol. 23, pp. 146–150, mar 2012.

- [56] A. H. M. Sanchez, B. J. Luthringer, F. Feyerabend, and R. Willumeit, “Mg and mg alloys: How comparable are in vitro and in vivo corrosion rates? a review,” *Acta Biomaterialia*, vol. 13, pp. 16–31, feb 2015.
- [57] E. L. Boland, R. Shine, N. Kelly, C. A. Sweeney, and P. E. McHugh, “A review of material degradation modelling for the analysis and design of bioabsorbable stents,” *Annals of Biomedical Engineering*, vol. 44, pp. 341–356, aug 2015.
- [58] J. A. Sanz-Herrera and E. Reina-Romo, “Continuum modeling and simulation in bone tissue engineering,” *Applied Sciences*, vol. 9, p. 3674, sep 2019.
- [59] Y. Gao, L. Wang, X. Gu, Z. Chu, M. Guo, and Y. Fan, “A quantitative study on magnesium alloy stent biodegradation,” *Journal of Biomechanics*, vol. 74, pp. 98–105, jun 2018.
- [60] D. Liu, S. Hu, X. Yin, J. Liu, Z. Jia, and Q. Li, “Degradation mechanism of magnesium alloy stent under simulated human micro-stress environment,” *Materials Science and Engineering: C*, vol. 84, pp. 263–270, mar 2018.
- [61] E. L. Boland, J. A. Grogan, and P. E. McHugh, “Computational modelling of magnesium stent mechanical performance in a remodelling artery: Effects of multiple remodelling stimuli,” *International Journal for Numerical Methods in Biomedical Engineering*, vol. 35, aug 2019.
- [62] A.-K. Gartzke, S. Julmi, C. Klose, A.-C. Waselau, A. Meyer-Lindenberg, H. J. Maier, S. Besdo, and P. Wriggers, “A simulation model for the degradation of magnesium-based bone implants,” *Journal of the Mechanical Behavior of Biomedical Materials*, vol. 101, p. 103411, jan 2020.
- [63] D. Gastaldi, V. Sassi, L. Petrini, M. Vedani, S. Trasatti, and F. Migliavacca, “Continuum damage model for bioresorbable magnesium alloy devices — application to coronary stents,” *Journal of the Mechanical Behavior of Biomedical Materials*, vol. 4, pp. 352–365, apr 2011.
- [64] W. Shi, H. Li, K. Mitchell, C. Zhang, T. Zhu, Y. Jin, and D. Zhao, “A multi-dimensional non-uniform corrosion model for bioabsorbable metallic vascular stents,” *Acta Biomaterialia*, vol. 131, pp. 572–580, sep 2021.

- [65] S. Ahmed, J. Ward, and Y. Liu, “Numerical modelling of effects of biphasic layers of corrosion products to the degradation of magnesium metal in vitro,” *Materials*, vol. 11, p. 1, dec 2017.
- [66] J. Grogan, S. Leen, and P. McHugh, “A physical corrosion model for bioabsorbable metal stents,” *Acta Biomaterialia*, vol. 10, pp. 2313–2322, may 2014.
- [67] Z. Shen, M. Zhao, D. Bian, D. Shen, X. Zhou, J. Liu, Y. Liu, H. Guo, and Y. Zheng, “Predicting the degradation behavior of magnesium alloys with a diffusion-based theoretical model and in vitro corrosion testing,” *Journal of Materials Science & Technology*, vol. 35, pp. 1393–1402, jul 2019.
- [68] P. Bajger, J. M. A. Ashbourn, V. Manhas, Y. Guyot, K. Lietaert, and L. Geris, “Mathematical modelling of the degradation behaviour of biodegradable metals,” *Biomechanics and Modeling in Mechanobiology*, vol. 16, pp. 227–238, aug 2016.
- [69] J. Sanz-Herrera, E. Reina-Romo, and A. Boccaccini, “In silico design of magnesium implants: Macroscopic modeling,” *Journal of the Mechanical Behavior of Biomedical Materials*, vol. 79, pp. 181–188, mar 2018.
- [70] T. Albaraghtheh, R. Willumeit-Römer, and B. Zeller-Plumhoff, “In silico studies of magnesium-based implants: A review of the current stage and challenges,” *Journal of Magnesium and Alloys*, vol. 10, pp. 2968–2996, nov 2022.
- [71] Y. Chen, Z. Xu, C. Smith, and J. Sankar, “Recent advances on the development of magnesium alloys for biodegradable implants,” *Acta Biomaterialia*, vol. 10, pp. 4561–4573, nov 2014.
- [72] Y. Qin, P. Wen, H. Guo, D. Xia, Y. Zheng, L. Jauer, R. Poprawe, M. Voshage, and J. H. Schleifenbaum, “Additive manufacturing of biodegradable metals: Current research status and future perspectives,” *Acta Biomaterialia*, vol. 98, pp. 3 – 22, 2019.
- [73] U. Riaz, I. Shabib, and W. Haider, “The current trends of mg alloys in biomedical applications—a review,” *Journal of Biomedical Materials Research Part B: Applied Biomaterials*, dec 2018.
- [74] Y. Xin, K. Huo, H. Tao, G. Tang, and P. K. Chu, “Influence of aggressive ions on the degradation behavior of biomedical magnesium alloy in

physiological environment,” *Acta Biomaterialia*, vol. 4, pp. 2008–2015, nov 2008.

- [75] J. W. Wilder, C. Clemons, D. Golovaty, K. L. Kreider, G. W. Young, and R. S. Lillard, “An adaptive level set approach for modeling damage due to galvanic corrosion,” *Journal of Engineering Mathematics*, vol. 91, pp. 121–142, nov 2014.
- [76] W. Sun, G. Liu, L. Wang, T. Wu, and Y. Liu, “An arbitrary lagrangian–eulerian model for studying the influences of corrosion product deposition on bimetallic corrosion,” *Journal of Solid State Electrochemistry*, vol. 17, pp. 829–840, nov 2012.
- [77] Y. Wang, J. Pan, X. Han, C. Sinka, and L. Ding, “A phenomenological model for the degradation of biodegradable polymers,” *Biomaterials*, vol. 29, no. 23, pp. 3393–3401, 2008.
- [78] P. Grindrod, *The theory and applications of reaction-diffusion equations : patterns and waves*. Oxford University Press, 1996.
- [79] J. Crank, *Free and Moving Boundary Problems*. OUP Oxford, 1987.
- [80] S. O. Ronald Fedkiw, *Level Set Methods and Dynamic Implicit Surfaces*. Springer New York, 2002.
- [81] M. Strebl, M. Bruns, and S. Virtanen, “Editors’ choice—respirometric in situ methods for real-time monitoring of corrosion rates: Part i. atmospheric corrosion,” *Journal of The Electrochemical Society*, vol. 167, p. 021510, jan 2020.
- [82] E. L. Silva, S. V. Lamaka, D. Mei, and M. L. Zheludkevich, “The reduction of dissolved oxygen during magnesium corrosion,” *ChemistryOpen*, vol. 7, pp. 664–668, aug 2018.
- [83] P. Grathwohl, *Diffusion in Natural Porous Media: Contaminant Transport, Sorption/Desorption and Dissolution Kinetics*. Springer US, 1998.
- [84] D. Höche, “Simulation of corrosion product deposit layer growth on bare magnesium galvanically coupled to aluminum,” *Journal of The Electrochemical Society*, vol. 162, pp. C1–C11, nov 2014.
- [85] S. Scheiner and C. Hellmich, “Stable pitting corrosion of stainless steel as diffusion-controlled dissolution process with a sharp moving electrode boundary,” *Corrosion Science*, vol. 49, pp. 319–346, feb 2007.

- [86] F. Hecht, “New development in freefem++,” *J. Numer. Math.*, vol. 20, no. 3-4, pp. 251–265, 2012.
- [87] R. D. Falgout and U. M. Yang, “hypre: A library of high performance preconditioners,” in *Lecture Notes in Computer Science*, pp. 632–641, Springer Berlin Heidelberg, 2002.
- [88] Y. Saad and M. H. Schultz, “Gmres: A generalized minimal residual algorithm for solving nonsymmetric linear systems,” *SIAM Journal on Scientific and Statistical Computing*, vol. 7, no. 3, pp. 856–869, 1986.
- [89] S. Balay, S. Abhyankar, M. F. Adams, J. Brown, P. Brune, K. Buschelman, L. Dalcin, A. Dener, V. Eijkhout, W. D. Gropp, D. Karpeyev, D. Kaushik, M. G. Knepley, D. A. May, L. C. McInnes, R. T. Mills, T. Munson, K. Rupp, P. Sanan, B. F. Smith, S. Zampini, H. Zhang, and H. Zhang, “PETSc Web page.” <https://www.mcs.anl.gov/petsc>, 2019.
- [90] P. Jolivet, F. Hecht, F. Nataf, and C. Prud’homme, “Scalable domain decomposition preconditioners for heterogeneous elliptic problems,” in *Proceedings of the International Conference on High Performance Computing, Networking, Storage and Analysis, SC ’13*, (New York, NY, USA), Association for Computing Machinery, 2013.
- [91] J. Schöberl, “NETGEN an advancing front 2d/3d-mesh generator based on abstract rules,” *Computing and Visualization in Science*, vol. 1, pp. 41–52, jul 1997.
- [92] A. Ribes and C. Caremoli, “Salome platform component model for numerical simulation,” in *31st Annual International Computer Software and Applications Conference - Vol. 2 - (COMPSAC 2007)*, IEEE, jul 2007.
- [93] J. Mockus, *Bayesian Approach to Global Optimization*. Springer Netherlands, 1989.
- [94] M. Mehrian, Y. Guyot, I. Papantoniou, S. Olofsson, M. Sonnaert, R. Misener, and L. Geris, “Maximizing neotissue growth kinetics in a perfusion bioreactor: An in silico strategy using model reduction and bayesian optimization,” *Biotechnology and Bioengineering*, vol. 115, pp. 617–629, dec 2017.

- [95] S. H. Lee and J. C. Rasaiah, “Proton transfer and the mobilities of the H⁺ and OH⁻ ions from studies of a dissociating model for water,” *The Journal of Chemical Physics*, vol. 135, p. 124505, sep 2011.
- [96] J. S. H. Graham C. Hill, *Chemistry in Context - Laboratory Manual*. Oxford University Press, 2001.
- [97] M. Abdalla, A. Joplin, M. Elahinia, and H. Ibrahim, “Corrosion modeling of magnesium and its alloys for biomedical applications: Review,” *Corrosion and Materials Degradation*, vol. 1, pp. 219–248, jul 2020.
- [98] R. J. Santucci, M. E. McMahon, and J. R. Scully, “Utilization of chemical stability diagrams for improved understanding of electrochemical systems: evolution of solution chemistry towards equilibrium,” *npj Materials Degradation*, vol. 2, jan 2018.
- [99] K. B. Deshpande, “Numerical modeling of micro-galvanic corrosion,” *Electrochimica Acta*, vol. 56, pp. 1737–1745, jan 2011.
- [100] O. Dolgikh, H. Simillion, S. V. Lamaka, A. C. Bastos, H. B. Xue, M. G. Taryba, A. R. Oliveira, C. Allély, B. V. D. Bossche, K. V. D. Bergh, J. D. Strycker, and J. Deconinck, “Corrosion protection of steel cut-edges by hot-dip galvanized al(zn,mg) coatings in 1 wt% NaCl: Part II. numerical simulations,” *Materials and Corrosion*, vol. 70, pp. 780–792, jan 2019.
- [101] V. I. Sikavitsas, G. N. Bancroft, J. J. Lemoine, M. A. K. Liebschner, M. Dauner, and A. G. Mikos, “Flow perfusion enhances the calcified matrix deposition of marrow stromal cells in biodegradable nonwoven fiber mesh scaffolds,” *Annals of Biomedical Engineering*, vol. 33, pp. 63–70, jan 2005.
- [102] W. L. Grayson, D. Marolt, S. Bhumiratana, M. Fröhlich, X. E. Guo, and G. Vunjak-Novakovic, “Optimizing the medium perfusion rate in bone tissue engineering bioreactors,” *Biotechnology and Bioengineering*, vol. 108, pp. 1159–1170, dec 2010.
- [103] M. Sonnaert, I. Papantoniou, V. Bloemen, G. Kerckhofs, F. P. Luyten, and J. Schrooten, “Human periosteal-derived cell expansion in a perfusion bioreactor system: proliferation, differentiation and extracellular matrix formation,” *Journal of Tissue Engineering and Regenerative Medicine*, vol. 11, pp. 519–530, sep 2014.

- [104] M. J. Song, D. Dean, and M. L. K. Tate, “Mechanical modulation of nascent stem cell lineage commitment in tissue engineering scaffolds,” *Biomaterials*, vol. 34, pp. 5766–5775, jul 2013.
- [105] R. McCoy, C. Jungreuthmayer, and F. O'Brien, “Influence of flow rate and scaffold pore size on cell behavior during mechanical stimulation in a flow perfusion bioreactor,” *Biotechnology and Bioengineering*, vol. 109, pp. 1583–1594, jan 2012.
- [106] J. Rauh, F. Milan, K.-P. Günther, and M. Stiehler, “Bioreactor systems for bone tissue engineering,” *Tissue Engineering Part B: Reviews*, vol. 17, pp. 263–280, aug 2011.
- [107] I. Papantoniou, Y. C. Chai, F. P. Luyten, and J. Schrooten, “Process quality engineering for bioreactor-driven manufacturing of tissue-engineered constructs for bone regeneration,” *Tissue Engineering Part C: Methods*, vol. 19, pp. 596–609, aug 2013.
- [108] J. Wang, V. Giridharan, V. Shanov, Z. Xu, B. Collins, L. White, Y. Jang, J. Sankar, N. Huang, and Y. Yun, “Flow-induced corrosion behavior of absorbable magnesium-based stents,” *Acta Biomaterialia*, vol. 10, pp. 5213–5223, dec 2014.
- [109] J. Lévesque, H. Hermawan, D. Dubé, and D. Mantovani, “Design of a pseudo-physiological test bench specific to the development of biodegradable metallic biomaterials,” *Acta Biomaterialia*, vol. 4, pp. 284–295, mar 2008.
- [110] N. Li, C. Guo, Y. H. Wu, Y. F. Zheng, and L. Q. Ruan, “Comparative study on corrosion behaviour of pure mg and WE43 alloy in static, stirring and flowing hank's solution,” *Corrosion Engineering, Science and Technology*, vol. 47, pp. 346–351, aug 2012.
- [111] K. Jafarzadeh, T. Shahrabi, and A. A. Oskouei, “Novel approach using EIS to study flow accelerated pitting corrosion of AA5083-h321 aluminum–magnesium alloy in NaCl solution,” *Journal of Applied Electrochemistry*, vol. 39, pp. 1725–1731, mar 2009.
- [112] Y. Chen, S. Zhang, J. Li, Y. Song, C. Zhao, and X. Zhang, “Dynamic degradation behavior of MgZn alloy in circulating m-SBF,” *Materials Letters*, vol. 64, pp. 1996–1999, sep 2010.

- [113] F. Witte, K. Bobe, and M. Meier, “Mri based perfusion measurements in bone after implantation of biodegradable magnesium rods,” *Eur Cells Mater*, vol. 26, 01 2013.
- [114] S. Hiromoto, A. Yamamoto, N. Maruyama, H. Somekawa, and T. Mukai, “Influence of pH and flow on the polarisation behaviour of pure magnesium in borate buffer solutions,” *Corrosion Science*, vol. 50, pp. 3561–3568, dec 2008.
- [115] K. D. Efird, “Flow effects on corrosion,” in *Uhlig's Corrosion Handbook*, pp. 203–213, John Wiley & Sons, Inc., apr 2011.
- [116] L. Xu and Y. Cheng, “Effect of fluid hydrodynamics on flow-assisted corrosion of aluminum alloy in ethylene glycol–water solution studied by a microelectrode technique,” *Corrosion Science*, vol. 51, pp. 2330–2335, oct 2009.
- [117] W. M. H. Versteeg, *Introduction to Computational Fluid Dynamics*, An. Pearson Education (US), 2007.
- [118] A. Sharma, *Introduction to Computational Fluid Dynamics*. Springer International Publishing, 2022.
- [119] D. W. Hutmacher and H. Singh, “Computational fluid dynamics for improved bioreactor design and 3d culture,” *Trends in Biotechnology*, vol. 26, pp. 166–172, apr 2008.
- [120] M. S. Hossain, X. B. Chen, and D. J. Bergstrom, “Investigation of the in vitro culture process for skeletal-tissue-engineered constructs using computational fluid dynamics and experimental methods,” *Journal of Biomechanical Engineering*, vol. 134, nov 2012.
- [121] A. R. Patrachari, J. T. Podichetty, and S. V. Madihally, “Application of computational fluid dynamics in tissue engineering,” *Journal of Bioscience and Bioengineering*, vol. 114, pp. 123–132, aug 2012.
- [122] T. J. Chung, *Computational Fluid Dynamics*. Cambridge University Press, 2014.
- [123] A. Quarteroni, “Navier-stokes equations,” in *Numerical Models for Differential Problems*, pp. 429–482, Springer Milan, 2014.
- [124] V. Girault and P.-A. Raviart, *Finite Element Approximation of the Navier-Stokes Equations*. Springer Berlin Heidelberg, 1979.

- [125] H. Elman, D. Silvester, and A. Wathen, *Finite Elements and Fast Iterative Solvers with Applications in Incompressible Fluid Dynamics*. Oxford University PressOxford, jun 2014.
- [126] F. de Vuyst, “Numerical modeling of transport problems using freefem++ software – with examples in biology, CFD, traffic flow and energy transfer.” Lecture, Sept. 2013.
- [127] G. Karypis and V. Kumar, “A fast and high quality multilevel scheme for partitioning irregular graphs,” *SIAM J. Sci. Comput.*, vol. 20, p. 359–392, Dec. 1998.
- [128] S. F. McCormick, *Multigrid methods*. SIAM, 1987.
- [129] Y. Guyot, I. Papantoniou, F. P. Luyten, and L. Geris, “Coupling curvature-dependent and shear stress-stimulated neotissue growth in dynamic bioreactor cultures: a 3d computational model of a complete scaffold,” *Biomechanics and Modeling in Mechanobiology*, vol. 15, pp. 169–180, jan 2016.
- [130] H. G. Weller, G. Tabor, H. Jasak, and C. Fureby, “A tensorial approach to computational continuum mechanics using object-oriented techniques,” *Computers in Physics*, vol. 12, no. 6, p. 620, 1998.
- [131] M. Barzegari, D. Mei, S. V. Lamaka, and L. Geris, “Computational modeling of degradation process of biodegradable magnesium biomaterials,” *Corrosion Science*, vol. 190, p. 109674, 2021.
- [132] G. Chourdakis, K. Davis, B. Rodenberg, M. Schulte, F. Simonis, B. Uekermann, G. Abrams, H. Bungartz, L. Cheung Yau, I. Desai, K. Eder, R. Hertrich, F. Lindner, A. Rusch, D. Sashko, D. Schneider, A. Totounferoush, D. Volland, P. Vollmer, and O. Koseomur, “pre-CICE v2: A sustainable and user-friendly coupling library [version 1; peer review: 2 approved],” *Open Research Europe*, vol. 2, no. 51, 2022.
- [133] L.-N. Zhang, Z.-T. Hou, X. Ye, Z.-B. Xu, X.-L. Bai, and P. Shang, “The effect of selected alloying element additions on properties of mg-based alloy as bioimplants: A literature review,” *Frontiers of Materials Science*, vol. 7, pp. 227–236, jul 2013.
- [134] X. Li, X. Liu, S. Wu, K. Yeung, Y. Zheng, and P. K. Chu, “Design of magnesium alloys with controllable degradation for biomedical implants: From bulk to surface,” *Acta Biomaterialia*, vol. 45, pp. 2–30, nov 2016.

- [135] A. Atrens, Z. Shi, S. U. Mehreen, S. Johnston, G.-L. Song, X. Chen, and F. Pan, “Review of mg alloy corrosion rates,” *Journal of Magnesium and Alloys*, vol. 8, pp. 989–998, dec 2020.
- [136] N. Kirkland, N. Birbilis, and M. Staiger, “Assessing the corrosion of biodegradable magnesium implants: A critical review of current methodologies and their limitations,” *Acta Biomaterialia*, vol. 8, pp. 925–936, mar 2012.
- [137] N. A. Agha, F. Feyerabend, B. Mihailova, S. Heidrich, U. Bismayer, and R. Willumeit-Römer, “Magnesium degradation influenced by buffering salts in concentrations typical of in vitro and in vivo models,” *Materials Science and Engineering: C*, vol. 58, pp. 817–825, jan 2016.
- [138] L.-Y. Cui, Y. Hu, R.-C. Zeng, Y.-X. Yang, D.-D. Sun, S.-Q. Li, F. Zhang, and E.-H. Han, “New insights into the effect of tris-HCl and tris on corrosion of magnesium alloy in presence of bicarbonate, sulfate, hydrogen phosphate and dihydrogen phosphate ions,” *Journal of Materials Science & Technology*, vol. 33, pp. 971–986, sep 2017.
- [139] M. B. Kannan, H. Khakbaz, and A. Yamamoto, “Understanding the influence of HEPES buffer concentration on the biodegradation of pure magnesium: An electrochemical study,” *Materials Chemistry and Physics*, vol. 197, pp. 47–56, aug 2017.
- [140] Y. Song, D. Shan, R. Chen, F. Zhang, and E.-H. Han, “Biodegradable behaviors of AZ31 magnesium alloy in simulated body fluid,” *Materials Science and Engineering: C*, vol. 29, pp. 1039–1045, apr 2009.
- [141] P. Jiang, C. Blawert, N. Scharnagl, and M. L. Zheludkevich, “Influence of water purity on the corrosion behavior of mg0.5znx (x=ca, ge) alloys,” *Corrosion Science*, vol. 153, pp. 62–73, jun 2019.
- [142] D. Mei, C. Wang, S. V. Lamaka, and M. L. Zheludkevich, “Clarifying the influence of albumin on the initial stages of magnesium corrosion in hank’s balanced salt solution,” *Journal of Magnesium and Alloys*, vol. 9, pp. 805–817, may 2021.
- [143] D. Höche, “Simulation of corrosion product deposit layer growth on bare magnesium galvanically coupled to aluminum,” *Journal of The Electrochemical Society*, vol. 162, no. 1, pp. C1–C11, 2014.

- [144] B. Zeller-Plumhoff, T. AlBaraghtheh, D. Höche, and R. Willumeit-Römer, “Computational modelling of magnesium degradation in simulated body fluid under physiological conditions,” *Journal of Magnesium and Alloys*, vol. 10, pp. 965–978, apr 2022.
- [145] B. Zeller-Plumhoff, M. Gile, M. Priebe, H. Slominska, B. Boll, B. Wiese, T. Würger, R. Willumeit-Römer, and R. H. Meißner, “Exploring key ionic interactions for magnesium degradation in simulated body fluid – a data-driven approach,” *Corrosion Science*, vol. 182, p. 109272, apr 2021.
- [146] J. Gonzalez, S. V. Lamaka, D. Mei, N. Scharnagl, F. Feyerabend, M. L. Zheludkevich, and R. Willumeit-Römer, “Mg biodegradation mechanism deduced from the local surface environment under simulated physiological conditions,” *Advanced Healthcare Materials*, vol. 10, p. 2100053, may 2021.
- [147] N. Ingri, W. Kakolowicz, L. G. Sillén, and B. Warnqvist, “High-speed computers as a supplement to graphical methods—v1haltafall, a general program for calculating the composition of equilibrium mixtures,” *Talanta*, vol. 14, pp. 1261–1286, nov 1967.
- [148] B. Warnqvist, “The HALTAFALL program-some corrections, and comments on recent experience,” *Talanta*, vol. 18, pp. 457–458, apr 1971.
- [149] G. Eriksson, “An algorithm for the computation of aqueous multi-component, multiphase equilibria,” *Analytica Chimica Acta*, vol. 112, pp. 375–383, dec 1979.
- [150] C. Wang, C. Song, D. Mei, L. Wang, W. Wang, T. Wu, D. Snihirova, M. L. Zheludkevich, and S. V. Lamaka, “Low interfacial pH discloses the favorable biodegradability of several mg alloys,” *Corrosion Science*, vol. 197, p. 110059, apr 2022.
- [151] M. Barzegari and L. Geris, “Highly scalable numerical simulation of coupled reaction–diffusion systems with moving interfaces,” *The International Journal of High Performance Computing Applications*, vol. 36, no. 2, pp. 198–213, 2022.
- [152] D. Mareci, G. Bolat, J. Izquierdo, C. Crimu, C. Munteanu, I. Antoniac, and R. Souto, “Electrochemical characteristics of bioresorbable binary MgCa alloys in ringer's solution: Revealing the impact of local pH distributions during in-vitro dissolution,” *Materials Science and Engineering: C*, vol. 60, pp. 402–410, mar 2016.

- [153] S. Gnedenkov, S. Sinebryukhov, V. Egorkin, D. Mashtalyar, I. Vyaliy, K. Nadaraia, I. Imshinetskiy, A. Nikitin, E. Subbotin, and A. Gnedenkov, “Magnesium fabricated using additive technology: Specificity of corrosion and protection,” *Journal of Alloys and Compounds*, vol. 808, p. 151629, nov 2019.
- [154] U. M. Tefashe, P. Dauphin-Ducharme, M. Danaie, Z. P. Cano, J. R. Kish, G. A. Botton, and J. Mauzeroll, “Localized corrosion behavior of AZ31b magnesium alloy with an electrodeposited poly(3,4-ethylenedioxythiophene) coating,” *Journal of The Electrochemical Society*, vol. 162, no. 10, pp. C536–C544, 2015.
- [155] S. Lamaka, G. Knörnschild, D. Snihirova, M. Taryba, M. Zheludkevich, and M. Ferreira, “Complex anticorrosion coating for ZK30 magnesium alloy,” *Electrochimica Acta*, vol. 55, pp. 131–141, dec 2009.